Active Galactic Nuclei Feedback in Multiphase Gaseous Halos

by

Chaoran Wang

A dissertation submitted in partial fulfillment
of the requirements for the degree of
Doctor of Philosophy
(Astronomy and Astrophysics)
in The University of Michigan
2021

Doctoral Committee:

Associate Professor Mateusz Ruszkowski, Chair
Professor Eric Bell
Professor August Evrard
Professor Mark Voit

Chaoran Wang

wangcha@umich.edu

ORCID iD: 0000-0003-1003-8662

ACKNOWLEDGEMENTS

Thanks to Mateusz. No doubt that you are the person that have helped and taught me the most in the past five years.

Thanks to my family, my mother and father. You are the ones I love the most.

Thanks to all the people that helped me for finishing my Ph.D: my thesis committee, my collaborators and faculty and staff of the Astronomy Department. Your valuable endeavour is essential to the development of my academic career.

Thanks to all my colleagues in the Astronomy department, for creating an inclusive and friendly working atmosphere.

TABLE OF CONTENTS

LIST OF FIGURES

Figure

LIST OF TABLES

Table

LIST OF APPENDICES

Appendix

ABSTRACT

In this thesis, I study the evolution of multiphase gaseous halos of galaxy clusters, groups, and giant elliptical galaxies using numerical simulations. I investigate how the key physical processes and model ingredients, including AGN feedback, cosmic rays, magnetic fields, and turbulence, play a role in the evolution of these systems.

I perform hydrodynamical simulations to study the observed "multiphase" and "single-phase" dichotomy in giant elliptical galaxies. The multiphase galaxies possess hot gaseous halos conducive to the development of thermal instability. These galaxies are characterized by the presence of extended cold gas filaments. The gaseous halos in the single-phase galaxies are less likely to develop thermal instability and cold gas is either absent or only located in the nuclear region in such galaxies. My simulations reproduce such "multiphase" and "single-phase" dichotomy in agreement with the observations. Importantly, I find that self-regulated AGN feedback maintains the multi- or single- phase nature of the halos but does not turn multiphase galaxies into single-phase ones or vice versa.

The long-term evolution of the simulated multiphase and single-phase galaxies reveals the formation of long-lived massive cold disks. Such disks are also seen in many other numerical simulations in the literature but are in tension with the observations. Thus, I explore a possible solution to this "disk problem" and find that magnetic fields can offer one such solution. The magnetic fields are overall weak in the hot halo but are locally amplified in the cold gas. The amplified magnetic fields effectively reduce the angular momentum of the cold gas, thus preventing the formation of the problematic disks. Additionally, I find that when the plasma composition in the AGN jets is dominated by cosmic rays, and when cosmic ray transport is included, the hot gaseous halos can maintain global thermal

equilibrium and the massive cold central disks do not form. In this case, the power of the AGN feedback is reduced as its energy is utilized more efficiently to heat the ambient gas compared to the case of purely kinetic AGN feedback.

Motivated by my finding that the magnetic fields have important dynamical impact on the cold gas, and by recent observational work on probing the ICM turbulence using the velocity structure function of the cold ICM filaments, we study the properties of turbulence in the multiphase ICM by calculating the velocity structure functions of different phases in the simulated ICM affected by the AGN feedback. We find that while the simulated turbulence is not consistent with the predictions from the classic Kolmogorov theory of turbulence, it is broadly consistent with the observations. We suggest a novel hypothesis supported by our simulations, that the turbulence of hot gas at the ICM center is driven both by the AGN outflows and the cold filaments formed via local thermal instability.

Finally, I study the energetic impact of turbulence on counterbalancing the radiative cooling in the ICM. I present an analytic model that quantitatively describes the heating rate due to turbulent dissipation and turbulent mixing. In this work, I elucidate the important, yet commonly neglected, role of the gravitational field in regulating these heat rates.

CHAPTER I

Introduction

Gaseous halos play a crucial role in the evolution of early-type galaxies, from the intracluster (ICM) and intragroup medium (IGM), in which the central dominant galaxies reside, to the circumgalactic medium (CGM) around smaller early-type ellipticals. In this thesis, I focus on the evolution of multiphase gaseous halos of galaxy clusters, groups, and giant elliptical galaxies. As suggested by the multi-wavelength observations of these systems, various physical processes and model ingredients play key roles in the evolution of these halos including, but not limited to, thermal instabilities, feedback from the Active Galactic Nuclei (AGN), cosmic rays (CRs), magnetic fields, and turbulence. They are all coupled with one another, thus making the evolution of these systems highly non-linear. Therefore, numerical simulations are the main approach adopted by researchers to understand the interplay between these processes and the properties of the gaseous halos.

1.1 The multiphase gas in and around early-type galaxies

1.1.1 X-ray properties of hot galactic halos

In a ΛCDM universe, large scale structure in the Universe grows predominantly via hierarchical merging of dark matter halos. Baryons fall into the gravitational potentials of the dark matter halos. The gaseous halos then undergo virial collapse, where halos collapse due to gravity until their sizes reduce to the virial radius, and the kinetic energy of the infall

and gravitational potential energy are virialized. In the subsequent evolution, pressure of the gas becomes important against the gravitational compression, and thus the infall slows down in the center. However, the infall velocity of the gas is typically supersonic and the gas in the center cannot adjust itself quickly enough against the infall of the gas at larger radii. Consequently, such infall creates a shock. In the classical picture of the gas accretion onto galaxies, the evolution of the post-shock gas is described as "hot mode" or "cold mode" accretion. *White and Rees* (1978) were the first to discuss the two distinct modes. They demonstrate that whether the gas accretion is in the hot or cold mode depends on the ratio of the cooling to dynamical time of the post-shock gas. This ratio is determined by the mass of the halo. In the "hot mode" scenario, which is expected in halos with mass larger than a threshold value of $\sim 10^{12} M_{\odot}$, the post-shock gas is able to form a quasi-stable, volume filling halo with temperature comparable to the virial temperature of the halo. In the "cold mode" scenario, predicted to occur in halos less massive than the threshold, the post-shock gas cannot be pressure-supported and collapses to a galaxy-scale disk as explained below.

Using one-dimensional hydrodynamic simulations, *Birnboim and Dekel* (2003) find agreement with this picture and obtain similar threshold halo mass dividing these two modes. They further attribute the hot and cold mode dichotomy to the stability of the post-shock gas against the contractive perturbation induced by the infall velocity. If the pressure fluctuation corresponding to the induced perturbation is large enough to push the gas back, the post-shock gas will be stable and gas accretion will proceed via the hot mode. In the unstable case, pressure gradients fail to restore the contraction and the run-away growth of the perturbation leads to the gas collapse onto a rotationally-supported disk; hence the unstable case corresponds to the cold mode accretion. The stability criterion depends on the radiative cooling rate in the sense that the internal energy loss due to radiative cooling reduces the corresponding pressure fluctuation. However, subsequent works in the literature suggest that gas accretion is more complicated than this simple dichotomy scenario. For example, at high-redshift cold gas can directly accrete onto the galaxy along filaments in

massive halos without being virially shocked (*Kereš et al.*, 2005, 2009; *Dekel and Birnboim*, 2006). Furthermore, stellar feedback from the stars formed in the disk can affect this two modes picture and halos with mass well below the $10^{12} M_{\odot}$ threshold can also accrete gas via the hot mode accretion. The halo gas will consequently be multiphase (*Fielding et al.*, 2017; *Stern et al.*, 2020), in agreement with the multiphase nature of the observed circumgalactic medium (CGM).

Nevertheless, for the most massive halos ($\gtrsim 10^{14} M_{\odot}$) in the Universe, the post-shock halo gas should be sufficiently virialized and its cooling time is longer than the Hubble time in the most parts of the halos. The temperature of the stable gas is similar to the virial temperature of the halo, which is on the level of $\sim$ keV. Thus, the gaseous halos emit radiation predominantly via thermal bremsstrahlung emission in X-rays. However, in a large fraction of galaxy clusters, the radiative cooling time can be much shorter in the centers of cool cores. This leads to the condensation of cold gas out of the hot halo gas and feeding of the central supermassive black hole (SMBH). This topic is discussed more in detail in Section 1.2.

1.1.2 Optical and Hα emission from the cold gas in galactic halos

Reservoirs of cold gas (molecular and atomic) associated with the hot X-ray halos are common in isolated giant elliptical galaxies and central dominant galaxies of galaxy clusters and galaxy groups. Smaller early type galaxies (ETGs) can also host significant amounts of cold gas. That the cold gas is common in ETGs is not trivial, because ETGs are typically considered "red and dead," i.e., they lack recent star formation. Although it is rather clear that the cold reservoirs of the central galaxies are generated by cooling of the gas out of the hot halos, it is still under debate whether the cold gas in smaller satellite and isolated ETGs has the same origin as that in the central dominant counterparts of ETGs. Thus, it is crucial to understand the properties and origin of the cold gas in ETGs in order to understand the evolution of these galaxies.

1.1.2.1 General properties of the cold gas phase

It has been known that cold gas is common in early-type galaxies either from individual observations (e.g., *Morganti et al.*, 2006; *Combes et al.*, 2007; *Oosterloo et al.*, 2010) or large surveys. Using the IRAM-30m telescope, *Young et al.* (2011) finds that $\sim$ 22% of the early-type galaxies of the ATLAS^{3D} survey (*Cappellari et al.*, 2011) have molecular gas detections with typical masses of $10^7 \sim 10^9 M_\odot$. The ATLAS^{3D} sample consist of relatively low-mass (median stellar mass $M_* \sim 3 \times 10^{10} M_\odot$) ETGs including many Virgo cluster members; atomic (HI) gas detection is also common, at the rate of 40% for all ATLAS^{3D} ETGs outside the Virgo cluster and 10% inside, and the detected HI mass falls in $5 \times 10^6 \sim 5 \times 10^9 M_\odot$ range, which is similar to the mass range of molecular masses (*Serra et al.*, 2012). The HI/H_2 mass ratios are, however, highly variable, ranging from 0.01 to 100 (*Young et al.*, 2014). IRAM observations of a representative subset of the samples from the MASSIVE project (*Ma et al.*, 2014) – a survey sampling ETGs with the highest masses ($M_* > 10^{11.5} M_\odot$) in the local Universe – find a similar molecular gas detection rate and typical molecular masses (*Davis et al.*, 2019). Although the MASSIVE objects are a mixture of isolated, satellite, and central galaxies (*Veale et al.*, 2017), the sampled objects are still predominantly isolated and satellite ETGs, as in the case of the ATLAS^{3D} project. This similarity is due to the volume-limited and complete nature of these surveys. The morphologies of the cold gas in non-central ETGs are dominated by disks and ring-like structures as shown by the double-horned shape of detected CO spectra and the re-constructed images from interferometric observations (e.g., *Crocker et al.*, 2011; *Young et al.*, 2011; *Chung et al.*, 2012; *Alatalo et al.*, 2013; *Davis et al.*, 2013).

The properties of the molecular gas in these ETGs are also affected by the environment. Compared to isolated ETGs, satellite ETGs have significantly reduced molecular gas extent and the ratio between molecular and stellar mass. Such reduction can be due to: (1) starvation, i.e., the cessation of cold gas supply to the galaxy (*Peng et al.*, 2015), which can be realized by the strong suppression of cold gas accretion onto satellite galaxies in

dense environment (*van de Voort et al.*, 2017); and/or (2) direct removal of the interstellar medium (ISM) via ram pressure stripping or tidal interactions in the cluster environments (*Davis et al.*, 2013).

However, the detection rate of the molecular gas is not statistically different between satellite and isolated ETGs. This is found to be the case in the ATLAS^{3D} ETGs (*Young et al.*, 2011) and these conclusions carry over to the higher mass regime covered by the MASSIVE sample (*Davis et al.*, 2019).

The central dominant galaxies of galaxy clusters and groups are often found to contain huge cold gas reservoirs with masses from $10^9 M_\odot$ to several $10^{11} M_\odot$ (e.g., *Edge*, 2001; *Churazov et al.*, 2003). Unlike in the case of the smaller ETGs, the cold gas in the central galaxies often exhibits extended morphologies that rarely shows evidence for rotational support (*Donahue et al.*, 2015a; *Russell et al.*, 2019). Such differences in morphology may be explained by the more common rotation, or different origins of the cold gas in satellite and isolated ETGs.

1.1.2.2 The origin of the cold gas

The origin of the cold gas is crucial for understanding the evolution of ETGs. Many possible scenarios for the origin of the cold gas have been considered and studied in the literature, including external sources of cold mode accretion in galaxy mergers and tidal stripping from neighbor galaxies; and internal sources such as residual star-forming gas, stellar mass loss, and condensation of the hot gaseous halos.

Brightest cluster galaxies (BCGs) are located at the centers of galaxy cluster potentials. Because of this unique position it is likely that large amounts of cold gas may accrete onto the BCGs from the ICM. The central hot ICM of a large fraction of galaxy clusters possess cool cores within which the gas entropy is low and the radiative cooling time is much shorter than the Hubble time. The cool cores are usually found to contain significant amounts of cold gas (*Pulido et al.*, 2018). This clearly suggests that the cold gas in the ICM could

originate via the cooling of the hot ICM. While a consensus has been reached that the cold gas is predominantly generated from the cooling of the hot gaseous halos in the BCGs and in some of the group central ETGs, it is still a matter of debate which process dominates the supply or generation of the cold gas in isolated and satellite ETGs. It is conceivable that multiple sources may contribute to the cold gas reservoirs in these sources.

By studying the extent and kinematics of the molecular gas in the ATALAS^{3D} ETGs, *Davis et al.* (2011) find that nearly half of the detected molecular disks in the fast rotators (i.e., objects in which the stars exhibit significant coherent rotation) of the local isolated ETGs are misaligned with the stellar rotational axis. The authors attribute the high fraction of objects exhibiting misalignment to the external origin of the cold reservoirs, e.g., gas-rich mergers. Old stellar populations in ETGs, especially stars on the asymptotic giant brunch (AGB), can go through periods of severe mass loss. The lost mass is ejected to the ambient space through stellar winds and may cool down to the atomic and molecular temperatures, supplying the galaxy with cold gas (e.g., *Serra et al.*, 2014; *Negri et al.*, 2015). While *Davis et al.* (2011) find that the Virgo cluster member ETGs generally have aligned molecular disks, which presumably indicates stellar mass loss origin, it is unlikely that the stellar ejecta are the dominant source of cold gas as no correlation is found between the molecular masses and the stellar masses for ATLAS^{3D} ETGs (*Young et al.*, 2011). Although gas-rich samples of more massive ETGs in the MASSIVE survey commonly host giant molecular gas reservoirs, tentatively indicating that stellar mass-loss becomes more important in ETGs with much larger stellar halos (*Davis et al.*, 2016), the correlation between old stellar mass and molecular mass is still missing in the less biased samples of MASSIVE galaxies (*Davis et al.*, 2019). However, dust and polycyclic aromatic hydrocarbon (PAH) emission are present in the mid infrared spectra of cold gas clouds in ETGs (e.g., *Panuzzo et al.*, 2011; *Donahue et al.*, 2011; *Werner et al.*, 2014), suggesting stellar contribution. Therefore, stellar mass loss should at least partially contribute to the cold gas origin, though it may not be the dominant source.

Combining the statistics of molecular gas in ETGs of the ALTAS^{3D} and MASSIVE surveys, *Davis et al.* (2019) present an analytic toy model describing the galaxy evolution from $z = 1$, aiming at matching the observed detection rate of ETGs' molecular gas, gas mass function, and the gas kinematic misalignment distribution as a function of the environment over-density. Their model shows that gas accretion during the gas-rich galaxy mergers contributes the most to the origin of ETGs' molecular gas. Stellar mass loss and hot gas condensation should play minor roles. While the former is widely considered as sub-dominant, there are questions that need to be answered regarding the latter. First, molecular disks that are misaligned with the rotation axis of stellar distribution do not necessarily result from external accretion. This is because condensation from rotating hot halo, that has rotational axis misaligned with respect to the stellar rotation axis, can also produce a cold disk that is misaligned with the stellar distribution. Thus, one of the key questions regarding the origin of the hot gas condensation, that may be answered with future observational data from high resolution X-ray spectrometers, is whether the fraction of the misaligned hot halos is high enough to account for the high rate of the misalignment of molecular disks. Second, the misaligned hot halo may be able to enhance cold gas condensation due to the collision between the hot halo and stellar ejecta. If that is the case, then the X-ray luminosity of the gas, which indicates the amount of cooling, should correlate with the parameters related to this process. Such correlations, though not found by (*Davis et al.*, 2019), could be tested by future observations with larger sample size and better sensitivity to $\sim 10^5$K gas.

However, galaxy mergers are much rarer for satellite galaxies in the cluster environments than for isolated galaxies. Therefore, mergers cannot fully account for the observed amount of cold gas in cluster environments. Given that the detection rate of molecular gas in ETGs does not depend on the environment, there should be an additional mechanism supplying the cold gas in cluster satellite ETGs. The *Davis et al.* (2019) model accounts for the missing cold gas in satellite ETGs by invoking morphological transformation of spiral galaxies to ETGs via environmental quenching. Such process can preserve a large

fraction of the residual cold gas from the star formation of the original spirals and it can form aligned molecular disks, which is consistent the properties of the observed satellite ETGs. However, it is puzzling that the detection rate of the cold gas remaining after the morphological transformation process is essentially the same as in the isolated ETGs. This apparent conspiracy may merit further investigation.

Babyk et al. (2019) find that the molecular gas mass correlates with the hot gas mass and density across about three-orders of magnitude in halo mass, from the gaseous halos of normal giant ellipticals all the way to the BCGs. In this sense, the hot gaseous halos in the less massive ETGs are scaled-down versions of the central dominant galaxies; thus, the process of hot gas condensation may unify the picture of the cold gas origin in the ETGs. However, due to the low X-ray brightness, the hot halos of non-central ETGs are not as well understood as those of galaxy clusters. The molecular mass–X-ray gas mass relation and the molecular mass–X-ray gas density relation presented in *Babyk et al.* (2019) show larger scatter in the non-BCG regime. The larger scatter may be due to systemic differences between the properties of the hot halos of the BCGs and non-BCGs. Rotation may be one of the properties associated with the larger scatter in non-central galaxies because fast rotators are much more common in such systems. Development of thermal instabilities might be easier in rotating halos (*Juráňová et al.*, 2020), leading to the formation of more massive cold disks than cold gas filaments formed in the non-rotating counterparts. Additionally, rotational support can prevent the cold gas from being quickly accreted by the central SMBH and fuelling the AGN. Consequently, the rotating hot halos are less heated by the AGN feedback and produce more condensation. Therefore, rotation can increase the molecular gas mass at a given mass or density of the hot halo. This is consistent with the most molecular gas–rich outliers in Babyk's relation being the S0, Sa and Sb ETGs with huge molecular disks.

While it is yet to be confirmed that the cold gas disks in non-BCG early types can be mostly accounted for by invoking rotating hot halos, other possibilities for the origin of

cold disks are still worthwhile considering. Some ETGs do not have detectable X-ray hot halos, but many of them still host large amounts of molecular gas. For example, *O'Sullivan et al.* (2018) studies central dominant ETGs of the galaxy groups (brightest group early types; BGEs) in the Complete Local-Volume Groups Sample (*O'Sullivan et al.*, 2017). In their sample, only 2 out of 21 CO-detected BGEs show extended structures, which are very similar in appearance to the distributions of the cold gas in BCGs. Since the extended structures in BCGs are most likely due to cooling of the cold phase out of the hot ICM, the origin of the extended structures in these two BGEs is likely the same as in BCGs. The other objects in the *O'Sullivan et al.* (2018) sample commonly contain disks, many of which reside in groups in which X-ray halos are not detected. Although additional X-ray observations are needed to cover all of the 21 CO-detected BGEs, these results nevertheless pose challenges to the hot halo cooling origin for the molecular gas. Furthermore, cold gas condensed out of the hot halo generally takes the form of extended filaments rather than rotating disks (unless the hot halo is rotating). These arguments suggest that alternative origin for the cold gas may need to be invoked especially for the objects possessing cold disk morphologies. As argued by *O'Sullivan et al.* (2018), the BGEs with cold disks often show evidence for disturbed morphologies and interactions with other galaxies. The molecular gas in these galaxies likely arises from tidal stripping, where the galaxies acquire the gas from their neighbors, or where there are residual structures left behind after previous galaxy encounters.

In summary, cold gas in BCGs and in some BGEs and isolated elliptical galaxies, likely originates from the cooling of the hot halo. However, in other BGEs, and smaller non-central ETGs, especially the ones that possess cold disks, alternative (external) origin of the cold gas is possible, including tidal stripping and gas-rich mergers.

Interestingly, hydrodynamic simulations of AGN feedback and the evolution of the hot gaseous halos of galaxy groups and clusters often reveal the formation of persistent, massive cold disks. These results are found in many simulations reported on both in the literature

(e.g., *Li et al.*, 2015; *Eisenreich et al.*, 2017; *Qiu et al.*, 2019b, 2021) and in this thesis. However, such disks are in tension with the observations because the simulated disks are too massive compared to those commonly observed in the galaxies considered in these simulations (note that no initial rotation is included in these simulations). Therefore, the disk formation in the simulated hot halos is unphysical and suggests that key physics may be missing in these simulations. In one of my papers (*Wang et al.*, 2020, Chapter III), I show that weak magnetic fields can have significant dynamical effect on the condensed cold gas and can prevent the formation of the unphysical disks in simulations.

1.1.3 Radio and γ-ray emission and the role of cosmic rays

In the hot gaseous halos, the powerful AGN jets can inflate bubble-like structures in the ambient medium. Although the jet-inflated bubbles are found to be faint in X-rays (and are thus often referred to as X-ray "cavities"), they are bright at radio frequencies. These bubbles emit synchrotron radiation, which is indicative of the presence of relativistic electrons (or cosmic ray electrons, CRes) and magnetic fields. However, as shown by *Dunn and Fabian* (2004), the energy density in the synchrotron-emitting CRes plus that in the magnetic fields are insufficient to maintain the pressure balance between the bubbles and the ambient hot ICM. Additional pressure support could be provided by "dark" material inside the bubbles, which should be faint in X-ray and radio bands, in the form of, e.g., ultra-hot gas or cosmic-ray protons (CRps).

Moreover, LOFAR low radio frequency observations of the Virgo cluster, that aim to probe the spectrally-aged old fossil CRes, do not detect the accumulation of old electrons at low radio frequencies expected due to synchrotron losses (*de Gasperin et al.*, 2012). The absence of old CRes in the outer radio halo implies that the CRes originally contained in the bubbles inflated by past AGN activity should have been transported out of the bubbles and then mixed and thermalized in the ambient gas (e.g., via Coulomb interactions). Such transport may be accounted for by the cosmic ray streaming (see Section 3.3 for more details).

Furthermore, Fermi and H.E.S.S observations of M87 (*Abdo et al.*, 2012) reveal a steady gamma-ray flux that corresponds to the same slope of the particle distribution as that derived from the radio photon spectrum. This suggests that CR protons, that are responsible for the gamma-ray emission, and the synchrotron-emitting CR electrons have common origin. *Pfrommer* (2013) puts forward a model for the AGN feedback heating mechanism, where the AGN jets inflate CR-filled (both CRes and CRps) bubbles in the ambient gas. As the bubbles propagate through the halo, the CRs are transported outward via CR streaming, which together with the hadronic interactions, heats the surrounding gas. Pfrommer's model shows that such heating rate is able to balance the radiative cooling rate of the hot plasma on average at every radius. While the global thermal equilibrium is maintained, local thermal instabilities can develop, and lead to the cold gas condensation out of the hot plasma. Using one-dimensional models, *Jacob and Pfrommer* (2017a) show that CRs produced by the AGN feedback can effectively heat the gas without violating observational constraints in the radio and gamma-rays. Three-dimensional MHD simulations performed by *Ruszkowski et al.* (2017a) and *Wang et al.* (2020) (Chapter III) show that the CR-dominated AGN feedback that includes CR transport processes can indeed maintain the self-regulated evolution of the hot halos while maintaining global thermal equilibrium.

1.2 Coupled evolution of the AGN feedback, cold gas, and hot gaseous halos

1.2.1 Classical cooling flow problem

In the central regions of a significant fraction of the hot gaseous halos of galaxy clusters, groups and giant elliptical galaxies, the radiative cooling time is much shorter than the Hubble time. Subsonic inflow of gas should then form to re-establish the pressure support against gravity. This is the so-called cooling flow (CF) model (*Fabian*, 1994). The CF model naturally predicts that the gas should accumulate at the halo center. Consequently,

the strong cooling of the central high density gas should lead to X-ray brightness cusp and star formation rate at hundreds to thousands solar mass per year.

However, neither the high star formation rate nor central X-ray cusps are observed, and the cooling rate turns out to be overestimated by the CF model by more than an order of magnitude. These observations suggest that the gaseous halos have very short cooling time in the halo centers and low actual cooling rates at the same time. This implies the presence of a significant heating source, which is able to effectively offset the radiative cooling losses and maintain the overall thermal equilibrium of the hot gaseous halos.

There is a consensus that feedback from the AGN associated with the central SMBH can balance the radiative cooling and play essential role in maintaining global thermal equilibrium of the hot gaseous halos. The key observational findings that support this hypothesis are the following. First, observations reveal the existence of morphological structures including cavities, shocks, and ripples in X-ray images; cavities are co-spatial with the radio lobes connected to the central engine. These structures can be well explained by the strong interactions between the AGN feedback and the ambient gas. Second, the radiative cooling rate of the gaseous halos and the cavity power are strongly correlated (*Rafferty et al.*, 2006). Third, the existence of cold filaments coincides with AGN activity (*Cavagnolo et al.*, 2008; *Tremblay et al.*, 2016). This indicates that the energy supply from the AGN is well regulated to counterbalance the radiative cooling in the time-averaged sense (*Croton et al.*, 2006). For a more comprehensive review of AGN heating in the gaseous halos see *McNamara and Nulsen* (2007, 2012) and *Fabian* (2012).

Despite the many appealing aspects of the AGN feedback model supported by the above observational findings, important details of mechanisms of the energy transfer from the AGN to the ambient halo gas remain unclear. Multiple possibilities have been explored in the literature. I introduce this topic in more detail in the Section 3.3.

1.2.2 Local thermal instability

Observations reveal that the hot gaseous halos are found when the ratio between the radiative cooling time $t_{\rm cool}$ and the gravitational free-fall time $t_{\rm ff}$ exceeds a critical value $t_{\rm cool}/t_{\rm ff} \gtrsim 10$. Additionally, $t_{\rm cool}/t_{\rm ff}$ of the hot halos that do not possess cold clumps (i.e., single-phase halos) generally have $\min(t_{\rm cool}/t_{\rm ff}) \gtrsim 20$, while the ones where extended cold gas structures are present (known as multiphase halos) have $10 \lesssim \min(t_{\rm cool}/t_{\rm ff}) \lesssim 20$ (*Werner et al.*, 2014; *Voit and Donahue*, 2015; *Voit et al.*, 2017). This implies that the observed cold clumps form due to the cooling and condensation of the hot halo gas. It has long been realized in the literature that $t_{\rm cool}/t_{\rm ff}$ is tightly correlated with the degree to which gravitationally stratified medium is prone to the development of thermal instability (TI; e.g., *McCourt et al.*, 2012; *Sharma et al.*, 2012; *Voit and Donahue*, 2015). Assuming a global thermal equilibrium in a static medium with vertical stratification, the simulations performed by *McCourt et al.* (2012) show that $t_{\rm cool}/t_{\rm ff} \sim 1$ is the threshold for nonlinear growth of thermal instabilities below which cold clumps condense out of hot halos. However, realistic hot gaseous halos exist in the regime where $t_{\rm cool}/t_{\rm ff} \gg 1$. This is because the development of thermal instabilities in the hot gaseous halos is further affected by a number of factors such as the details of AGN feedback, turbulence, and the entropy gradient.

As suggested in a more comprehensive theoretical study of *Voit et al.* (2017), thermal instability can saturate via buoyancy damping instead of developing run-away condensations. As the initial entropy perturbation oscillates in the gravitationally-stratified medium, it can drive acoustic waves in the ambient medium that dissipate its kinetic energy. Generally, if the dissipation timescale is shorter than the timescale for the TI development, the perturbation will saturate without developing condensations. The timescale criterion for the onset of TI can be expressed in terms of a critical slope of the entropy profile $\alpha_K = r\nabla \ln K \sim (t_{\rm cool}/t_{\rm ff})^{-2}$, where $K = k_B T n_e^{-2/3}$ is the gas pseudo entropy, r is the distance to the cluster center, k_B is the Boltzmann constant, and T and n_e are the gas temperature and electron number density, respectively. Thus, for the condensation to happen under re-

alistic conditions, where $t_{\rm cool}/t_{\rm ff} \gg 1$, a nearly constant entropy profile is required. Early observations supported the general existence of isentropic cores in the hot gaseous halos of galaxy clusters (e.g., *Cavagnolo et al.*, 2009). However, *Panagoulia et al.* (2014) show that the flattening of inner entropy is a resolution effect, which is due to poor data quality and different methods used to obtain the temperature and density profiles. Subsequent works also confirm a universal entropy slope of $2/3$ in the inner regions of cool cores (*Hogan et al.*, 2017; *Babyk et al.*, 2018). However, turbulence in ICM may change the picture of TI development, which was originally considered in the static medium. Turbulent motions counteract the buoyant restoring force and hence weaken the effect of buoyancy damping. Therefore, cold gas condensation can nevertheless happen for $\alpha_K = r\nabla \ln K > (t_{\rm cool}/t_{\rm ff})^{-2}$. With increasing $t_{\rm cool}/t_{\rm ff}$, stronger disturbance is needed to offset the effect of buoyancy damping. As shown by the heuristic model of *Voit* (2018), the observed level of turbulence can account for the cold gas condensation when $t_{\rm cool}/t_{\rm ff} = 10 \sim 20$ and $\alpha_K \sim 2/3$.

Thus, it may be possible to describe the overall evolution of the system in the framework of the precipitation-regulated AGN feedback model. In this model, the central AGN feedback fueled by the cold gas accretion can uplift the low entropy gas to higher altitude, effectively lowering the $t_{\rm cool}/t_{\rm ff}$ of the gas. At the same time, the disturbed ICM in the inner $\alpha_K \sim 2/3$ region can become thermally unstable and the cold gas can condense out from the hot halo. These processes produce cold gas that further powers the central engine, until the AGN feedback heats the ICM to the extent where the $t_{\rm cool}/t_{\rm ff}$ of the halo is globally too large to generate cold gas either by uplift or condensation. At that point, the AGN will shut down due to lack of fuel and the halo will cool down again to trigger the next cycle of the evolution. Consequently, the $t_{\rm cool}/t_{\rm ff}$ of the hot halo is regulated to be above the critical value. This value is often found to be 10 to 20 in observations.

Although the observations are broadly consistent with the precipitation model, there are some discrepancies on a detailed level, which may have significant consequences. For example, (1) numerical simulations of the precipitation-regulated AGN feedback (e.g., *Li*

et al., 2015; *Prasad et al.*, 2015; *Ruszkowski et al.*, 2017a) often show large fluctuations in the radial profiles of thermal quantities during the AGN active phases, while observations suggest the hot atmospheres are rather stable despite AGN activity (*McNamara et al.*, 2016; *Hogan et al.*, 2017); (2) based on the analysis of the observational data performed by *McNamara et al.* (2016), there is a fundamental relationship between the hot gas cooling times and the presence of cold filaments. Dividing the cooling time by the free-fall time only increases the scatter of these correlations. Therefore, in order to reconcile the theoretical TI models with the observations, additional factors may need to be considered in the theoretical models. These factors include but are not limited to density fluctuations (*Choudhury et al.*, 2019; *Esmerian et al.*, 2021), magnetic fields (*Ji et al.*, 2018), and cosmic rays (*Kempski and Quataert*, 2020; *Butsky et al.*, 2020). All of these factors could modify the criteria for triggering of TI.

1.2.3 Numerical investigations of the evolution of gaseous halos

Numerical simulations of the evolution of gaseous halos in ETGs have been extensively discussed in the literature. Early one-dimensional calculations (e.g., *Mathews and Loewenstein*, 1986; *Loewenstein and Mathews*, 1987; *Ciotti et al.*, 1991) considered hot gas flow effected by stellar mass loss and type Ia supernovae in early type galaxies. Following *Ciotti et al.* (1991), a number of authors studied the evolution of gaseous halos of ETGs using hydrodynamic simulations including feedback from central supermassive black holes (*Ciotti and Ostriker*, 2001, 2007; *Ciotti et al.*, 2010, 2017). These works considered progressively more realistic models that included star formation and stellar feedback, and more sophisticated prescriptions for the AGN feedback – from radiative heating alone to the combination of radiative and mechanical feedback.

Recent high-resolution simulations of the feedback operating in the presence of precipitation (e.g., *Gaspari et al.*, 2012a; *Li and Bryan*, 2014a,b; *Li et al.*, 2015; *Yang and Reynolds*, 2016; *Prasad et al.*, 2015, 2018) demonstrate that the mechanical AGN feedback in the form

of bi-polar jets is able to maintain overall thermal equilibrium of the gaseous halos in a self-regulated manner. The modelled AGN feedback is fueled by the accretion of cold gas that condenses out of the hot halo and falls toward the vicinity of central supermassive black hole.

1.3 Turbulence in the ICM

Turbulence in the multiphase ICM is observed by direct and indirect ways. Indirect approaches include methods based on the surface brightness fluctuations (*Gaspari and Churazov*, 2013; *Zhuravleva et al.*, 2014), resonance scattering (*Ogorzalek et al.*, 2017), and Sunyaev-Zeldovich (SZ) fluctuations (*Battaglia et al.*, 2012). The first direct observation of turbulence was obtained by the Hitomi telescope, which measured the Doppler line broadening of the Fe XXV and Fe XXVI emission lines in the ICM of the Perseus cluster (*Hitomi Collaboration et al.*, 2016). Recently, *Li et al.* (2020) directly probed the turbulence in the cold ICM by measuring the velocity structure functions of the cold ICM filaments using optical spectroscopic data. These measurements suggest the turbulence in the galaxy clusters should be very subsonic and the turbulent pressure should be very small compared to the thermal pressure of the ICM.

Interestingly, by assuming a one-to-one conversion factor of density fluctuations observed in residual X-ray brightness map to the velocity fluctuation caused by turbulence, i.e., $\delta\rho_l/\rho = \delta v_l/c_s$, where ρ is the gas density, c_s is the sound speed, and $\delta\rho_l$, δv_l are the density and velocity fluctuations on length scale l, respectively, *Zhuravleva et al.* (2014) derive the velocity power spectra of the hot ICM in the Perseus and Virgo clusters. The resultant velocity power spectra are broadly consistent with the *Kolmogorov* (1941) prediction, i.e., $v_l \propto l^{1/3}$. Based on the derived velocity power spectra, *Zhuravleva et al.* (2014) estimate the turbulent dissipation rate v_l^3/l, and find that it can balance the radiative cooling rate as a function of the distance from cluster centers. Therefore, their results suggest that turbulent dissipation can be the dominant mechanism for energy transfer from

the AGN outflows to the hot ambient ICM. However, subsequent studies are in tension with this conclusion. For example, by statistically analyzing a large set of hydrodynamical cluster simulations, *Valdarnini* (2019) find that the turbulent velocity is too small to make significant contribution to the thermal energy budget of the cluster cores. Similar results were reported by other teams simulating the self-regulated AGN feedback in the ICM (*Li et al.*, 2017; *Yang and Reynolds*, 2016). Moreover, *Mohapatra and Sharma* (2019) find that for the dissipation of subsonic turbulence to balance radiative losses, the turbulent mixing time must be shorter than radiative cooling time. This would imply that no TI could operate in the cool core contrary to what is observed.

The tension between *Zhuravleva et al.* (2014) hypothesis and the results mentioned above may be due to the following reasons:

1. The observed density fluctuations may not be proportional to the turbulent velocity fluctuations. As shown by the simulations in *Mohapatra et al.* (2020), the gravitational stratification (i.e., the effect of gravitational field on shaping the profiles of thermodynamical quantities in order to enforce global hydrostatic equilibrium), can affect the amplitude of density fluctuations. Generally, strong stratification leads to larger density fluctuations for given root-mean-square velocity fluctuations. Thus, density fluctuations can overestimate the velocity fluctuations and hence the turbulent dissipation rate in the strongly stratified ICM and in particular in the central region, where stratification is the strongest. Furthermore, density fluctuations can arise due to factors other than turbulence, such as, e.g., contact discontinuities at the boundary between AGN-inflated bubbles and the ambient ICM.

2. Turbulent dissipation rate may not be well described by the v_l^3/l law. As shown by *Pouquet et al.* (2018), gravitational stratification affects the ratio (denoted by β therein) between the actual turbulent dissipation rate and v_l^3/l. In particular, they find a simple scaling relation $\beta \sim Fr$ in a medium range of Fr, $0.01 \lesssim Fr \lesssim 0.2$,

where $Fr = \frac{u_{\rm rms}}{\omega_{\rm BV} l_{\rm drive}}$ is the Froude number, $\omega_{\rm BV} = \sqrt{\frac{g}{\gamma}\left(\frac{\partial \ln P}{\partial r} - \gamma \frac{\partial \ln \rho}{\partial r}\right)}$ is the Brunt–Väisälä frequency, $u_{\rm rms}$ is the root mean square velocity of the turbulence, $l_{\rm drive}$ is the driving scale of the turbulence, $\gamma = 5/3$ is the adiabatic index, ρ is the gas density, P is the gas pressure, and g is the gravitational acceleration. The *Pouquet et al.* (2018) simulations are not tailored to the galaxy cluster environments, but this scaling relation may nevertheless hold. Therefore, further numerical simulations with cluster initial conditions are needed to test and calibrate this scaling relation.

3. When turbulence is present in an entropy-stratified medium, turbulent mixing leads to energy transfer that can effectively result in additional heating on top of turbulent dissipation. Observations reveal that there is a universal positive entropy gradient in the hot ICM (*Babyk et al.*, 2018). Turbulent eddies cause the high entropy gas at larger radii to mix with the low entropy gas at smaller radii. Thus, this process results in a net inflow of gas internal energy and heating the gas in the center.

1.4 Thesis outline

In Chapter II, I study the observed "multiphase" and "single-phase" dichotomy (*Werner et al.*, 2014; *Voit et al.*, 2015b) in the gaseous halos in giant elliptical galaxies. I find that the self-regulated momentum-driven AGN feedback is able to maintain this observed dichotomy. However, the long-term evolution of the systems reveals the formation of long-lived massive cold disks. Such disks are seen in many other numerical simulations in the literature but are in tension with the observations. Thus, in Chapter III, I explore the possible solution to this "disk problem." I find that magnetic fields provide one such solution. Although weak in the hot gas, the magnetic fields are amplified in the cold gas and effectively reduce the angular momentum of the cold gas, thus preventing the formation of the problematic disks. Additionally, I find that when the plasma composition in the AGN jets is dominated by CRs and CRs transport is included, the hot gaseous halo can maintain

global thermal equilibrium and the massive cold central disks do not form (without CR transport the hot halos exhibit massive cooling flows in disagreement with observations). The AGN power is reduced as its energy is utilized more efficiently in the presence of CR transport. Motivated by the finding from Chapter III that the magnetic fields have important dynamical impact on the cold gas, and by recent observational work on probing the ICM turbulence using the velocity structure function of the cold ICM filaments (*Li et al.*, 2020), in Chapter IV I study the properties of turbulence in the multiphase ICM by calculating the velocity structure functions of different phases in the simulated ICM affected by the AGN feedback. I find that while the simulated turbulence is not consistent with the predictions from the *Kolmogorov* (1941) theory, it is broadly consistent with the observations. I suggest a novel hypothesis supported by our simulations, that the turbulence of the hot gas at the ICM center is driven both by the AGN outflows and the cold filaments formed via TI. In Chapter V, I study the energetic impact of turbulence on the heating–cooling balance in the ICM and present an analytic model that quantitatively describes the heating rate due to turbulent dissipation and turbulent mixing. I elucidate the important role of gravitational stratification in regulating the heating rates. Thesis summary and future work are presented in Chapter VI.

CHAPTER II

AGN Feedback and Multi-phase Gas in Giant Elliptical Galaxies

2.1 Preface

The results presented in this chapter were published in: *Wang, Chaoran, Yuan Li, and Mateusz Ruszkowski. "AGN feedback and multiphase gas in giant elliptical galaxies." Monthly Notices of the Royal Astronomical Society 482.3 (2019): 3576-3590* and are reproduced here with minor style revisions.

2.2 Abstract

Recent observations have found extended multiphase gas in a significant fraction of massive elliptical galaxies. We perform high-resolution three-dimensional hydrodynamical simulations of two idealized elliptical galaxies – one representing a typical galaxy characterized by initial conditions conducive to the development of thermal instability and the other one less likely to develop thermal instability – in order to study the development of thermal instability and the formation of multiphase structures. We analyze the interplay between radiative cooling, momentum-driven AGN feedback, star formation, and stellar feedback from both young and old stars. We find that in one class of elliptical galaxies, the entropy of the hot halo gas rises sharply as a function of radius, and the hot halo is thermally stable

and run-away cooling can only happen in the very center of the galaxy. In other class of ellipticals, the hot halo gas has a cooling to free-fall time ratio close to 10, and the non-linear perturbation driven by AGN feedback can cause the hot gas to frequently precipitate into extended multiphase filaments. Both multi- and single-phase elliptical galaxies experience cooling-driven AGN feedback cycles. Interestingly, AGN feedback maintains the multi- or single-phase nature of the halo but does not turn multiphase galaxies into single-phase ones or vice versa. Some of the extended cold gas in the multiphase galaxy also forms young stars. The level of star formation and its spatial distribution are in excellent agreement with *Hubble* observations of nearby elliptical galaxies.

2.3 Introduction

The evolution of galaxies is heavily shaped by the supermassive black holes (SMBHs) in their centers (see review by *Kormendy and Ho*, 2013). In today's universe, most elliptical galaxies have little ongoing star formation. To maintain this quiescent state, the energy input from the central SMBHs via the active galactic nuclei (AGN) feedback is needed for mainly two reasons. First, the cooling time of the interstellar medium (ISM) in the center of elliptical galaxies is short. In the absence of heating, a classical cooling flow is expected to develop in the center of the galaxy (*Fabian*, 1994). The classical cooling flow model overpredicts the star formation rates both in the center of elliptical galaxies and clusters (e.g., *David et al.* 2001; *Bregman et al.* 2005; *Mathews and Brighenti* 2003; *Bregman and Lloyd-Davies* 2006; *Sanders et al.* 2008). The solution to this "cooling flow problem" is some form of heating to offset radiative cooling. AGN feedback is the most plausible solution due to its high efficiency and self-regulating nature (*McNamara and Nulsen*, 2007).

In addition to solving the "cooling flow problem," AGN feedback is also needed to remove stellar ejecta out of the galaxies. Old stars lose a significant fraction of their original mass to the ISM via stellar winds during the asymptotic giant branch (AGB) phase. The stellar ejecta need to be removed to maintain the observed low density halo (*Mathews and*

Baker, 1971). Because of the high velocities of the AGB stars themselves (the velocity dispersion of the stars is similar to the velocity dispersion of the hot halo gas), the stellar wind likely thermalizes to the virial temperature of the halo quickly, and this process alone provides a small but non-negligible amount of heating (*Mathews*, 1990; *Conroy et al.*, 2015) [1]. Type Ia SNe (SNIa) explosions inject more thermal energy than thermalized stellar winds, but still do not provide enough energy needed to drive a galactic wind and sweep stellar ejecta out of the galaxy (*Mathews and Brighenti*, 2003; *Ciotti et al.*, 2017). Cosmological simulations also find that stellar feedback alone cannot prevent late time star formation in massive elliptical galaxies, and that AGN feedback is still needed to maintain the quiescent state (*Sijacki et al.*, 2007; *Weinberger et al.*, 2017b).

Accretion onto SMBHs can be dominated by the "hot mode" described in the Bondi-Hoyle accretion model (*Bondi*, 1952), or by the "cold mode", assuming that the hot gas first fragments and falls onto the black hole as cold clouds (*Balbus and Soker*, 1989; *Pizzolato and Soker*, 2005). Recent Chandra observations of hot X-ray gas in close vicinity of some nearby SMBHs contradict the classical "Bondi" model predictions (*Baganoff et al.*, 2003; *Russell et al.*, 2015). Theoretical and numerical investigations suggest that hot mode accretion onto SMBHs is inefficient (*Yuan and Narayan*, 2014) and powerful AGN feedback is likely triggered by cold mode accretion (*Gaspari et al.*, 2013; *Voit et al.*, 2015a).

There is growing observational evidence for the existence of multiphase gas in many elliptical galaxies. It has been known for a long time that a significant fraction of elliptical galaxies have dust in their cores (*van Dokkum and Franx*, 1995; *Lauer et al.*, 2005) and the dust is suggested to be linked to AGN activities (*Martini et al.*, 2013). Recent surveys have found both molecular and warm ionized gas in nearby early-type galaxies (*Young et al.*, 2011; *Pandya et al.*, 2017). Cold gas has also been detected in significant amounts in the circum-galactic medium (CGM) of early type galaxies (*Werk et al.*, 2014). Some of the

[1] Stellar wind heating only increases the total amount of thermal energy per unit volume, but does not increase the specific thermal energy (per unit mass), and thus cannot provide extra energy to do the work required to remove the stellar winds.

cold gas in elliptical galaxies is also turning into stars as is suggested by UV observations (*Yi et al.*, 2005). Recent Hubble observations have directly detected young stars in several nearby elliptical galaxies (*Ford and Bregman*, 2013). The estimated star formation rate is rather low (on the order of $\sim 10^{-4}$ $M_\odot \cdot yr^{-1}$), but the existence of young stars and star clusters indicate that many elliptical galaxies are not completely "red and dead."

The effects of different modes of AGN feedback have been studied in many one- and two-dimensional numerical simulations (*Ciotti and Ostriker*, 1997; *Ciotti et al.*, 2017; *Li et al.*, 2018b). In the past few years, cosmological simulations have found that mechanical AGN feedback is more effective at ejecting gas out of the halo and suppressing late-time star formation than pure thermal feedback, resulting in early-type galaxy properties that are more consistent with the observations (*Choi et al.*, 2012; *Pillepich et al.*, 2017). *Gaspari et al.* (2012a); *Eisenreich et al.* (2017) have studied the interplay between cooling and AGN feedback in more detail using idealized three-dimensional simulations of elliptical galaxies, but neither work focuses on the multiphase gas due to limited resolution or treatment of cold gas.

Recent observations of a sample of nearby elliptical galaxies show that about half of them host spatially extended multiphase gas, while the rest have single-phase halos (*Werner et al.*, 2012, 2014) [2]. *Voit et al.* (2015b) theorizes that in single-phase elliptical galaxies, AGN and SNIa together can drive outflows that sweep stellar ejecta out of galaxies, keeping the ISM in a single phase with only hot gas; in multiphase elliptical galaxies, SNIa heating is weaker, and thermal instability can develop to form multiphase gas (*McCourt et al.*, 2012; *Sharma et al.*, 2012), but precipitation-triggered AGN feedback helps prevent further cooling and keeps the galaxies generally "quenched."

In this paper, we carry out 3D adaptive mesh refinement (AMR) simulations to study AGN feedback and multiphase gas in two idealized elliptical galaxies based on the observations of NGC 5044 and NGC 4472. NGC 5044 is a multiphase galaxy (MPG) in *Werner*

[2]Note that galaxies with cold gas detected only in the nuclei are classified as single-phase galaxies; only galaxies with extended Hα emission are classified as multiphase galaxies.

et al. (2014), and NGC 4472 is a single-phase galaxy (SPG). We adopt the momentum-driven mechanical AGN feedback model powered by cold-mode accretion, which has been used in our previous simulations of cool-core galaxy clusters (*Li and Bryan*, 2014a,b; *Li et al.*, 2015) and successfully reproduced many observed features including filamentary multiphase gas and star formation (*Donahue et al.*, 2015b; *Tremblay et al.*, 2015). Other important physical processes included in the simulations are self-gravity, radiative cooling, feedback from the old stellar population (stellar wind and SNIa), and star formation and feedback from Type II supernovae. The key questions we try to address are: (1) How do SMBH feeding and feedback relate to thermal instabilities and multiphase ISM in elliptical galaxies? (2) How does the AGN feedback affect the hot halo gas and drive galactic wind? (3) What causes the difference between multi- and single-phase galaxies? (4) What is the level of star formation and where do young stars form?

The paper is structured as follows: in Section 2.4, we describe the simulation setup and how different physical processes are modeled; the main results of the simulations are presented in Section 2.5, including the development of thermal instabilities, AGN-driven galactic wind, and star formation; in Section 2.6, we discuss the caveats of the simulations reflected in the long term evolution of the galaxies, present our resolution and parameter studies, and compare our results with cluster simulations and other elliptical galaxy simulations. We summarize our work in Section 2.7.

2.4 Methodology

Our three-dimensional simulations are performed using the adaptive mesh refinement (AMR) code ENZO (*Bryan et al.*, 2014) with the ZEUS hydrodynamic method (*Stone and Norman*, 1992). The simulation domain is a 16 Mpc^3 cube with 64^3 root grids and a maximum of 11 refinement levels. Therefore, the size of the smallest cell is $\Delta x_{\mathrm{min}} = 16\ \mathrm{Mpc}/64/2^{11} \approx 122$ pc. We follow the refinement criteria used in galaxy cluster simulations (*Li and Bryan*, 2012, 2014a,b; *Li et al.*, 2015). Detailed descriptions of

the refinement criteria can be found in *Li and Bryan* (2012). Here we only repeat the key points. A non-maximum-refined cell is refined if (1) the cell mass is larger than one-fifth of the gas mass in one cell of the root grid; (2) the ratio of gas cooling time to sound-crossing time of the cell is smaller than 6 (we use a somewhat arbitrary value larger than 1 to better resolve cooling); (3) the size of the cell is larger than four times the local Jeans length.

In addition to AMR, we place a nested set of static refined boxes in the central area of the simulation domain. The boxes are placed such that the minimum level of refinement increases from 7 at $r = 100$ kpc to 11 at $r = 0.8$ kpc. This ensures that the AGN jet launching region is always refined to the highest level and that the inner halo is reasonably well resolved even in the absence of cold gas.

To better resolve the onset of cooling instability and the multiphase structures, we use the "super-Lagrangian" refinement as described in *Li and Bryan* (2012). This makes the maximum mass of cells decrease with increasing refinement levels. In our standard simulation, the maximum cell mass at $l = 11$, our highest level of refinement, is $\sim 1.8 \times 10^5$ $M_\odot$. However many cells in the simulations have much smaller masses ($\sim 10^2$ $M_\odot$), partially owning to our static refined boxes.

We model two idealized elliptical galaxies. The initial conditions are described in §2.4.1. Important physical processes in our simulations include radiative cooling, self-gravity, momentum-driven AGN feedback, feedback from evolved stars, and star formation, and Type II supernova feedback from young stars. For radiative cooling, we calculate the cooling function derived from the Table 4 of *Schure et al.* (2009) for $T > 10^4$ K and extend it down to 300 K using the cooling rates given by *Rosen and Bregman* (1995). In §2.4.2, we describe in detail how we model the other physical processes.

2.4.1 Galaxy Initial Conditions

Our MPG and SPG are modeled to agree with NGC 5044 and NGC 4472, respectively. Both of them are central dominant galaxies of low-mass groups. NGC 5044 has extended

multiphase gas and NGC 4472 is observed to be a single-phase elliptical galaxy. We choose them as representatives of multi- and single-phase galaxies, and refer to them as MPG and SPG throughout the paper instead of using their actual names.

We model the two galaxies in a similar fashion. Both galaxies are initially spherically symmetric and in hydrostatic equilibrium. The gravitational potential for each galaxy consists of self-gravity of the gas and three static components: dark matter, stars, and the central black hole. The dark matter halo is described by an NFW profile (*Navarro et al.*, 1997), which is characterized by the virial radius $r_{\rm vir}$, virial mass $M_{\rm vir}$, and the concentration parameter c.

The stellar density profile, $\rho_*(r)$ is described by a spherically symmetric de Vaucouleurs profile with a power-law core in the inner region:

$$\rho_*(r) = \begin{cases} \rho_{\rm deV}(r; r_e, M_*), & r > r_c \\ \rho_{\rm deV}(r_c; r_e, M_*)(r/r_c)^{-0.9}, & r \leqslant r_c \end{cases}, \tag{2.1}$$

where r_e is the effective radius and M_* is the total stellar mass. The approximate de Vaucouleurs profile is adopted from *Terzić and Graham* (2005).

The central black hole is treated as a point source of gravity with mass $M_{\rm BH}$. We adopt the NFW parameters from *Mathews and Brighenti* (2003) for the SPG and from *Valentini and Brighenti* (2015) for the MPG. The parameters for modeling the gravity potential for SPG and MPG are listed in Table 2.4.1.

The properties of the hot halo gas are modeled according to the X-ray observations of the two galaxies (SPG: *Irwin and Sarazin* 1996; *Werner et al.* 2012, and MPG: *Buote et al.* 2003a, 2004; *Werner et al.* 2014). For each galaxy, we first fit the temperature data using an analytical expression. We then calculate the density profile assuming hydrostatic equilibrium, normalizing it to match the observed data, shown in Figure 2.1. We do not put in any multiphase gas by hand in the initial setup.

For both galaxies, we set the metallicity of the gas to be a constant solar abundance.

This simplistic assumption is consistent with the X-ray observations of the central several tens kpc regions of both galaxies (for SPG, *Athey* 2007; *Humphrey et al.* 2006; for MPG, *Buote et al.* 2003b; *Komiyama et al.* 2009).

Model	Name	r_e (kpc)	M_* ($10^{11}M_\odot$)	r_c	c	$M_{\rm vir}$ ($10^{13}M_\odot$)	$r_{\rm vir}$ (kpc)	$M_{\rm BH}$ ($10^8M_\odot$)
(1)	(2)	(3)	(4)	(5)	(6)	(7)	(8)	(9)
SPG	NGC 4472	8.57	7.26	0.2	6.7	4	700	5.6
MPG	NGC 5044	10	3.5	0	8.5	4	900	4

Table 2.1: Gravitational potential parameters. Note. (1) Model name: SPG is the single-phase galaxy, and MPG is the multiphase galaxy, (2) Name of the galaxies: SPG is modeled to agree with NGC 4472 and MPG with NGC 5044, (3) Effective radius, (4) Total stellar mass, (5) Radius of the power-law core of the stellar density profile, (6) Dark matter halo concentration parameter, (7) Total halo mass within the virial radius, (8) Virial radius, (9) Black hole mass. See §2.4.1 for more details.

2.4.2 Physical Processes

2.4.2.1 AGN feedback

The way we model the AGN feedback is similar to that of *Li and Bryan* (2014a,b). Here we only repeat the key points.

The SMBH is located in the center of the galaxy. In order to model the black hole accretion, at each time step (Δt) we calculate the mass accretion rate ($\dot{M}_{\rm acc}$) by dividing the total cold gas mass within the central vicinity ($r < 500$pc) by the local characteristic free-fall time (5 Myr). After this time step, $\dot{M}_{\rm acc}\Delta t$ of cold gas in this region is removed.

We model the AGN jets as bipolar outflows launched along the $z-$axis from a pair of jet launching planes. The two jet launching planes are both parallel to the x-y plane and located at the center of the simulation domain. Mass (Δm) is loaded onto the launching planes at each time step following a distribution of $\Delta m \propto \exp\left[\frac{-r^2}{2r_{\rm jet}^2}\right]$, where $r \leqslant 2r_{\rm jet}$ is the distance from the z-axis and $r_{\rm jet} = 1.5\Delta x_{\rm min}$. The total amount of launched gas is normalized to be equal to that of the gas removed in the accretion process, namely $\int_{r\leqslant 2r_{\rm jet}} \Delta m = \dot{M}_{\rm acc}\Delta t$. That

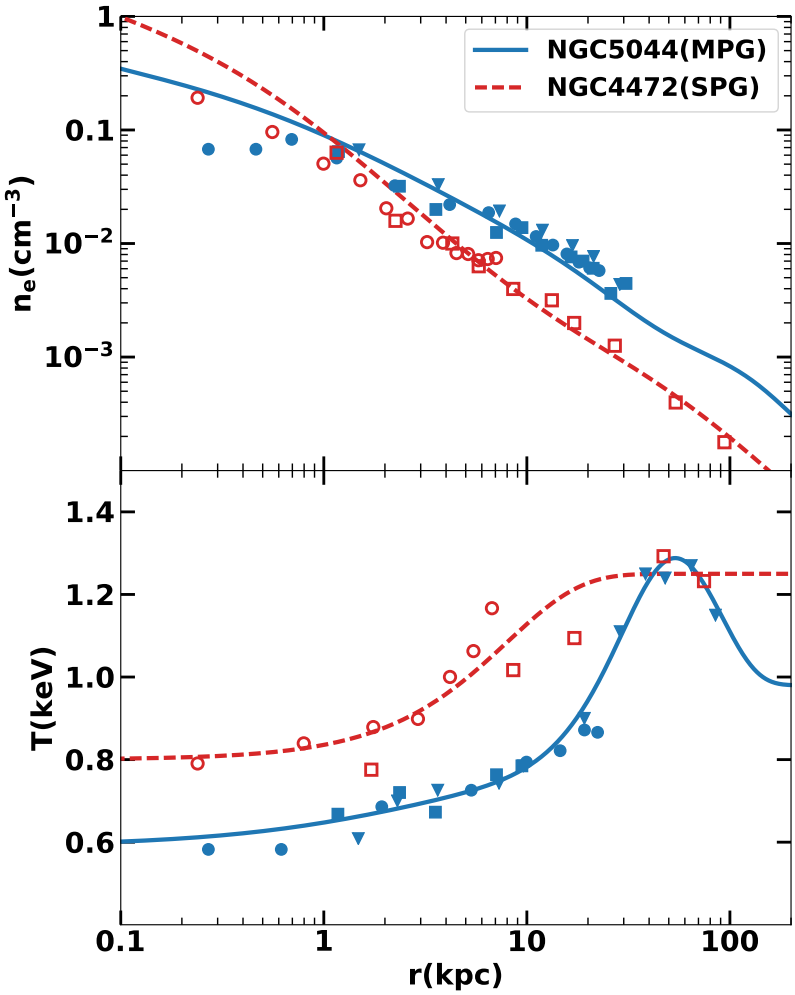

Figure 2.1: The initial conditions of the two galaxies. Upper panel: the initial electron density profiles of the simulated MPG (NGC 5044, solid blue line) and SPG (NGC4472, dashed red line). The blue points are the observed data for the MPG from *Buote et al.* (2003a) (filled triangles), *Buote et al.* (2004) (filled squares), and *Werner et al.* (2014) (filled circles). The red points are for the SPG from *Irwin and Sarazin* (1996) (open squares) and *Werner et al.* (2012) (open circles). Lower panel: the initial temperature profiles and the observed X-ray data. Color scheme and line styles are the same as in the upper panel.

is, we assume that only a very small amount of gas is actually accelerated onto the SMBH.

The jet power is given by

$$P_{\rm jet} = \epsilon \dot{M}_{\rm acc} c^2. \tag{2.2}$$

The feedback efficiency ϵ is 0.5% in our standard runs. We further assume that 10% of the jet power is thermalized (put in as thermal energy) and the remaining 90% is put in as kinetic energy. In our standard simulations, the jet precesses at a small angle ($\theta = 0.15$ radian) with a period of 10 Myr. This small precession angle and the exact value of the thermalization fraction of the jet do not have a significant impact on the simulation results. We discuss the impact of the choice of parameters, including the feedback efficiency, in Section 2.6.2.

2.4.2.2 Feedback from old stars

For the feedback from old stellar population, we consider the mass and energy input from stellar wind and energy feedback from type Ia supernovae (SNe Ia). The mass loss from old stars are described by a specific mass ejection rate $\alpha = 10^{-19}$ s^{-1}, so that the amount of the ejected matter per unit volume per unit time is $\alpha\rho_*$. The ejected matter is assumed to be thermalized to the stellar virial temperature (*Mathews and Brighenti*, 2003). We adopt $\sigma = 300$ km $\cdot$ s^{-1} which is a typical value for group centrals.

The SNe Ia feedback from old stars is modeled by injecting pure thermal energy to the ISM. The energy injection is azimuthally uniform, with its rate proportional to the stellar density. The energy input is 10^{51} ergs per SN explosion. The specific SNe Ia rate is 3×10^{-11} kyr^{-1} $\cdot$ M$_\odot{}^{-1}$, which is the value used in *Voit et al.* 2015b and is broadly consistent with the observations (*Maoz et al.*, 2012). With these parameters, SNIa heating rate is about 5 times the heating rate of the thermalized stellar wind.

2.4.2.3 Star formation and stellar feedback

Star formation and feedback from young stars are modeled in the same way as in *Li et al.* (2015). We model star formation following *Cen and Ostriker* (1992) with stochastic formation of star particles. A star particle is created if the following criteria are satisfied in a cell: (1) the gas is denser than a critical density (we use 1.67×10^{-24} g $\cdot$ cm^{-3} in our simulations), (2) the cell mass exceeds the local Jeans mass, (3) the flow is convergent, and (4) $t_{\rm cool}/t_{\rm collapse} < 1$ where $t_{\rm collapse} = \sqrt{3\pi/(32G\rho_{\rm gas})}$. The mass of the created star particle is $m_* = 0.02 m_{\rm cell}\Delta t/t_{\rm collapse}$ if $m_* > m_{*\rm min} = 10^5$ M$_\odot$, where $m_{\rm cell}$ is the cell mass and Δt is one computational time step. For cells which meet the four criteria but have $m_* < m_{*\rm min}$, star particles are formed stochastically with a possibility of $m_*/m_{\rm min}$; and the mass of the particle is $\min(0.8m_{\rm cell}, m_{*\rm min})$. This stochastic procedure is used to prevent forming too many star particles. We further consider stellar feedback including mass loss and Type II supernova from the created stars. For the mass loss, we let the created stars return 25% of their mass to the gas phase; for Type II supernova feedback, 10^{-5} of their rest-mass energy is injected as thermal energy to local cells.

2.5 Results

In this section we discuss the properties of the two simulated galaxies over 1.5 Gyr. §2.5.1 describes the general gas evolution in MPG and SPG, and in §2.5.2 we analyze the development of thermal instabilities and the formation of cold gas in the two system. In §2.5.3 we discuss the how gas sweeping is achieved in the two simulated galaxies and compare it with the theoretical analysis in *Voit et al.* (2015b). We discuss star formation in our simulated galaxies and compare it with observations in Section 2.5.4, and in Section 2.5.5 we discuss the velocity dispersion of the hot ISM.

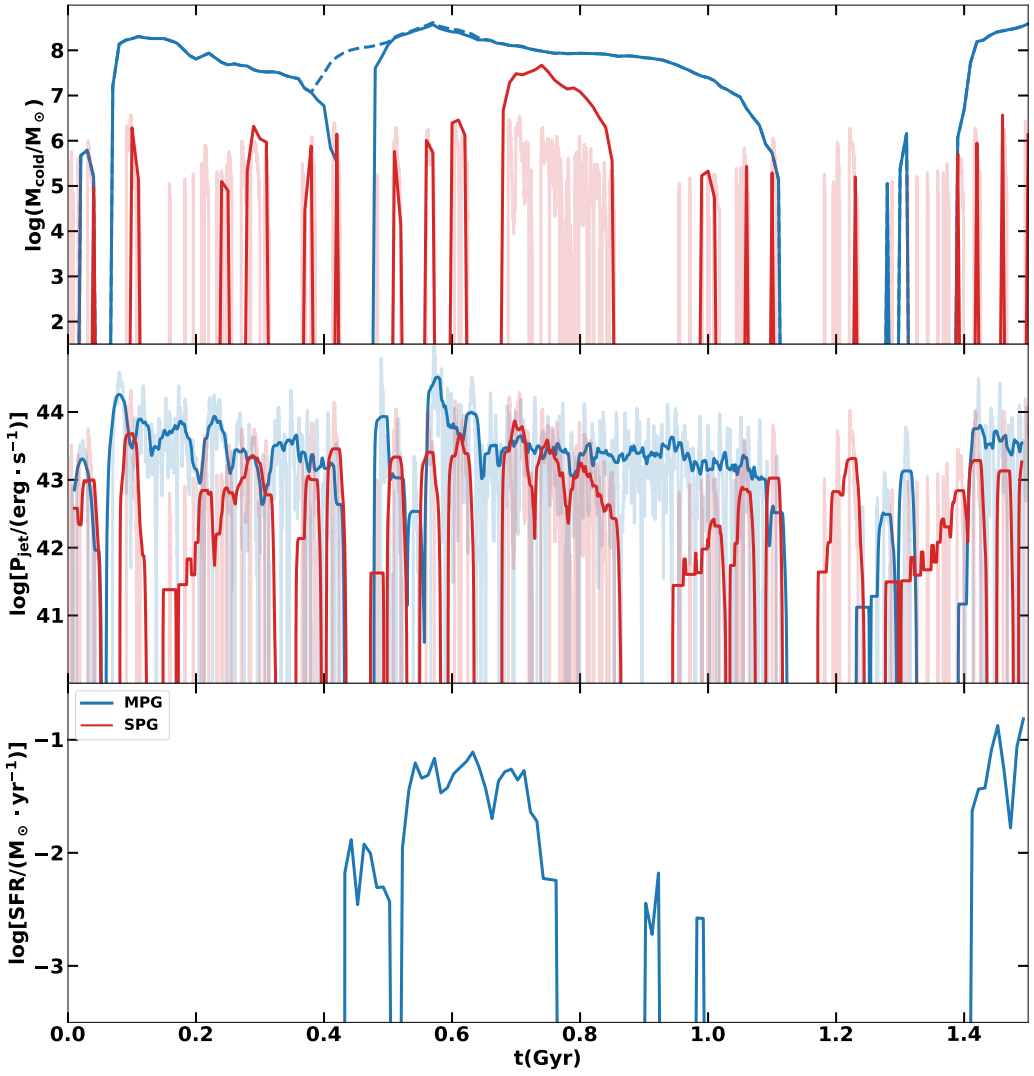

Figure 2.2: From the top to bottom panel: the evolution of cold gas mass, jet power, and star formation rate in the two simulated galaxies. Red color corresponds to the SPG and blue to the MPG. In the top panel, the solid blue line corresponds to the cold gas within $r < 10$ kpc region; and the dashed line corresponds to the total amount of the cold gas in the galaxy. Simulation data are sampled every 10 Myr. For clarity, we show the instantaneous cold mass within SPG's accretion zone in faint red in the top panel. Some short-lived cold gas is not captured by the 10Myr sampling. In the middle panel, we show the instantaneous jet power in lighter color, and add solid lines that are averaged with a 20-Myr moving window.

2.5.1 General properties of the evolution of the galaxies

2.5.1.1 multiphase Galaxy (NGC 5044)

In the MPG, the system goes through several major precipitation cycles with AGN activities and extended multiphase gas. At the beginning of the simulation, AGN feedback is off. Radiative cooling causes gas to condense in the center of the galaxy almost immediately after the simulation starts. This is because in our initial setup, cooling time decreases towards the center monotonically. If we keep AGN feedback off, a classical cooling flow develops in the center of the galaxy, which we have verified numerically. In our standard run with AGN feedback, condensation near the SMBH triggers AGN feedback, which quickly heats up the gas in close vicinity to the SMBH. This small amount of energy injection, however, only delays further condensation by $\sim$ 30 Myr as is shown in Figure 2.2. At $t \approx 70$ Myr, a major precipitation event occurs in the center of the galaxy with a multiphase structure that extends out to $\sim$10 kpc, which triggers a strong AGN outburst. The gas falls toward the SMBH, and swirls around it as it gradually feeds the SMBH. Meanwhile, more gas continues to precipitate within $r < 10$ kpc and continues to power AGN feedback. The mechanical AGN feedback generates shock waves that heat up the ISM as they propagate through the halo. These shock waves also create low density, high temperature regions that resemble X-ray bubbles often observed in these systems (see a snapshot of the projected gas density during this period in the first panel of Figure 2.3). Interestingly, even though star formation is allowed to happen, no star particle forms in this first cycle of precipitation in spite of the presence of multiphase gas (third panel of Figure 2.2).

At $t \approx 400$ Myr, all the cold gas near the SMBH has been accreted or turned into stars, which turns off AGN feedback. At the same time, a parcel of low entropy gas that has been lifted up by previous AGN activities starts to condense at $r \approx 30$ kpc. The cold gas falls to the center of the galaxy, forming stars on its way, and reignites AGN feedback, which marks the beginning of the second cycle. Precipitation continues until all the cold gas settles to a

clumpy rotating disk around the SMBH at about $t \approx 800$ Myr. The disk then shrinks as star formation and accretion onto the SMBH continues, and eventually vanishes at $t \approx 1.1$ Gyr, which shuts off AGN feedback again. This is the end of the second cycle. The top right panel of Figure 2.3 shows this brief quiescent phase.

The third cycle begins at $t \approx 1.2$ Gyr in ways very similar to the first cycle: a small amount of condensation first happens in the center, triggering a brief AGN outflow that is followed by a major precipitation and AGN outburst. We focus on the first 1.5 Gyr of the simulation and leave the evolution of the galaxy after this point for discussion in Section 2.6.1.

The cold gas mass peaks at few times 10^8 $M_\odot$, and the jet power mostly varies within $10^{43} \sim 10^{44}$ erg $\cdot$ s^{-1} (Figure 2.2). The average accretion rate is about 1% of the Eddington accretion rate. Note that the general cyclical behavior is not sensitive to simulation parameters, but details are. For example, a very small change in one simulation parameter can result in a noticeable difference (a factor of two) in the exact duration of each cycle, the exact amount and spatial extension of the multiphase gas, and whether precipitation first starts at the center or off center (though the first condensation in the simulation always starts in the center).

2.5.1.2 Single-phase Galaxy (NGC 4472)

The SPG evolves quite differently from the MPG. As in the case of the MPG, runaway cooling also happens first in the center of the galaxy, and triggers AGN feedback, but this does not lead to a major precipitation event with the formation of extended multiphase gas. Instead, after the cold gas is quickly accreted onto the SMBH and AGN is turned off, condensation occurs again in the center of the galaxy, with no spatially extended multiphase gas present. This central condensation ignites the AGN again and the galaxy continues to go through cycles of central cooling and AGN feedback. The bottom panels of Figure 2.3 show the projected gas density of the SPG when the cold gas is about to turn on the AGN

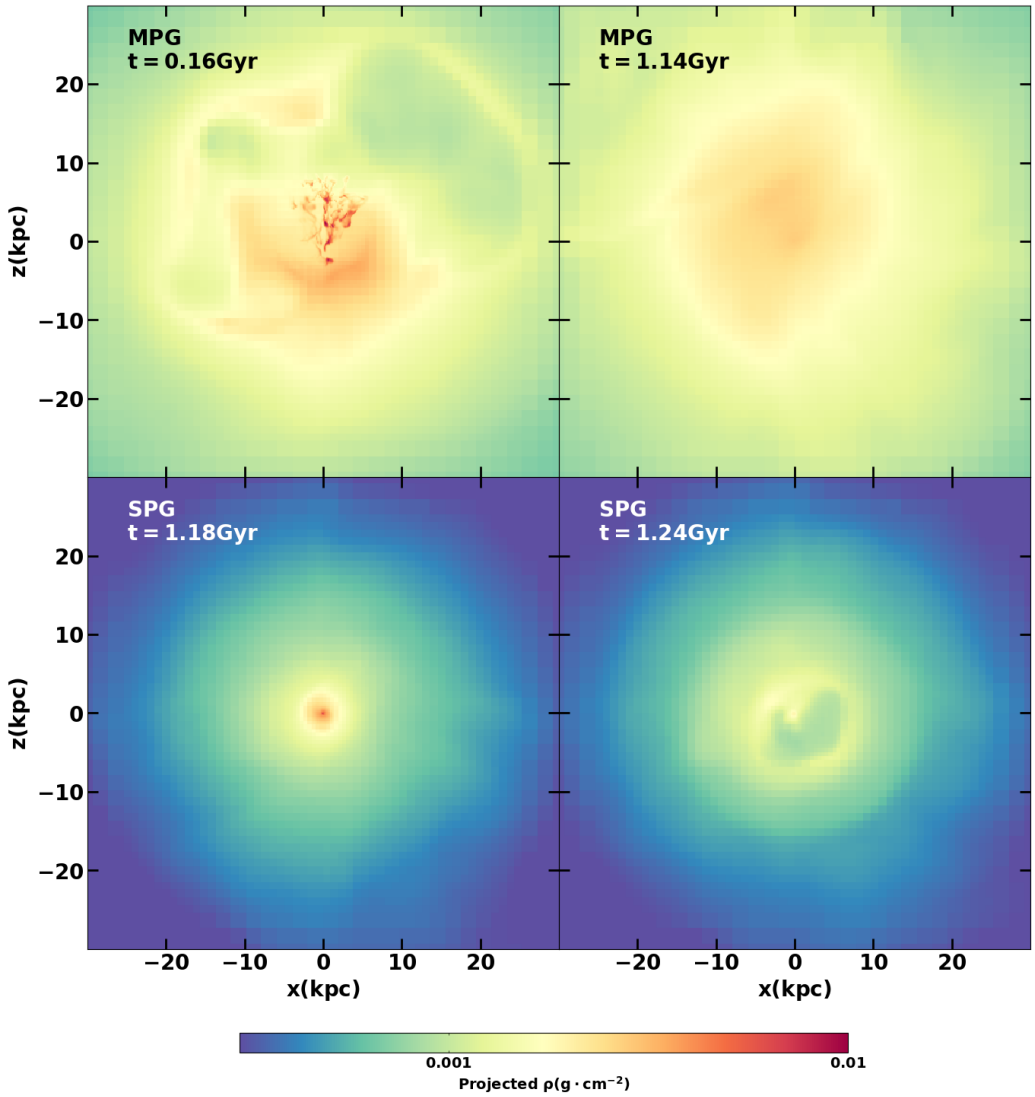

Figure 2.3: Snapshots of projected gas density in the central $(60\text{kpc})^3$ regions of MPG (top panels) and SPG (bottom panels). The projection is along the $y-$axis and the AGN jets are along the $z-$axis. Animations can be found at vimeo.com/266890265 (MPG) and vimeo.com/266890473 (SPG).

(bottom left panel) and when cold gas is gone right after an AGN outburst (bottom right penal). The peak of the AGN power approaches 10^{44} erg $\cdot$ s^{-1}, only slightly lower than the MPG, but the duration of each cycle is much shorter, typically lasting only tens of Myr or even shorter, followed by several tens of Myr pause (Figure 2.2). The average accretion rate is about 0.2% of the Eddington rate.

Within 1.5 Gyr, the SPG only shows extended multiphase gas at $t \sim 700$ Myr. The multiphase structure reaches its maximum spatial extent of ~ 12 kpc, and the amount of cold gas rises to 6×10^7 M$_\odot$. Except for this brief moment of spatially extended cooling, the galaxy never hosts more than 10^7 M$_\odot$ cold gas, and the cold gas is always only found in the nucleus of the galaxy.

Despite the drastic difference between the two galaxies in the spatial extent of the multiphase gas and the duration of individual feedback episodes, the periodicity appears universal. Both galaxies evolve through cycles of gas cooling and AGN outbursts. Within 1.5 Gyr, the averaged gas properties bounce around the initial condition for both galaxies (Figure 2.4). The density, temperature, entropy and pressure profiles of both hot halos stay rather close to their initial conditions. The entropy profile tends to flatten in the center when feedback is on. This is also seen in other simulations (e.g., *Meece et al.*, 2017). We think that this is mainly because our jet base is much wider than the real jet base due to our resolution limit. As a result, our jets likely heat up a wider region than the real jets. It is also possible that if we include additional physics such as cosmic rays, heating will be less centralized, and we will see less increase in the central entropy. We will test this in future works.

Even though large fluctuations are seen in the "true" profiles, the "observed" profiles are much smoother due to the projection effect. As an example, we show in the third row of Figure 2.4 the projected temperature profiles, close to what an observer would see. The projected temperature profiles are smoother and closer to the initial conditions than the profiles directly computed from the simulation data (the second row).

The X-ray luminosities of the two systems do not show large fluctuations either. Figure 2.5 shows the two galaxies on the $L_X - L_B$ relation. Within 1.5 Gyr of the simulations, the variation of L_X is within 28 percent of the initial condition for the MPG and 49 percent for the SPG.

2.5.2 Thermal Instabilities and multiphase ISM

In this section, we analyze our simulation results in more detail, with a focus on the multiphase ISM in the two galaxies. In particular, we discuss why thermal instabilities develop differently in the two galaxies, and compare our results with analytical work and previous numerical simulations.

The development of thermal instability in a gaseous halo is closely related to its $\min(t_{\rm cool}/t_{\rm ff})$ ratio. Recent observations suggest that there is a critical ratio of $\min(t_{\rm cool}/t_{\rm ff}) \sim 10$ where hot halos of elliptical galaxies and galaxy clusters can develop extended multiphase gas (*Werner et al.*, 2014; *Voit and Donahue*, 2015). Numerical simulations also generally agree that thermal instabilities occur when the $\min(t_{\rm cool}/t_{\rm ff})$ of the system drops below a critical value, typically between a few and 20 (*Sharma et al.*, 2012; *Gaspari et al.*, 2012a; *Li and Bryan*, 2014a; *Meece et al.*, 2015).

Our simulations confirm that elliptical galaxies develop extended multiphase gas when the azimuthally averaged ratio between cooling time and free fall time, $\langle \mathbf{t}_{\rm cool}/\mathbf{t}_{\rm ff} \rangle \approx 10$. Figure 2.6 shows the "stacked-average" $t_{\rm cool}/t_{\rm ff}$ in our two simulated galaxies. For every simulation output (every 10 Myr), we plot the distribution of X-ray luminosity-weighted $t_{\rm cool}$ as a function of radius, normalized within each radius bin. We then stack these individual plots to obtain an average distribution. The goal is to create a stacked $t_{\rm cool}$ profile similar to that observed in a sample of multiphase and single-phase ellipticals. We over-plot dashed lines representing 5, 10, 20, and 70 times the free-fall time $t_{\rm ff}(r)$.

In the MPG, the average cooling time (cyan line) of the gas is very close to the $t_{\rm ff} \times 10$ line (left panel of Figure 2.6). However, at any radius, the distribution of $t_{\rm cool}$ extends well

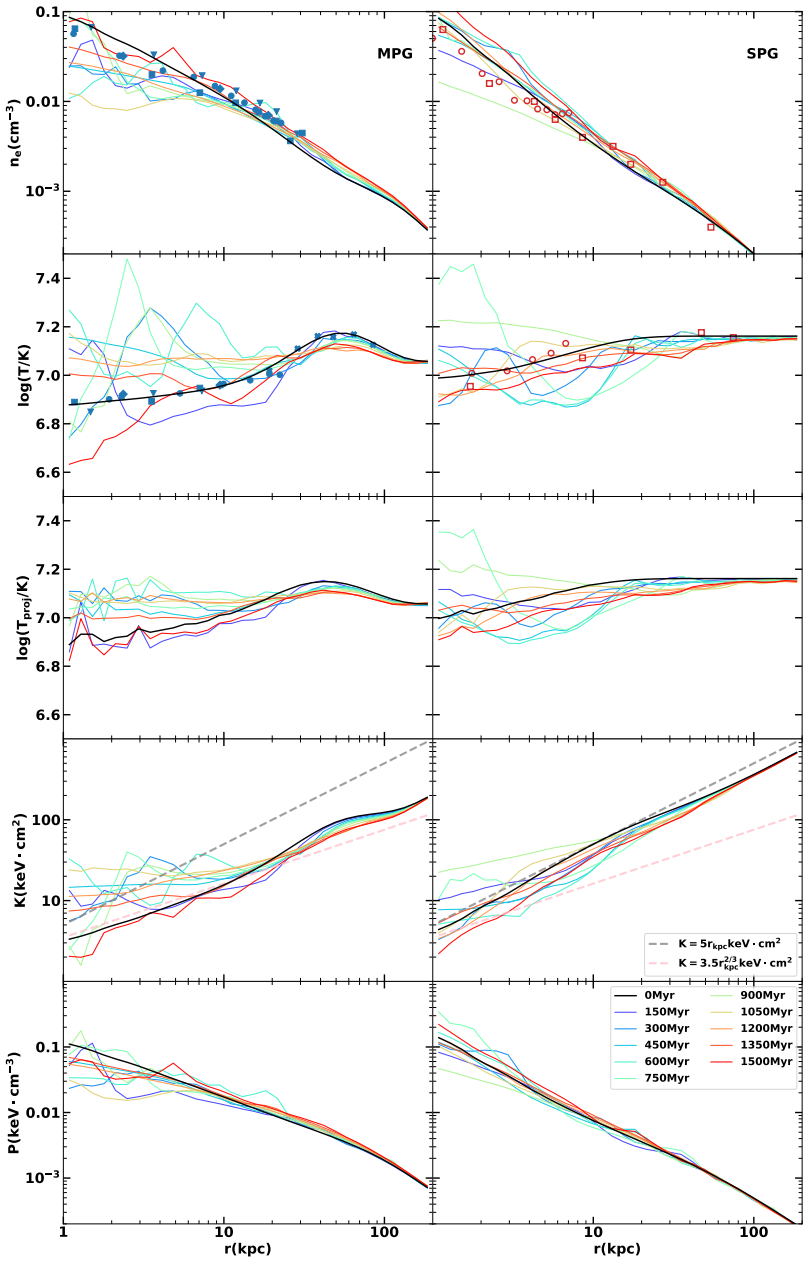

Figure 2.4: From top to the bottom: the electron density, temperature, projected temperature, entropy, and pressure profiles of the hot gas of the MPG (left) and SPG (right). The density and temperature profiles are weighted by 0.5-9.9 keV X-ray emissivity; the entropy profiles and density profiles are derived from the temperature and density profiles. For each panel, profiles are plotted every 150 Myr, going from red to blue. The black lines show the initial conditions. The data points over-plotted on the density and temperature profiles correspond to the same observational data that is used to generate the initial conditions shown in Figure 2.1.

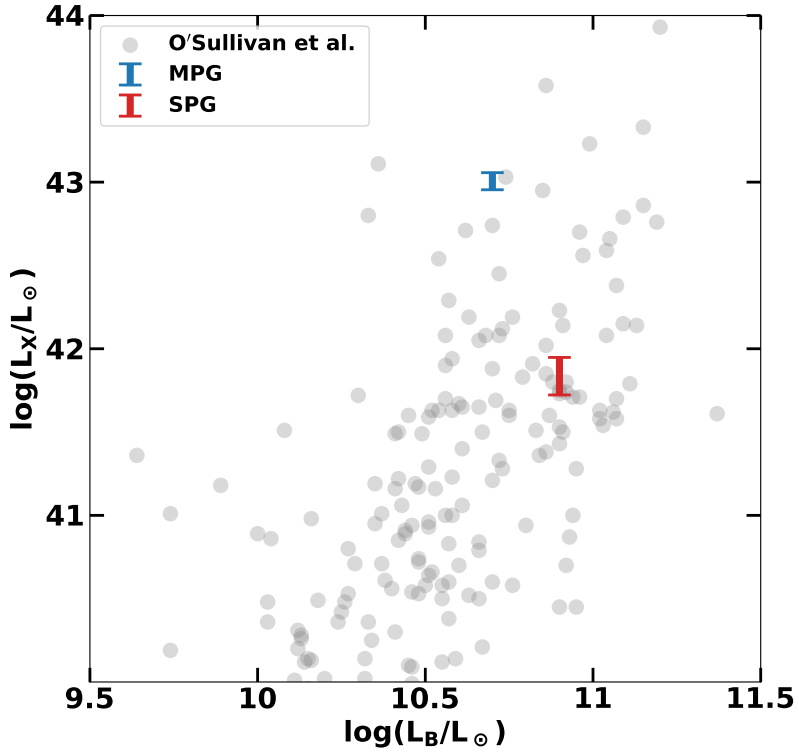

Figure 2.5: The $L_X - L_B$ relation of elliptical galaxies. The filled gray circles are from *O'Sullivan et al.* (2001). The simulated MPG and SPG are shown as the blue and the red symbols, respectively. The error bars represent the range of total X-ray luminosities within 1.5 Gyr.

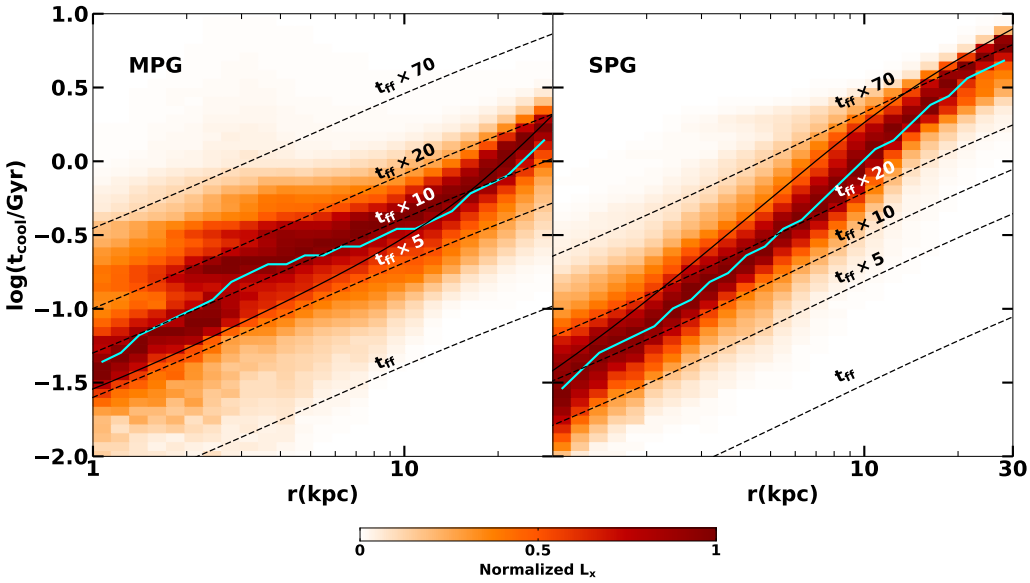

Figure 2.6: The average radial distributions of the cooling time of hot gas over the first 1.5 Gyr simulation of the MPG (left) and the SPG (right). Plots are made by stacking the 2-D distributions of $t_{\rm cool}(r)$ from every simulation output. Color represents the normalized X-ray luminosity within each radial bin. The dashed black dashed lines denote 1, 5, 10, 20 and 70 times of the free-fall time. The solid black line represents the initial $t_{\rm cool}(r)$. The cyan line shows the X-ray luminosity-weighted average $t_{\rm cool}(r)$.

below $5t_{\rm ff}$, and the gas that precipitates in the simulation is the gas at the low end of the $t_{\rm cool}$ distribution, with a $t_{\rm cool}/t_{\rm ff}$ closer to 1. The same point has also been made in *Li and Bryan* (2014b); *Meece et al.* (2015) in the context of precipitation in galaxy clusters. If we look at the mean $\langle \mathbf{t}_{\rm cool}/\mathbf{t}_{\rm ff}\rangle$ instead of the full distribution, our MPG spends about 7% of the time with $min(\langle \mathbf{t}_{\rm cool}/\mathbf{t}_{\rm ff}\rangle) < \mathbf{5}$ within 20 kpc. This is about half of the value found in *Prasad et al.* (2018) for galaxy clusters.

We have analyzed the physical reason for precipitation occurring when the average $\langle \mathbf{t}_{\rm cool}/\mathbf{t}_{\rm ff}\rangle$ is above 1 in galaxy clusters (*Li and Bryan*, 2014b,a; *Voit et al.*, 2017). The physical processes are similar in our simulations of multiphase elliptical galaxies discussed here, and therefore we only emphasize the key points without repeating the same analysis: in systems where AGN feedback is the main source of perturbation, AGN itself is the reason for precipitation (sometimes phrased as "negative feedback"). Both $t_{\rm cool}$ and $t_{\rm ff}$ increase

as a function of radius. Lower entropy gas is uplifted by AGN jets from small radii to larger altitudes where $t_{\rm cool}$ ($\sim$ constant if the uplifting process is adiabatic; see *Li and Bryan* (2014b)) becomes comparable to the local $t_{\rm ff}$. Besides direct uplifting, AGN jets also drive turbulence, which facilitates precipitation by suppressing buoyancy damping (*Voit*, 2018). In addition, turbulence enhances density contrast and broadens the distribution of $t_{\rm cool}$ at any given radius. The high density, low entropy gas is more likely to cool into cold clouds.

Based on the *Hubble* observations of 77 early-type galaxies, *Lauer et al.* (2005) hypothesize that dusty clouds form, settle to the center and disappear repeatedly. This cyclical behavior is recreated in our simulated MPG.

In the SPG, however, even the non-linear perturbation from AGN cannot cause precipitation. The average cooling time of the gas is a steep function of radius (right panel of Figure 2.6). The average $\langle \mathbf{t}_{\rm cool}/\mathbf{t}_{\rm ff} \rangle$ is above 10 throughout the halo, except at the very center, where the gas does condense. Even the low entropy tail sits mostly above $5t_{\rm ff}$. Thus the hot halo of the SPG is too stable for condensation to happen except for the very center.

The stability of hot halo gas is also tightly linked to its entropy defined as $K = kTn_e^{-2/3}$. This is not a surprise as the entropy is almost linearly proportional to cooling time for temperatures we are interested in ($\sim$ 1 keV). The third row of Figure 2.4 shows the time evolution of the gas entropy profiles in our simulated galaxies. *Voit et al.* (2015b) analyze a sample of single and multiphase galaxies and find that the two populations have distinctively different entropy profiles. The single-phase galaxies in their sample follow an outflow solution, with $K(r) = 5r_{\rm kpc}$ keV $\cdot$ cm^2, shown as the gray dashed line. The entropy of multiphase galaxies follows a shallower slope, with $K(r) = 3.5r_{\rm kpc}^{2/3}$ keV $\cdot$ cm^2, corresponding to a precipitation threshold at $t_{\rm cool}/t_{\rm ff} \approx 10$, shown as the pink dashed line. Our simulations show that the single phase galaxy indeed follows the outflow solution of *Voit et al.* (2015b) and that the multiphase galaxy evolves around the precipitation limit. This means that self-regulated AGN feedback is able to maintain the "single-phase" or "multiphase" nature of the gaseous halo, and the main reason is that AGN feedback helps maintain the halo in rough hydrostatic

equilibrium, and does not cause the galaxy to deviate much from the initial condition.

It is worth emphasizing that AGN feedback does not turn a MPG into a SPG. Even though our simulated MPG experiences brief single-phase moments between feedback cycles, its profile is consistent with that of a typical MPG. Real MPGs likely host extended multiphase gas even more frequently than our simulated MPG as we do not consider any minor merger events, which could also trigger precipitation. In addition, winds from AGB stars may not fully mix with the hot ISM before they seed further condensation (*Parriott and Bregman*, 2008).

Whether an elliptical galaxy is single or multiphase ultimately is determined by its formation history and environment. What our simulations imply is that once an elliptical galaxy has formed, it is locked to its state: a SPG will almost always have a single-phase halo, and a MPG will frequently have extended multiphase gas and low-level star formation.

2.5.3 Cooling, Heating, and Sweeping

In this section, we examine the balance between cooling, heating, and sweeping of stellar ejecta. Old stellar population in massive elliptical galaxies keeps losing mass into ambient ISM via stellar winds. To prevent the classical cooling flow and excessive star formation, the stellar wind material has to be removed from the galactic interior. This requires energy in addition to the energy needed to account for radiative cooling loss.

Sources of energy injection include AGN feedback, SNIa and thermalized stellar wind itself. The last two terms are modeled as injection of thermal energy in our simulations as described in Section 2.4. With the parameters we adopted, heating from SNIa is about 5 times the heating from stellar wind. Our AGN feedback injects mostly kinetic energy at the jet base, which then dissipates into heat via shock waves and turbulence with the former being the dominant channel (*Yang and Reynolds*, 2016; *Li et al.*, 2017). The minimum amount of energy needed to sweep stellar ejecta out to radius r is the sum of the change in the potential energy of the stellar ejecta and the enthalpy change.

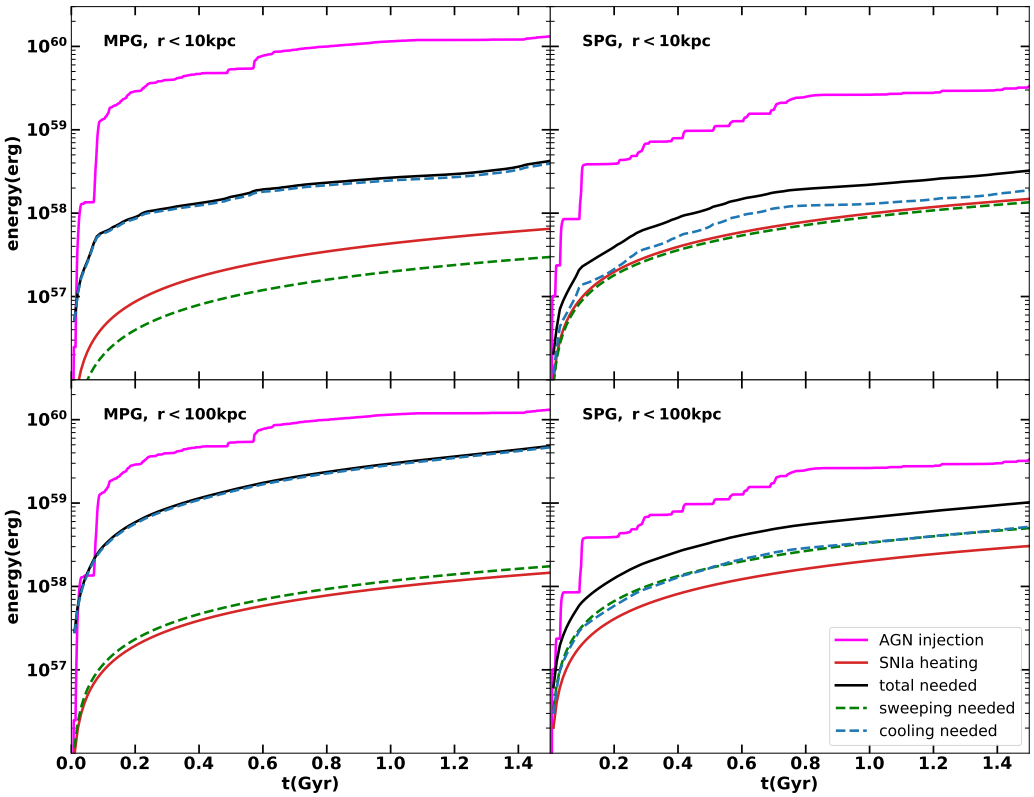

Figure 2.7: The integrated amount of injected energy in the simulations and the energy needed to compensate for radiative cooling and to sweep the stellar ejecta out to maintain a steady state halo within $r < 10$ kpc (upper panels) and $r < 100$ kpc of the simulated MPG (left panels) and SPG (right panels). The sources of energy injection include AGN feedback (magenta lines) and SNIa feedback (red lines). Sources of energy loss including radiative cooling (blue lines) and stellar ejecta sweeping (green lines) are both computed using the initial conditions.

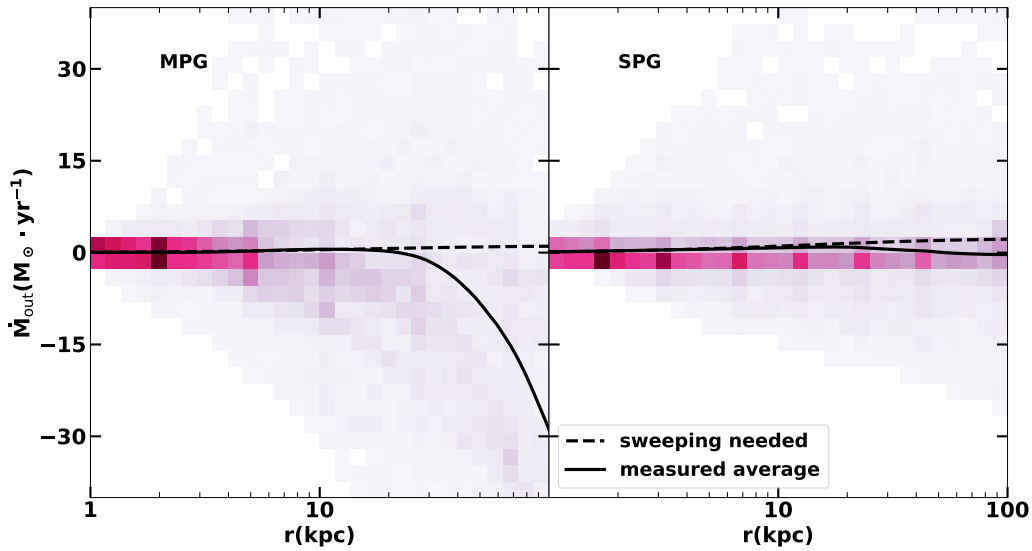

Figure 2.8: The spherically averaged outflow rates measured from our simulated MPG (left panel) and SPG (right panel). Negative values of the outflow rates, $\dot{M}_{\rm out}$ are effectively inflows. Solid lines show the time-averaged outflow rates and dashed lines show the rates needed to sweep out all the gas produced by old stars to maintain a steady state halo.

Figure 2.7 shows how different sources of energy loss and injection compare with each other. In the MPG, within 10 kpc (upper left panel), the total energy needed to balance cooling and sweep out stellar ejecta is about 5 times the energy provided by stellar heating. In the SPG, within 10 kpc stellar heating, cooling and sweeping energy requirements are comparable. This is generally consistent with the estimation in *Voit et al.* (2015b), which leads to their conclusion that SN-driven outflow effectively sweeps stellar ejecta out of the SPG but not the MPG. When we consider the energy injected by AGN, however, we see a more nuanced picture. In both MPG and SPG, the energy injected by AGN is more than an order of magnitude higher than stellar heating. Although this energy is not all deposited in the central 10 kpc, the work done by AGN has to be comparable to stellar heating in the SPG to maintain the balance within 10 kpc. In the MPG, AGN does most of the sweeping. As pointed out in *Voit et al.* (2015b), sweeping in MPG is not effective. Indeed, the total amount of gas that cools ($\sim 5.5 \times 10^8$ $M_\odot$) is not much smaller than the amount added by old stars ($\sim 6.9 \times 10^8$ $M_\odot$). In other words, only a fraction of the stellar ejecta is swept out;

the rest is "recycled" and forms multiphase gas. The fate of the cold gas is discussed in more detail in Section 2.6.3.

If we consider a larger region of the galaxy ($r < 100$ kpc, bottom panels of Figure 2.7) instead of just the central 10 kpc, we find an even larger deficit if stellar feedback is the only source of heating in both MPG and SPG. Due to its higher gas density, the MPG loses more energy via radiative cooling, which causes the AGN to inject more energy to maintain the balance. Because coupling is not perfect, the total energy injected by the AGN is 2-3 times the energy needed within 100 kpc. This is very similar to what is found in our previous simulations of cool-core galaxy clusters (*Li et al.*, 2015). We compare our simulations with cluster simulations in more detail in Section 2.6.3.

Figure 2.8 shows the outflow rate that is needed to maintain a steady state halo (dashed line) along with the actual mass flux measured in the simulation. Although the measured flux varies with time, in both MPG and SPG, the average flux matches the expectation almost perfectly within 10 kpc. This is in line with Figure 2.4 which shows that the properties of the gas in the innermost 10-20 kpc do not deviate much from the initial conditions. However, at $r > 10 - 20$ kpc, the measured outflow rate falls below expectation in both MPG and SPG. As is shown in *Li et al.* (2017), the energy deposition of mechanical AGN jets is a steep function of radius ($\sim r^{-3}$) (see also *Voit and Donahue* (2005); *Fabian et al.* (2005)). As a result, swept-up stellar ejecta pile up around ~ 30 kpc, gradually increasing the density of the gas (Figure 2.4). This then causes the cooling rate to increase, driving an inflow from even larger radii in a process similar to the classical cooling flow. This is why the radial mass flux becomes negative in Figure 2.8. Because the MPG has a higher density halo and a shorter cooling time, this effect is more dramatic. We discuss the result of this pileup problem in Section 2.6.1.

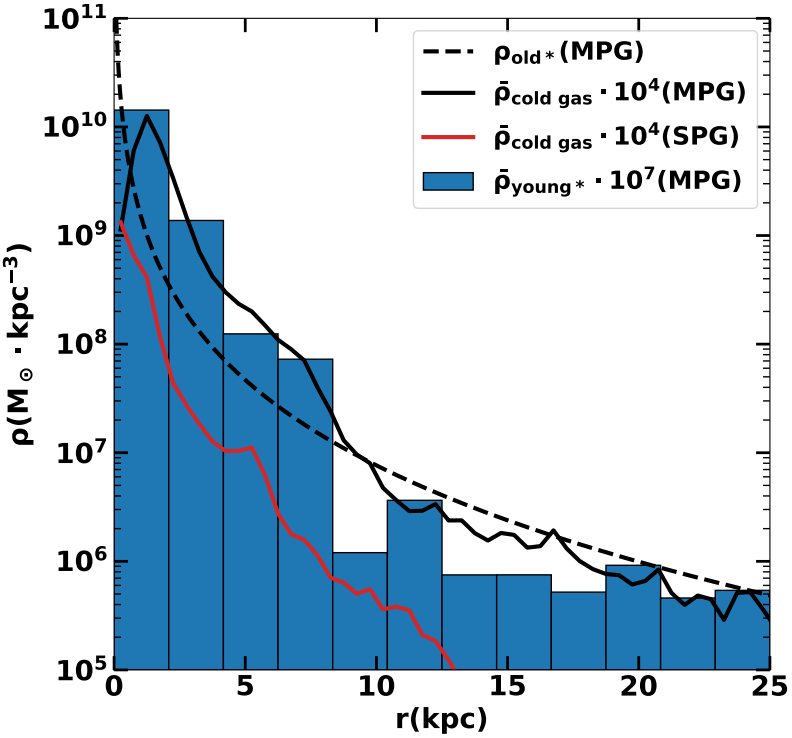

Figure 2.9: The average density distribution of the cold gas (solid black line), old stars (dashed black line), and young stars (blue histogram) of the MPG. The red line shows the average density distribution of the cold gas in the SPG. For presentation purposes, cold gas density and the young stars density are multiplied by 10^7 and 10^4, respectively.

2.5.4 Young Stars in multiphase Elliptical Galaxies

Low-level star formation in elliptical galaxies has been suggested by observations of optical lines and dust lanes (*Lauer et al.*, 2005). Using ultraviolet Hubble Space Telescope Wide Field Camera 3 imaging, *Ford and Bregman* (2013) detected young stars and star clusters in all of the four nearby elliptical galaxies they observed.

As described in Section 2.5.1, stars form in extended multiphase structures in our simulated MPG, with a rate of $\lesssim 0.1\ \mathrm{M}_{\odot} \cdot \mathrm{yr}^{-1}$. We show the radial distribution of cold gas (solid line), old stars (dashed line), and newly formed young stars (histogram) in Figure 2.9. The density distributions of cold gas and young stars are again a "snapshot average" obtained by stacking the distribution from all simulation output data (generated every 10 Myr). Here young stars are defined as star particles with an age younger than 10 Myr. The old stellar population follows the de Vaucouleurs profile by design (§2.4.1).

To make comparison easier, the young star density is multiplied by a factor of 10^7 and the cold gas density is multiplied by a factor of 10^4. The radial distribution of young stars is very similar to the distribution of cold gas. This is not surprising as star formation occurs over a short timescale (the local dynamical time of the cold dense gas). The distribution of young stars is also similar to the old stars, with a slightly steeper slope.

The star formation rate in our simulated galaxy and more remarkably, the radial distribution of the young stars are in excellent agreement with the measurements in *Ford and Bregman* (2013).

For comparison, we also plot in Figure 2.9 the distribution of cold gas in our simulated SPG, which is both much lower in its total amount and much more spatially concentrated than cold gas in the MPG. As mentioned earlier, stars never form in our simulated SPG despite the existence of cold gas. We do caution that our star formation model has been mainly calibrated using simulations of star forming disk galaxies, and thus may not be perfectly suitable for star formation in elliptical galaxies. Nonetheless, even if stars do form in SPGs, they should be very concentrated in the nuclei. Our model predicts very

different spatial distributions of both multiphase gas and stars in single-phase and multiphase galaxies, which can be tested with future observations of a larger sample of ellipticals.

2.5.5 Velocity Dispersion of the Hot Gas

Besides the obvious difference in the morphology of cold gas between the MPG and SPG, there is also significant difference in the AGN duty cycle and power, and thus the level of perturbation it causes in the hot ISM.

As described in Section 2.5.1 and shown in Figure 2.2, in the MPG, AGN feedback has a longer duty cycle, longer "on" time, and overall more energy output than in the SPG (see also Figure 2.7). As a result, the MPG also has a more perturbed hot halo. This is reflected in the profiles of the hot gas shown in Figure 2.4. The gas density, temperature, entropy, and pressure of the MPG generally show larger fluctuations than in the case of the SPG.

Figure 2.10 shows the distribution of average line-of-sight velocity dispersion of the central 10 kpc region of our simulated MPG and SPG. Though the range of σ is similar ($\sim$ 50 – 300 km $\cdot$ s^{-1}) for both galaxies, MPG show a higher fraction time with $\sigma >$ 100 km $\cdot$ s^{-1}. We further define an active phase by selecting times when the AGN is on. Both galaxies show higher sigma during their active times as one would expect, and similar σ distribution when the AGN is off, typically between 50 and 100 km $\cdot$ s^{-1}. Selecting times when cold gas is present within $r < 10$ kpc as the active phase yields similar results. These findings are generally consistent with previous 3D and 2D simulations of similar systems under the influence of momentum-driven AGN feedback (*Gaspari et al.*, 2012a; *Valentini and Brighenti*, 2015).

Ogorzalek et al. (2017) measured turbulent velocities of 13 nearby elliptical galaxies using resonance scattering and line broadening. Their measured range and mean ($\sim$ 110 km$\cdot$ s^{-1}) are in good agreement with our simulations. In particular, they obtained a $\sigma_{1D} = 172^{+108}_{-79}$ km $\cdot$ s^{-1} for NGC 5044 (our MPG); and even though additional data is needed for better measurements of turbulence in NGC 4472 (our SPG), their analysis supports weak

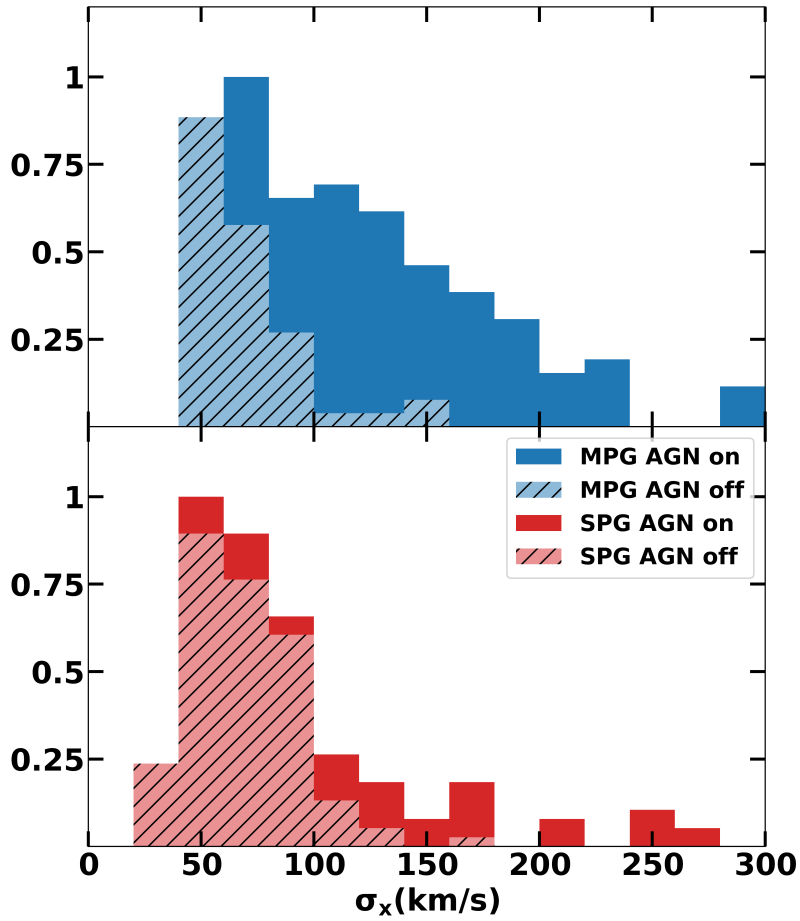

Figure 2.10: Normalized distributions of velocity dispersion (computed as the standard deviation of velocities along $x-$axis) of $r < 10$ kpc region weighted by the 0.5-9.9 keV X-ray emissivity in our simulated MPG (top panel) and SPG (bottom panel). Hatched regions denote the epochs when the AGN is off.

turbulence, in good agreement with our simulation results. With a larger sample of elliptical galaxies, we should be able to test our prediction that velocity dispersion of the hot halo gas is positively correlated with AGN activities and the existence of cold gas.

2.6 Discussion

2.6.1 Long-term Evolution

In this section, we discuss the evolution of the galaxies after the first 1.5 Gyr. As discussed in Section 2.5.3, because AGN-driven galactic wind weakens at larger radii,

stellar ejecta gradually pile up around a few tens of kpc, which then increases the cooling rate. As a result, a major precipitation event happens at $t \sim 1.4$ Gyr in the MPG, with $\sim 2 \times 10^9$ $M_\odot$ of cold gas cooling out of the hot halo. The cold gas falls to the center and forms a massive cold disk. The inner boundary of the disk extends to the accretion region. The disk keeps feeding the central black hole, continuously powering AGN feedback, but the angular momentum prevents it from being quickly accreted. The hot ISM cools directly onto the disk. The central few kpc region gets over-heated and becomes isentropic. Eventually, after about 2 Gyr, star formation and SMBH accretion completely consume the cold disk and the system returns to a state similar to its initial condition. The SPG experiences a similar cycle, at a much later time ($t \sim 4$ Gyr).

One can argue that AGN feedback is still maintaining a thermal balance during the 2 Gyr cold disk phase. However, the existence of an overly massive cold disk and a large isentropic core violate the observations of most elliptical galaxies. For example, *Young et al.* (2011) find that in a large sample (~ 260) of early-type galaxies, only a few of them have massive cold disks. Thus, we consider this phase unphysical and do not include it when discussion our main results in Section 2.5. A persisting massive cold disk is commonly seen in numerical simulations of massive galaxies or clusters (*Li and Bryan*, 2014a; *Prasad et al.*, 2015; *Eisenreich et al.*, 2017). Below we discuss the possible solutions to this problem.

The solutions to the cold disk phase fall in three categories: (i) a major cooling event should never happen, or (ii) the disk should never form in such an event, or (iii) the cold disk is a short-lived phase. It is possible that minor mergers, which are not included in our idealized simulations, can provide heating via dynamical friction in the outskirts of the galaxies at $r \sim 30$ kpc to keep the gas properties constant (*Conroy and Ostriker*, 2008). It is also possible that our AGN feedback is too simplistic, and real AGN jets are able to more effectively remove gas accumulated due to stellar winds to large radii out of the galaxy.

More probably though, elliptical galaxies do periodically host a significant amount of cold gas and go through a very short quasar phase (*Yuan et al.*, 2017). It is possible that

the newly formed cold clouds are more easily destroyed due to thermal conduction or they have additional pressure support from cosmic rays and/or magnetic fields (thus a larger ram-pressure cross-section for given mass) (*Li et al.*, 2018a), and therefore a massive disk never forms. It is also possible that massive cold disks do form (*Alatalo et al.*, 2013) and trigger a quasar as a result of the secular evolution of the galaxies even without a wet merger. Quasar-mode AGN feedback could effectively destroy or remove the cold gas via radiation-driven dusty winds (*Ciotti et al.*, 2017). Cosmic rays from supernovae could also drive galactic winds and remove gas from such disks (*Booth et al.*, 2013; *Salem and Bryan*, 2014; *Pakmor et al.*, 2016; *Ruszkowski et al.*, 2017b; *Butsky and Quinn*, 2018). Cosmic rays injected by the AGN could disperse in the circumgalactic medium and in the process heat the gas via the streaming instability (*Ruszkowski et al.*, 2017a). Alternatively, we simply do not have the resolution to resolve the instabilities of the cold disk for it to be quickly accreted. It is also possible that the longevity of the cold disk has to do with numerical over cooling at the mixing layers between the hot gas and cold gas (*Brighenti et al.*, 2015).

Regardless of the true reason for the existence of the disks, we think that the cold disk should be short-lived if it ever forms in real galaxies as elliptical galaxies are rarely observed to host a cold disk of 10^9 $M_\odot$, and the system should quickly return to the cycles described in Section 2.5. We will test some of the hypothesizes above to solve the disk problem in future work.

2.6.2 Resolution and Model Parameters

2.6.2.1 Lower Resolution Run

To test the convergence of our simulations, we perform lower resolution runs with a maximum refinement level of 10, one level coarser than our standard runs. Everything else is kept the same as in the standard run, including the physical size of the jet launching plane and the accretion zone. We find that the results are qualitatively very similar to our standard runs. In particular, we find similar cyclical behavior (although the exact durations

differ) and $t_{\rm cool}/t_{\rm ff}$ distribution. The main difference is that there are fewer cold clumps and individual clumps are larger, as one would expect.

2.6.2.2 Testing Model Parameters

Since our simulation results are converged, all our tests of the impact of changing model parameters are performed using the lower resolution with a maximum refinement level of 10. We find that our simulation results do not change qualitatively when we change the kinetic fraction of the AGN feedback energy as long as the feedback is not purely thermal. This is consistent with what is found in cluster simulations in *Li and Bryan* (2014a); *Meece et al.* (2017). The results do not depend on the exact value of small angle precession either, again in agreement with *Li and Bryan* (2014a); *Meece et al.* (2017). However we do find that the cold disk forms earlier when there is no precession at all. Note that even though the general results are robust, the details of the galaxy evolution are very sensitive to any small change in simulation parameters or initial conditions. These details include the exact duration of individual cycles, the exact amount of cold gas that cools in each cycle, and the exact morphology of the extended multiphase structures, which can be more bi-polar, isotropic, or more disky. This is because the evolution of the system is highly non-linear. Thus, the results discussed earlier, based on our standard run, should not be seen as the one and only evolutionary path, but rather as a typical one.

The MPG simulation without star formation leads to similar results to the standard run, because star formation is inefficient and has little impact on the evolution of the system. This is quite different from our previous simulations of cool-core clusters and is discussed in more detail in Section 2.6.3.

The one parameter that can alter the results significantly is the feedback efficiency ϵ. When we increase ϵ by a factor of 2 to 1%, we see very little change compared with our standard run, but when we decrease ϵ to 0.1%, the simulated galaxies appear drastically different. A large amount of gas ($\sim 10^8$ $M_\odot$) cools into spatially extended structures and

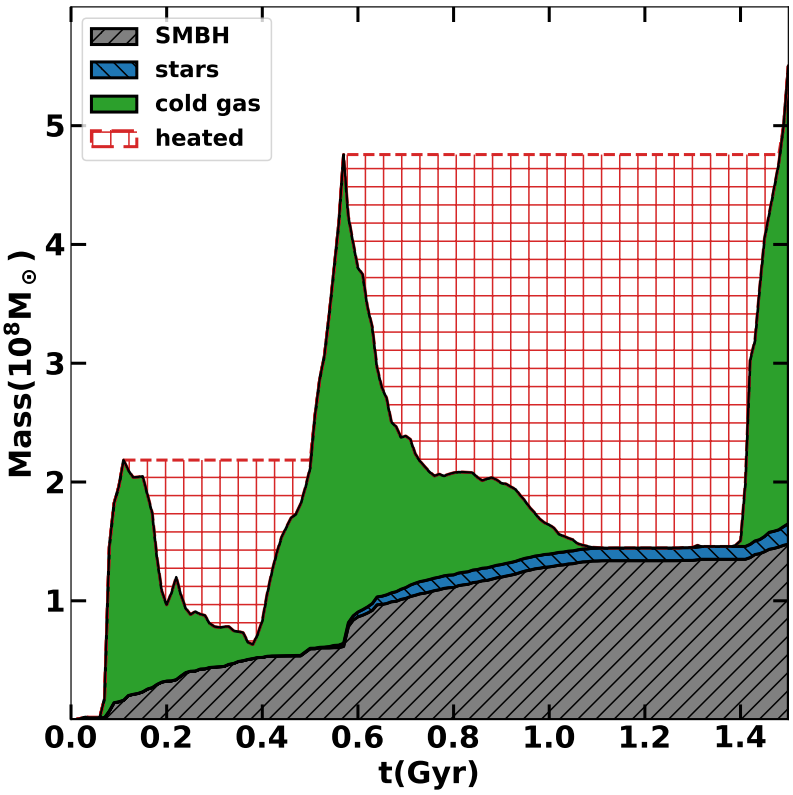

Figure 2.11: The integrated amount of cold gas ($T < 10^5$ K) that is processed by the SMBH (grey), the gas that has turned into young stars (blue), the cold gas that exists in the halo of the simulated MPG (green), and the lower limit of the cold gas that is returned to the hot phase via shredding and mixing (red).

forms stars even in the SPG. This is not surprising as the total energy injected by the SMBH in our standard run is only 2-3 times the required energy to balance radiative cooling and sweep stellar ejecta out of the halo (Figure 2.7). A lower ϵ results in over-cooling of the halo, and causes the galaxies to evolve significantly away from their initial conditions and thus violate the observations. This finding is in tension with *Gaspari et al.* (2012a), which we discuss in detail in Section 2.6.4.

2.6.3 Comparison with Cluster Simulations

The evolution of our simulated elliptical galaxies, especially the MPG, shares many similarities with simulated cool-core galaxy clusters in our previous works (*Li and Bryan*, 2014a,b; *Li et al.*, 2015). Both MPG and cool-core clusters experience cycles of AGN

outbursts, formation of extended multiphase gas and star formation. The criterion for thermal instability to develop in both systems is $t_{\rm cool}/t_{\rm ff} \sim 10$, and the feedback efficiency required for AGN to balance cooling is also similar ($\epsilon \sim 0.5 - 1\%$). The amount of gas that precipitates and the number of stars that form are lower in MPG than in clusters. As a result, individual cycles are also shorter in MPG than in clusters. This is simply because the density of the hot gas in the MPG is much lower than in the center of a cool-core clusters. Thus, the amount of low entropy hot gas that can cool in each cycle is smaller.

The most striking difference between the MPG and the cluster simulations is the fate of the cold gas. Figure 2.11 shows the total amount of cold gas ($T < 10^5$ K) processed by the SMBH, the amount that formed stars, and the gas that exists in the system integrated over time. The amount of gas turning into stars is only $\sim 1/10$ of that falling onto the SMBH. This is quite the opposite of what is seen in our simulated cool-core cluster, where the amount of star formation is an order of magnitude larger than SMBH accretion.

We speculate that this is because the cold clumps in our simulated MPG are "fluffier" (with lower average density and pressure) than in clusters, and thus are less effective at turning into stars. They are likely also more susceptible to ram pressure stripping and shredding. It is difficult to quantify the amount of cold gas that is mixed back into the hot phase in a grid-based code. However, we can obtain a lower limit on the amount of heated gas based on the simple fact that the total amount of cold gas formed in the galaxy has to increase monotonically. As Figure 2.11 shows, a significant amount of cold gas is returned to the hot phase before it forms stars or falls onto the SMBH, often more than the amount of traceable cold gas.

Our simulations suggest that star formation efficiency is lower in MPGs than in cool-core clusters which has similar efficiency as the main sequence galaxies (*Li et al.*, 2015). The average gas depletion time in our simulated MPG is about 7 Gyr. However, we caution that neither the cold clumps nor star formation is well resolved in our simulations. Our conclusion needs to be confirmed with dedicated future high-resolution studies.

2.6.4 Comparison with Other Works

In this section, we compare our simulation results with two other works: *Gaspari et al.* (2012a) and *Eisenreich et al.* (2017) that study AGN feedback in idealized elliptical galaxies using 3D hydro simulations.

The setup of our MPG is very similar to *Gaspari et al.* (2012a) who use the FLASH code. We both find that cold-mode accretion powered mechanical AGN feedback can successfully suppress cooling in elliptical galaxies. The spatial extent of the cold gas and the level of turbulence in the hot halo in our MPG are generally in good agreement with *Gaspari et al.* (2012a). A remarkable difference is that *Gaspari et al.* (2012a) favor a much lower SMBH feedback efficiency $\sim 10^{-4} - 10^{-3}$. We attribute this difference mainly to the difference in the treatment of cold gas in the two simulations. *Gaspari et al.* (2012a) remove cold gas using a dropout term and assumes that all the gas that cools falls onto the SMBH. We follow the evolution of cold clumps in our simulations and find that only a fraction ($< 1/5$) of cold gas actually gets processed by the AGN, and a larger fraction is mixed back into the hot phase before it is accreted or forms stars (see Figure 2.11 and Section 2.6.3).

Eisenreich et al. (2017) uses smoothed particle hydrodynamics code to study the quenching effect of AGN feedback in massive elliptical galaxies. Despite the differences in the simulation codes, initial setup, and modes of AGN feedback (*Eisenreich et al.* (2017) includes radiative feedback in addition to mechanical feedback), we find generally consistent results. In particular, both works find that AGN feedback has only a small effect on the L_X of the galaxy, and thus causes little change to L_X position on scaling relations (e.g., the $L_X - L_B$ relation in Figure 2.5). *Eisenreich et al.* (2017) also find that AGN feedback is most effective in pushing gas out of the central $\sim$ 30 kpc, and a persisting cold disk forms in all of their simulations. This suggests that the formation of the disk at later times in our simulations (Section 2.6.1) does not depend on the code or the specific implementation of the feedback model (at least in these simulations).

2.7 Conclusions

We have performed 3D AMR hydrodynamical simulations of two idealized elliptical galaxies based on the observations of NGC 5044 and NGC 4472. We choose the former as a representative multiphase elliptical galaxy (MPG, defined as a galaxy hosting spatially extended multiphase gas) and the latter a representative single-phase galaxy (SPG, defined as a galaxy that has no cooler component or the cooler gas is only detected in the nucleus). We model momentum-driven AGN feedback powered by cold-mode accretion, and study the interplay between radiative cooling, AGN feedback and feedback from old stars in the galaxies. We focus on the development of thermal instabilities in the two galaxies and the formation of multiphase gas. We compare our simulation results with previous analytical prediction and observations of nearby elliptical galaxies including the velocity dispersion of the hot gas and the distribution of young stars. Our main results are summarized below:

1. The simulated MPG has an average $t_{\rm cool}/t_{\rm ff} \sim 10$ within ~ 30 kpc, and momentum-driven AGN jets frequently trigger thermal instabilities in the halo, causing hot gas to cool into extended multiphase structures. The galaxy experiences precipitation-regulated AGN feedback cycles with typical periods of a few hundred Myr. In the simulated SPG, $t_{\rm cool}/t_{\rm ff}$ is a steeper function of radius, and is always above 10 except in the very center where cooling can happen. The galaxy rarely shows extended multiphase gas, and AGN feedback cycles are typically only a few tens of Myr.

2. Most of the stellar ejecta in the inner halo of the SPG are swept out, while some of them cool in the MPG, As predicted in *Voit et al.* (2015b). Most of the sweeping work is done by AGN feedback rather than stellar feedback in both MPG and SPG. Because shock heating is a steep function of radius, AGN-driven outflow does not result in a steady state halo. Instead, it slows down around 30 kpc, causing gas to pile up. As a result, after a few Gyr, a large a mount of gas precipitates and forms a massive cold disk.

3. AGN feedback is on more frequently with a higher average power in the MPG than in the SPG. As a result, the hot halo gas in the MPG shows a high velocity dispersion (> 100 km $\cdot$ s^{-1}) more frequently than the SPG. Both galaxies have similar velocity dispersions ($\sim 50 - 100$ km $\cdot$ s^{-1}) during the quiescent phase when the AGN is off.

4. The spatially extended multiphase gas in the simulated MPG is often associated with extended star formation. The star formation rate is low (< 0.1 M$_\odot \cdot$ yr^{-1}). The spatial distribution of the young stars is similar to the cold stellar population, but slightly steeper as a function of radius. This is in excellent agreement with the Hubble observations of young stars in several nearby elliptical galaxies. Star formation does not occur in our simulated SPG until $t \sim 4Gyr$. We caution that the long-term evolution of our simulated galaxies may be unrealistic due to lack of dynamical heating from infalling satellites and other physical processes not included in the simulations.

5. Compared to our previous simulations of cool-core galaxy clusters, we find that in elliptical galaxies, the thermal instability criterion ($t_{\rm cool}/t_{\rm ff} \sim 10$) and the required AGN feedback efficiency ($\epsilon \sim 0.5 - 1\%$) are very similar. The main difference between the simulated elliptical galaxies and cool-core clusters is the fate of the cold gas. In elliptical galaxies, cold gas has a lower average density and thus forms stars less efficiently. In addition, in multiphase elliptical galaxies, a larger fraction of cold gas is shredded and returned to the hot phase before it can be accreted onto the SMBH.

Our simulations suggest that maintenance-mode AGN feedback not only maintains the general quiescent state of massive elliptical galaxies, but also maintains the multi- or single-phase nature of the galaxy. In other words, once an elliptical galaxy is formed with a halo structure that allows local thermal instability to develop (with a flatter entropy or $t_{\rm cool}/t_{\rm ff}$ profile), it will frequently exhibit extended multiphase gas, whereas a galaxy with a steeper entropy or $t_{\rm cool}/t_{\rm ff}$ slop will only periodically have cold gas in its very center. Future

simulations with more physical processes included (e.g., cosmic rays) will help to better understand the long-term evolution of the galaxies.

CHAPTER III

Chaotic Cold Accretion in Giant Elliptical Galaxies Heated by AGN Cosmic Rays

3.1 Preface

The results presented in this chapter were published in: *Wang, Chaoran, Mateusz Ruszkowski, and H.-Y. Karen Yang. "Chaotic cold accretion in giant elliptical galaxies heated by AGN cosmic rays." Monthly Notices of the Royal Astronomical Society 493.3 (2020): 4065-4076* and are reproduced here with minor style revisions.

3.2 Abstract

Black hole feedback plays a central role in shaping the circumgalactic medium (CGM) of elliptical galaxies. We systematically study the impact of plasma physics on the evolution of ellipticals by performing three-dimensional non-ideal magneto-hydrodynamic simulations of the interactions of active galactic nucleus (AGN) jets with the CGM including magnetic fields, and cosmic rays (CRs) and their transport processes. We find that the physics of feedback operating on large galactic scales depends very sensitively on plasma physics operating on small scales. Specifically, we demonstrate that: (i) in the purely hydrodynamical case, the AGN jets initially maintain the atmospheres in global thermal balance. However, local thermal instability generically leads to the formation of massive cold disks in the vicinity of

the central black hole in disagreement with observations; (ii) including weak magnetic fields prevents the formation of the disks because local B-field amplification in the precipitating cold gas leads to strong magnetic braking, which quickly extracts angular momentum from the accreting clouds. The magnetic fields transform the cold clouds into narrow filaments that do not fall ballistically; (iii) when plasma composition in the AGN jets is dominated by CRs, and CR transport is neglected, the atmospheres exhibit cooling catastrophes due to inefficient heat transfer from the AGN to CGM despite Coulomb/hadronic CR losses being present; (iv) including CR streaming and heating restores agreement with the observations, i.e., cooling catastrophes are prevented and massive cold central disks do not form. The AGN power is reduced as its energy is utilized efficiently.

3.3 Introduction

In the centers of galaxy clusters, groups, and giant elliptical galaxies, radiative cooling time of the hot gaseous halos can be much shorter than the Hubble time. When this is the case, and in the absence of heating sources, a classic cooling flow will form (*Fabian*, 1994) leading to high star formation rates (SFRs). However, the observed SFRs are at least one order of magnitude lower than that predicted by the pure cooling flow (e.g., *O'Dea et al.*, 2008). It has been widely accepted that the feedback from active galactic nuclei (AGN) is the most plausible solution to the cooling flow problem. The energetic AGN feedback is able to maintain the overall thermal equilibrium of hot gaseous halos and prevents excessive gas cooling and star formation in galaxy clusters, groups, and giant elliptical galaxies (see *McNamara and Nulsen*, 2007, for a review). Most AGN found in the centers of these massive systems at low redshift are associated with bipolar jet outflows launched by the central supermassive black holes (SMBHs). The AGN jet inflates radio-emitting bubbles that generate X-ray cavities in the hot halo. How exactly the jets and bubbles transfer energy to the hot halo remains unclear. Various possibilities have been proposed and extensively studied in the literature, including: mixing of jet-inflated bubble filled with ultra-hot gas

(e.g., *Brüggen and Kaiser*, 2002; *Gilkis and Soker*, 2012; *Hillel and Soker*, 2014, 2016, 2017; *Yang and Reynolds*, 2016); dissipation of jet-induced sound waves and weak shocks (e.g., *Fabian et al.*, 2003; *Ruszkowski et al.*, 2004a,b; *Fabian et al.*, 2005, 2006, 2017; *Sanders and Fabian*, 2008; *Zweibel et al.*, 2018; *Fabian et al.*, 2003, 2005, 2017; *Forman et al.*, 2007; *Randall et al.*, 2015; *Barai et al.*, 2016; *Yang and Reynolds*, 2016; *Li et al.*, 2017; *Martizzi et al.*, 2019), and turbulent dissipation of gas motions (e.g., *De Young*, 2010; *Zhuravleva et al.*, 2014); and heating by cosmic rays (CRs) escaping from the jet-inflatd bubbles (e.g., *Guo and Oh*, 2008; *Enßlin et al.*, 2011; *Ruszkowski et al.*, 2008; *Wiener et al.*, 2013b; *Fujita and Ohira*, 2013; *Fujita et al.*, 2013; *Jacob and Pfrommer*, 2017a,b; *Ruszkowski et al.*, 2017a; *Ehlert et al.*, 2018). However, no consensus has been reached and the dominant mechanism(s) is(are) uncertain.

Despite adopting various numerical methods, simulations of AGN feedback and cooling flow problem often reveal formation of a massive ($\sim 10^9$ to 10^{10} solar masses in ellipticals and 10^{12} solar masses in clusters) long-lived cold disk in the vicinity of the central SMBH (e.g., *Li and Bryan*, 2014a; *Eisenreich et al.*, 2017; *Qiu et al.*, 2019b; *Wang et al.*, 2019). However, most of the observed disks are much less massive than those found in the simulations. In the sample of 260 elliptical galaxies in *Young et al.* (2011), only three galaxies have molecular mass exceeding 10^9 solar masses, and only one of these three (NGC 2764) has the velocity distribution consistent with a rotating disk. Similarly, observations of clusters reveal that molecular gas is rarely rotationally supported and molecular gas mass in the rotationally supported phase (10^8 to 10^9 solar masses) is much smaller than seen in simulations (*Hamer et al.*, 2014; *Russell et al.*, 2019). The formation of such massive disks poses further problems for the feeding of the central SMBH and AGN feedback. In our previous work (*Wang et al.*, 2019), the fueling of large amounts of cold gas from the disk breaks the self-regularity of the AGN feedback, thus causing the central region of the halo to overheat. This results in an isentropic core, which is inconsistent with the observations.

Radio observations show that the jet-inflated bubbles emit synchrotron radiation, indi-

cating the presence of relativistic electrons. However, it has been shown that the emitting electrons plus magnetic field have less pressure than required to maintain pressure balance between the bubble interior and the ambient hot halo gas (*Dunn and Fabian*, 2004). Therefore, the non-radiating component has to be present inside the bubbles to provide the required pressure, e.g., ultra-hot gas, magnetic fields, and CR protons. However, the relative contribution of each of these non-thermal components is not well constrained by the observations.

CR-dominated AGN jet can potentially solve the disk problem mentioned above. CRs heat the halo gas via Coulomb, hadronic interactions (*Yoast-Hull et al.*, 2013), and streaming instability (*Zweibel*, 2013, for a review) as they are transported out from the jet-inflated bubbles. Streaming instability allows CRs to scatter on the self-excited Alfvén waves and to stream down their pressure gradient along the magnetic field at or above the Alfvén speed. CR streaming down the pressure gradient along the B-field results in CRs doing work on the gas and effectively heating it. This additional mode of heating could help to heat the has at larger distances from the center and eliminate catastrophic cooling and cold disk formation at late times. However, recent simulations of a single short-duration jet in the galaxy cluster (*Yang et al.*, 2019) demonstrate that CR-dominated jets can efficiently uplift the hot halo due to high buoyancy of the CR fluid filling the bubbles and larger cross-sections of the raising bubbles. This could remove gas with the shortest cooling time near the cluster center and potentially limit the formation of the disk in the long term. Interestingly, while more efficient heating in long term is expected, *Yang et al.* (2019) show that the CR-dominated jet makes the intracluster medium (ICM) more prone to the development of thermal instabilities in the center due to inefficient mixing and heating on short time-scales.

Motivated by the above findings, in this paper we investigate how CR feedback affects the long-term evolution of the hot halo. Using magneto-hydrodynamic (MHD) simulations, we show that when CR transport and heating due to the streaming instability are included, CR-dominated jet can maintain global thermal equilibrium of the hot halo in elliptical

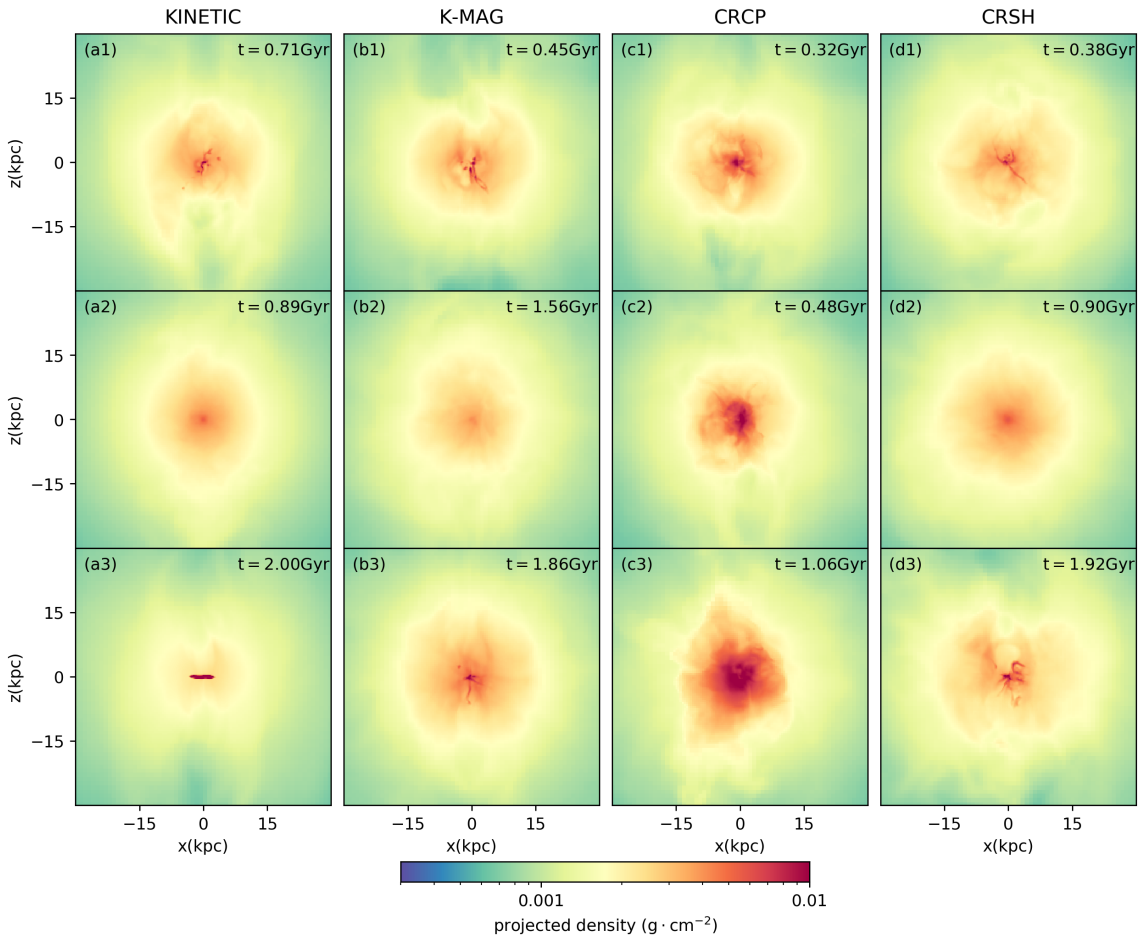

Figure 3.1: Columns from left to right: projected gas density of KINETIC, K-MAG, CRCP, and CRSH runs. Within each column the slices are plotted in chronological order from top to bottom. The density is projected along the $y-$axis within the central 60 kpc-wide cube. The jet is along the $z-$axis.

galaxies and, at the same time, prevent the formation of the massive cold disks.

3.4 Methodology

We perform three-dimensional MHD simulations using the FLASH code (*Fryxell et al.*, 2000; *Dubey et al.*, 2008) with the directional unsplit staggered mesh MHD solver (*Lee and Deane*, 2009; *Lee*, 2013). The simulation domain is a statically-refined cubic box with width of $L_{\rm box}$ = 250 kpc. The domain is refined by a set of nested cubic regions with

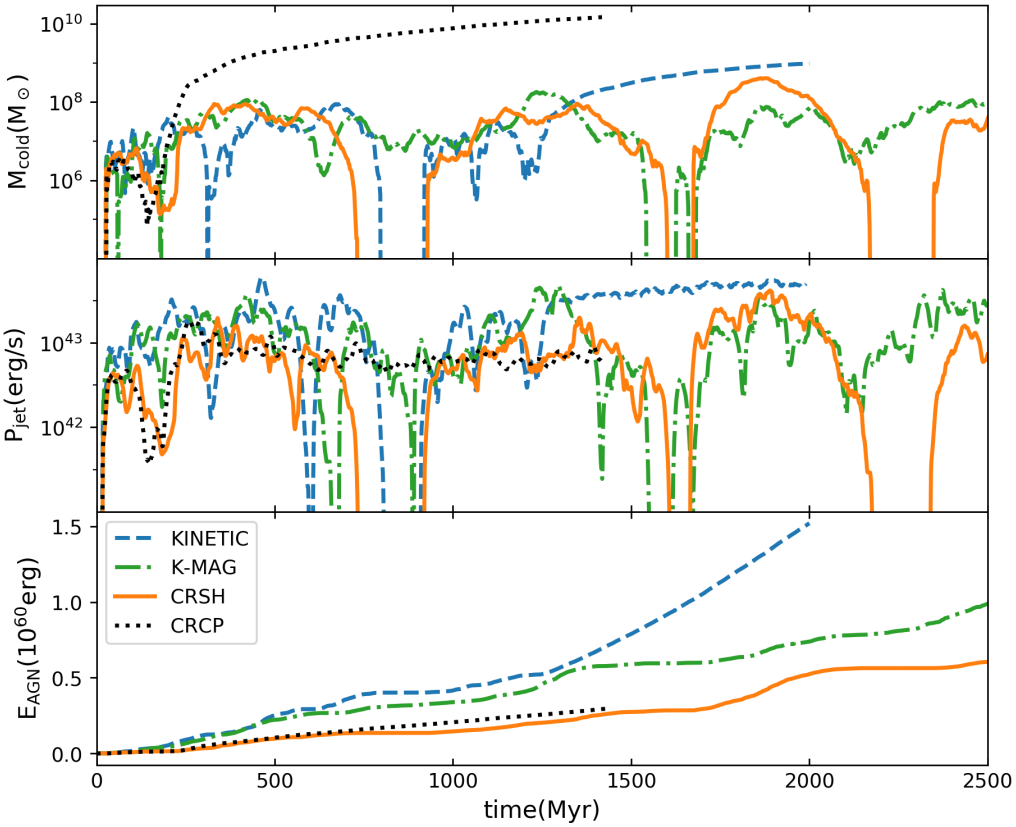

Figure 3.2: Time evolution of cold gas mass (top), AGN jet power (middle) and cumulative AGN energy (bottom) of KINETIC (blue dashed lines), K-MAG (green dash-dotted lines), CRCP run (black dotted lines), and CRSH (orange solid lines). The jet powers are averaged using a 20 Myr-wide moving window.

increasing refinement levels. The entire region is refined by $(64)^3$ root grids and the central $L_{\rm box}/2^n$ wide regions have n additional nested levels of refinement ($n = 1, ..., 4$) with the refinement level increasing with the decreasing distance from the domain center. Therefore, the smallest cell is $\Delta x_{\rm min} = L_{\rm box}/64/2^4 \approx 0.244$ kpc wide and the highest refinement region is $L_{\rm box}/2^4 \approx 16$ kpc wide. We adopt the diode boundary conditions. That is, the gas can only flow out and all variables have zero gradient at the computational box boundary.

name	magnetic field	$f_{\rm cr}$	CR streaming
KINETIC	no	0	no
K-MAG	yes	0	no
CRCP	yes	0.8	no
CRSH	yes	0.8	yes

Table 3.1: List of Simulations

We follow our previous work (*Wang et al.*, 2019) in setting up the initial conditions. The density and temperature profiles of the hot gas are initially in hydrostatic equilibrium. The gravitational potential includes contributions from stars, dark matter, and the central SMBH. Our initial conditions agree with NGC 5044, which is observed to have extended multiphase gas in the center (*Werner et al.* 2014; as explained below, our simulations develop cold phase component over time due to local thermal instability). Following *Ruszkowski et al.* (2007), we include tangled magnetic fields with the following power spectrum:

$$B_k \propto k^{-11/6} \exp\left[-\left(\frac{k}{k_0}\right)^4\right], \tag{3.1}$$

where $k_0 = 10^2(2\pi/L_{\rm box})$. In order to generate magnetic fields characterized by the above spectrum, we first calculate real-space magnetic fields by inversely Fourier transforming the above power spectrum. We then renormalize the average field strength such that the plasma $\beta \sim 100$. We then Fourier transform the B-fields, clean B-field divergence in Fourier space and then perform inverse Fourier transform to obtain real-space B-fields. We repeat this procedure until the magnetic fields become divergence-free.

The key physical processes that we consider are radiative cooling, feedback from old

stars, CR transport and heating, and AGN feedback. For radiative cooling, we use the tabulated cooling functions from *Sutherland and Dopita* (1993) assuming one solar metallicity (*Buote et al.*, 2003b; *Komiyama et al.*, 2009). For old star feedback, we use the model described in *Wang et al.* (2019). In short, we consider the mass loss from evolved stars and thermal energy injection from type Ia supernovae. The ejecta from the evolved stars are assumed to be thermalized by the random stellar motions and the energy and mass are injected at a constant rate.

In the following sections, we describe the included CR physics (section 3.4.1) and the AGN feedback model (section 3.4.2).

3.4.1 CR physics

CRs are energetic particles travelling at nearly the speed of light. However, they are confined due to the scattering on the magnetic fields that are coupled to the hot plasma via flux freezing. In the CR self-confinement picture, CRs generate magnetic field fluctuations via the streaming instability and scatter on them, which limits their effective transport speed with respect to the gas to Alfvén speed. In this scenario, CRs advect with the gas, stream with respect to the gas, and heat the gas at the rate that depends on the Alfvén speed and the CR pressure gradient. This is the working assumption for the CR MHD equations quoted below. Alternatively, in the extrinsic confinement model (*Zweibel*, 2017), CRs are confined to the gas by scattering on pre-existing fluctuations in the turbulent gas, and CR transport can be described as diffusion. In one of our models (the CRCP run in Table 3.1) we consider this extrinsic confinement model under the simplifying assumption that the diffusion coefficient is very small, in which case CRs can be treated as a relativistic fluid advecting with the gas. This case is only included as a reference case to help us isolate the impact of streaming transport and streaming heating. The CRs are modelled as a relativistic fluid with adiabatic index $\gamma_{\rm cr} = 4/3$. We follow the evolution of the CR pressure $p_{\rm cr}$ (or energy density $e_{\rm cr} = p_{\rm cr}/(\gamma_{\rm cr} - 1)$) as a function of space and time. The CR implementation

includes the following processes: (i) advection with the gas, (ii) transport of CRs along the magnetic field lines due to Alfvénic streaming (CR streaming/drift speed is determined by the streaming instability) and the associated energy transfer from CRs to the gas, and (iii) heating of gas by the CRs via Coulomb and hadronic interactions. We solve the MHD equations in the following form:

$$\frac{\partial \rho}{\partial t} + \nabla \cdot (\rho \mathbf{u_g}) = \dot{\rho}_{\rm jet} \tag{3.2}$$

$$\frac{\partial (\rho \mathbf{u_g})}{\partial t} + \nabla \cdot \left(\rho \mathbf{u_g} \mathbf{u_g} - \frac{\mathbf{B}\mathbf{B}}{4\pi} \right) + \nabla p_{\rm tot} = \rho \mathbf{g} + \dot{\mathbf{p}}_{\mathbf{jet}} \tag{3.3}$$

$$\frac{\partial e_{\rm tot}}{\partial t} + \nabla \cdot \left[(e_{\rm tot} + p_{\rm tot}) \mathbf{u_g} - \frac{(\mathbf{B} \cdot \mathbf{u_g})\mathbf{B}}{4\pi} + \mathbf{F}_{\rm stream} \right] = \rho \mathbf{u_g} \cdot \mathbf{g} + \dot{e}_{\rm jet} - C_{\rm rad} - C_{\rm cr,net} \tag{3.4}$$

$$\frac{\partial e_{\rm cr}}{\partial t} + \nabla \cdot (e_{\rm cr} \mathbf{u_g} + \mathbf{F}_{\rm stream}) = -p_{\rm cr} \nabla \cdot \mathbf{u_g} + f_{\rm cr} \dot{e}_{\rm jet} - C_{\rm cr,C} - C_{\rm cr,h} - C_{\rm cr,s}, \tag{3.5}$$

where ρ is the gas density; $\mathbf{u_g}$ is the gas velocity; $\mathbf{B}$ is the magnetic field; and $\mathbf{g}$ is the gravitational acceleration. The total pressure, $p_{\rm tot}$ is the sum of the gas thermal pressure, magnetic pressure and the CR pressure, $p_{\rm tot} = p + B^2/8\pi + p_{\rm cr}$; and the total energy density $e_{\rm tot}$ is the sum of the gas internal energy, kinetic energy, magnetic energy, and the CR energy $e_{\rm tot} = p/(\gamma_{\rm gas} - 1) + \rho u_g^2/2 + B^2/8\pi + e_{\rm cr}$, where $\gamma_{\rm gas} = 5/3$ is the adiabatic index of the ideal gas. $\dot{\rho}_{\rm jet}$, $\dot{p}_{\rm jet}$, and $\dot{e}_{\rm jet}$ represent the mass, momentum, and energy injection of the AGN jets. We explain in detail about the AGN feedback in section 3.4.2.

The three terms on the right hand side of Eq.3.5, $C_{\rm cr,C}$, $C_{\rm cr,h}$, and $C_{\rm cr,s}$, account for the CR fluid energy losses due to Coulomb, hadronic interactions, and streaming heating, respectively. $C_{\rm cr,C}$ and $C_{\rm cr,h}$ are given by (*Yoast-Hull et al.*, 2013):

$$C_{\rm cr,C} = 4.93 \times 10^{-19} \left(\frac{n_{\rm cr}}{\rm cm^{-3}} \right) \left(\frac{n_{\rm e}}{\rm cm^{-3}} \right) {\rm erg \cdot cm^{-3} s^{-1}}; \tag{3.6}$$

$$C_{\rm cr,h} = 8.56 \times 10^{-19} \left(\frac{\gamma}{3}\right)^{1.28} \left(\frac{n_{\rm cr}}{\rm cm^{-3}}\right) \left(\frac{n_{\rm p}}{\rm cm^{-3}}\right) \rm erg \cdot cm^{-3} s^{-1}, \tag{3.7}$$

where $\gamma = 3$ is the average Lorentz factor of CRs, $n_{\rm p} = \rho/(\mu_{\rm p} m_{\rm p})$ is the gas proton number density, and $n_{\rm e} = \rho/(\mu_{\rm e} m_{\rm p})$ is the gas electron number density. $n_{\rm cr}$ is the CR number density which is:

$$n_{\rm cr} = \frac{n-4}{n-3} \frac{e_{\rm cr}}{E_{\rm min}}, \tag{3.8}$$

where $E_{\rm min} = 1$GeV is the low energy cut-off of CR energy, and $n = 4.5$ is the slope of CR momentum distribution. In the self-confined picture, CRs stream with respect to the gas and get scattered on self-excited MHD waves. This leads to the transfer of CR energy to the gas. The heating rate is (*Wiener et al.*, 2013a):

$$C_{\rm cr,s} = |\mathbf{u}'_{\mathbf{A}} \cdot \nabla p_{\rm cr}|, \tag{3.9}$$

where $\mathbf{u}'_{\mathbf{A}}$ is the modified Alfvén velocity. We assume:

$$\mathbf{u}'_{\mathbf{A}} = \begin{cases} \min(\mathbf{u}_{\mathbf{A}}, 200 \text{ km/s}), & r > 1 \text{ kpc} \\ 0, & r \leqslant 1 \text{ kpc} \end{cases} \tag{3.10}$$

The size of the central region where the streaming heating is suppressed is comparable to the size of the base of the AGN jet. We treat the central 1 kpc region as a subgrid region and switch off streaming heating there to avoid artificial heating. In this approximation the streaming velocity cannot exceed than 200 km/s, which helps to save computational cost. We verified that this constraint limits the heating in only in a very small fraction of cells and does not affect the conclusions presented below.

The terms on the right hand side of Eq.3.4, $C_{\rm rad}$ and $C_{\rm cr,net}$, represent the radiative cooling losses of the gas and the net total energy loss of the composite gas plus CR fluid, respectively. As during hadronic collisions 5/6 of the CR energy escapes from the gas due

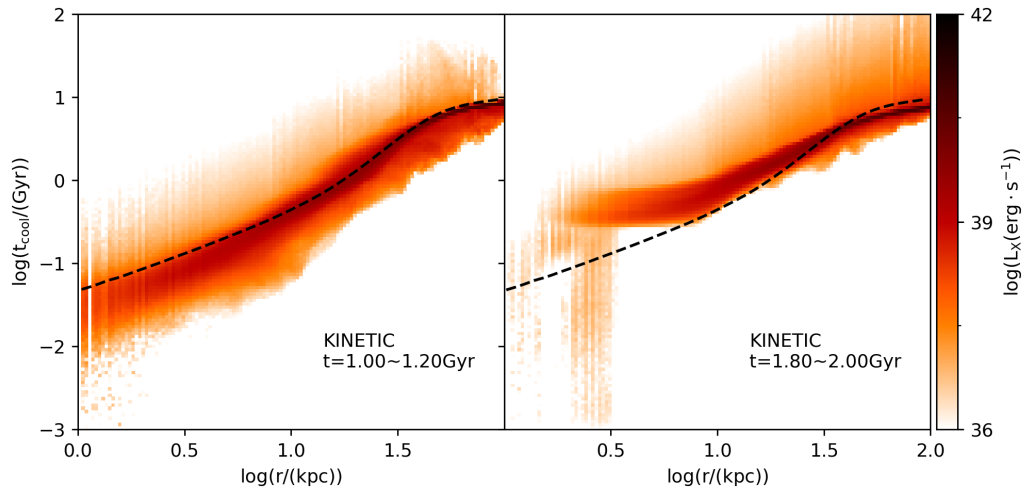

Figure 3.3: The radial distributions of gas cooling time in KINETIC run averaged over two periods of time. Left: $t = 1 \sim 1.2$ Gyr; right $t = 1.8 \sim 2.0$ Gyr. For each panel, the average is calculated by stacking the cooling time distributions of all simulation outputs within the corresponding period. Color shows the gas X-ray luminosity. The dashed lines represent the initial cooling time profile.

to gamma-ray and neutrino emission, the net loss of the energy is

$$C_{\rm cr,net} = \frac{5}{6} C_{\rm cr,h}, \tag{3.11}$$

i.e., 1/6 of the CR hadronic loss rate is used to heat the thermal gas, and the remaining 5/6 are permanently lost from the system.

The CR streaming flux $\mathbf{F}_{\rm stream}$ in Eq.3.4 and Eq.3.5 is $\mathbf{F}_{\rm stream} = -(e_{\rm cr}+p_{\rm cr})\mathbf{u}'_{\mathbf{A}}\ {\rm sgn}\ (\mathbf{B}\cdot\nabla e_{\rm cr})$. To avoid infinitely fast variations of $\nabla\cdot\mathbf{F}_{\rm stream}$ at the local extrema of $\nabla e_{\rm cr}$, we follow the method of *Sharma et al.* (2009) and regularize the streaming flux as:

$$\mathbf{F}_{\rm stream} = -(e_{\rm cr}+p_{\rm cr})\mathbf{u}'_{\mathbf{A}}\ \tanh\left(h_c \frac{\mathbf{B}}{|\mathbf{B}|}\cdot\frac{\nabla e_{\rm cr}}{e_{\rm cr}}\right). \tag{3.12}$$

We set the regularization scale height h_c to 10 kpc for all runs reported in Section 3.5. We performed a test run with $h_c = 40$ kpc which evolves to 1.5 Gyr. Comparing to the $h_c = 10$ kpc case, no qualitative difference is found in the key properties of the simulation.

3.4.2 AGN feedback

For the fueling of the AGN, we adopt the cold mode accretion model, which has been used in many numerical studies in the literature (e.g., *Gaspari et al.* 2012b, 2013; *Li and Bryan* 2014a,b; *Yang and Reynolds* 2016). The cold gas ($T < 10^5$ K) within the central $r < 0.5$ kpc region is accreted at the rate $\dot{M}_{\rm acc} = M_{\rm in,c}/5$ Myr, where $M_{\rm in,c}$ is the mass of cold gas within $r < 0.5$ kpc. The accretion-powered AGN feedback injects gas and CRs. The gas feedback is purely kinetic with kinetic power ($\dot{E}_{\rm k}$) given by

$$\dot{E}_{\rm k} = \frac{1}{2}\eta \dot{M}_{\rm acc} v_{\rm jet}^2 = \epsilon\eta(1 - f_{\rm cr})\dot{M}_{\rm acc}c^2; \tag{3.13}$$

and the CR feedback power ($\dot{E}_{\rm cr}$) given by

$$\dot{E}_{\rm cr} = \epsilon\eta f_{\rm cr}\dot{M}_{\rm acc}c^2, \tag{3.14}$$

where c is the speed of light, ϵ is the feedback efficiency, η is the mass loading factor and $f_{\rm cr}$ is the CR fraction of the AGN injected energy. We adopted $\epsilon = 3 \times 10^{-4}$ and $\eta = 1$ for all simulations in this work and $f_{\rm cr} = 0.8$ for all simulations that included CRs. The AGN ejecta is launched via bipolar jets. The jet launching base is the innermost 8 cells and the jet precesses around the $z-$axis with the precession angle of 10 degrees and period of 10 Myr.

3.5 Results

We now systematically discuss the results from our simulations. In this section we comment on simulations with progressively more complex physics of the CGM plasma, i.e., we begin with a purely hydrodynamical run (KINETIC run), then discuss its generalization to include magnetic fields (K-MAG run) and CRs including Coulomb and hadronic/pionic losses (CRCP run), and finally comment on the run that extends the above physics to include CR transport via the streaming instability and the associated with it CR heating of the CGM

(CRSH run). Key parameters distinguishing these runs are shown in Table 1, where $f_{\rm cr}$ denotes the fraction of the CR energy in the AGN jet.

3.5.1 AGN feedback in the hydrodynamical case

In the purely hydrodynamical AGN feedback case, the atmosphere goes through cycles of cold gas precipitation and AGN outbursts in the first 1.2 Gyr. At the beginning of each cycle, AGN outburst is triggered by either (i) central gas cooling due to short central cooling time, or (ii) infall of cold gas that condenses out of previously uplifted low entropy gas. The first cycle is initiated by the short central cooling time. The AGN jets perturb the halo triggering thermal instabilities. Consequently, cold gas condenses out of the halo and forms extended structures (see panel a1 in Fig.3.1). Some of the cold clumps fall toward the center, swirl around the central SMBH and eventually get accreted by it. A fraction of cold clumps find themselves in the path of the AGN jet, get fragmented by it, and get either ablated or accreted by the SMBH. Cold gas condensation ends when the AGN heating makes the halo thermally stable. When all cold gas gets consumed or destroyed, the AGN shuts down and the halo returns to the quiescent state (see panel a2 in Fig.3.1) until the next cycle begins. During the precipitation cycles, the cold gas mass fluctuates between $\sim 10^6$ and $\sim 10^8$ $M_\odot$, and the AGN jet power typically ranges between $10^{42.5} \sim 10^{43.5}$ erg $\cdot$ s^{-1} (see top and middle panels in Fig.3.2). This cyclic evolution is a natural result of the self-regulated AGN feedback. Many previous studies of cold mode accretion AGN feedback in giant elliptical galaxies or galaxy clusters led to similar conclusions with regard to the behavior of cold gas mass and jet power fluctuations. The cyclic evolution only lasts for the first 1.2 Gyr, after which the simulation goes into the unphysical *disk phase* described below.

3.5.1.1 Formation of a massive cold disk in the vicinity of the SMBH

In the third precipitation cycle accreting cold gas forms a rotationally-supported disk at $t \approx 1.2$ Gyr. Although the formation of such disks has been seen in many simulations

(e.g., *Li and Bryan*, 2014a; *Eisenreich et al.*, 2017; *Qiu et al.*, 2019b; *Wang et al.*, 2019), we consider the evolution after the disk formation to be unphysical due to the following two reasons.

1. The disk quickly becomes too large and too massive. Since the onset of disk formation, the cold gas mass in the disk increases monotonically as shown in the top panel of Fig.3.2. At $t = 2$ Gyr, the disk grows to 3 kpc in radius (third row of the left column in Fig.3.1) and 10^9 $M_\odot$ in mass. Such massive cold disk is not found in NGC5044 nor in most of the observed elliptical galaxies (*Young et al.*, 2011).

2. The feeding of the AGN from the disk leads to the overheating of the central few kpc region while hot gas continues to cool directly onto the disk. Fig.3.3 shows the average radial distribution of gas cooling time, $t_{\rm cool}(r)$, over two 200 Myr-long intervals – one just before the disk formation, $t = 1 \sim 1.2$ Gyr (left panel) and the other one 600 Myr later, $t = 1.8 \sim 2$ Gyr (right panel); the dashed lines in both panels represent the initial $t_{\rm cool}(r)$. Before the formation of the disk, the system is self-regulated, and the gas cooling and AGN heating are overall in balance with each other. Therefore, $t_{\rm cool}(r)$ is scattered approximately symmetrically around the initial values. In this phase, the cold gas is accreted onto the SMBH and the cold gas is removed from the central regions. However, in later phase, the rate of cold gas consumption by the SMBH and the jet power reach a plateau. This happens because a centrifugally supported disk is formed and the angular momentum is not sufficiently quickly removed from it. Furthermore, because the disk rotates about the jet axis, the AGN outflow cannot intercept the cold gas and is unable to reheat it (this type of reheating is present in the simulations that exhibit cyclic AGN behavior). Therefore, the AGN consistently heats the halo while the disk continues to grow in mass as the hot phase cools and adds mass to it. As shown in the right panel of Fig.3.3, while $t_{\rm cool}(r)$ systematically increases away from the initial condition due to the AGN heating in the 3 kpc $< r <$ 10 kpc region, it cascades down for $r \lesssim 3$ kpc because the gas directly cools onto the disk.

Therefore, even though the AGN overheats the halo, it fails to stop the fast cooling of the gas. The whole system is no longer self-regulated and its thermal properties are systematically changed compared to the initial condition.

3.5.2 AGN feedback in the magneto-hydrodynamical case

We now discuss the impact of magnetic fields on the purely hydrodynamical simulations of the AGN feedback described above. Similarly to the KINETIC case, in the K-MAG case the atmosphere and the AGN undergo cyclic variations. In the K-MAG case thermal instability is also present and cold gas clouds decouple from the hot atmosphere. However, unlike in the KINETIC case, massive cold disk surrounding the SMBH does not form (c.f. last row of the first and second column in Fig.3.1). Moreover, the atmosphere remains in a state of global thermodynamic equilibrium without overheating in the time-averaged sense throughout the simulation time, rather than exhibiting overheating that occurs in the KINETIC case at about 1.2 Gyr. As we argue below, both of these differences can be attributed to the impact of magnetic tension acting on the clouds and magnetic braking that leads to more efficient extraction of angular momentum and accretion of the cold clumps onto the central SMBH.

3.5.2.1 Morphology of the precipitating clouds

In order to unravel the reason for the absence of cold disks in the K-MAG case, we now turn our attention to the morphology of the clouds. To this end, we compare how cold clumps evolve in the KINETIC and K-MAG runs and analyze one event of the infall of an isolated cold clump in each run. Fig.3.4 shows snapshots of the projected density at the beginning of the infall of isolated clumps (top row) and at the time when the cold clumps reach the center (bottom row). Arrows point to the locations of the cold clouds when they are compact. While in the KINETIC case (left column) the cloud appears compact throughout its infall, in the K-MAG case the cloud is compact in the beginning and then

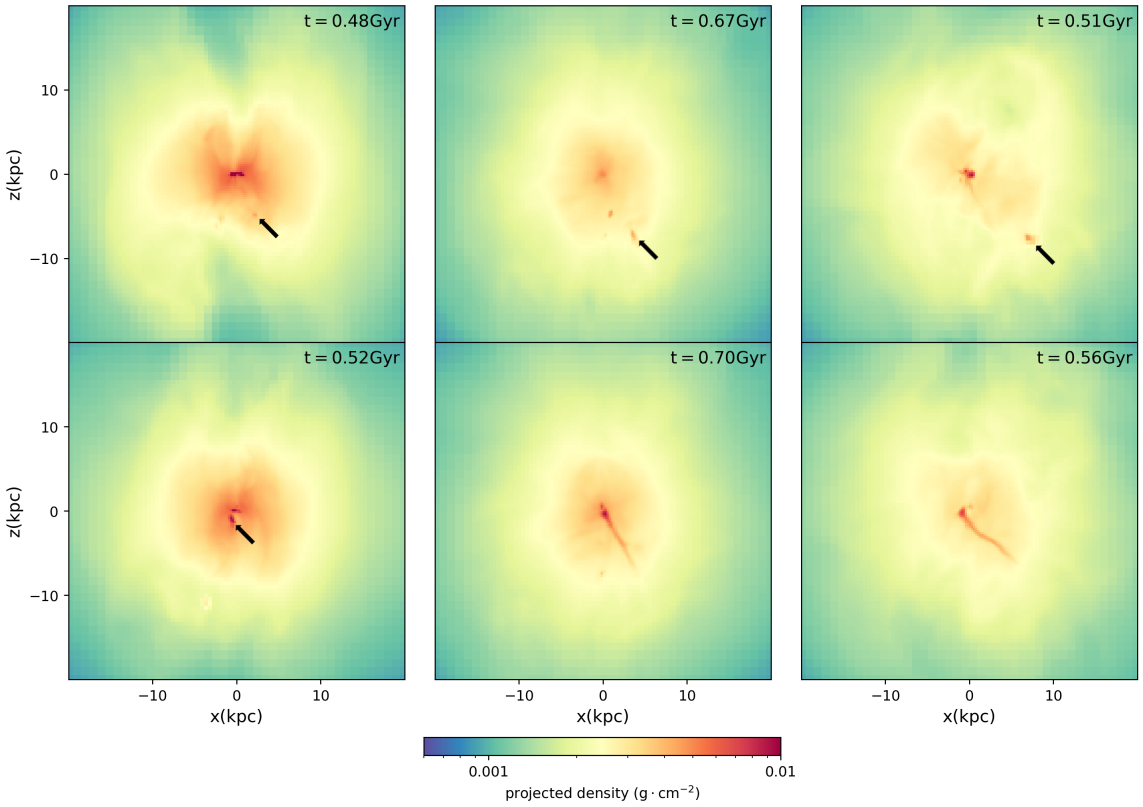

Figure 3.4: Infall of an isolated cold clump in (from left to right column) KINETIC, KMAG, and CRSH runs. In each column, the top row is the projected density snapshot at the time when the condensed cold clump starts to fall in and the bottom row corresponds to the epoch when the head of the clump reaches the center. Arrows point to the locations of the cold clouds when they are compact.

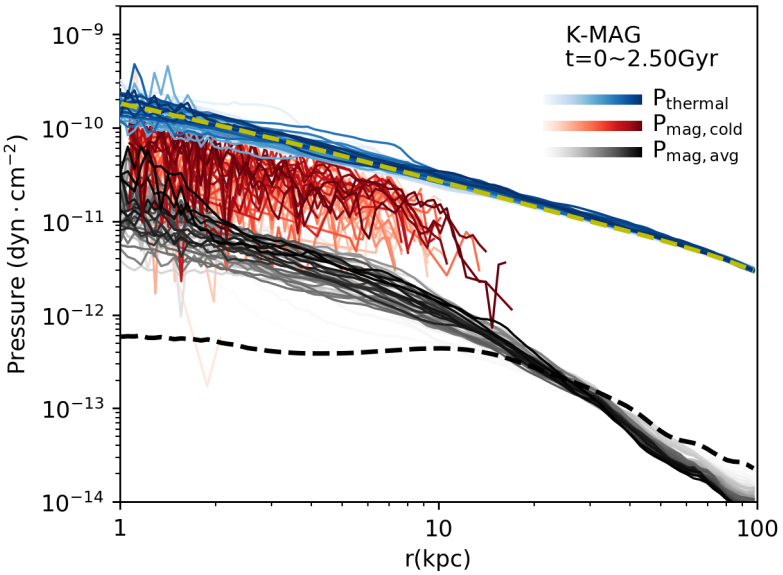

Figure 3.5: Three sets of pressure profiles: thermal pressure (blue), magnetic pressure in the regions occupied by the cold gas (red), and magnetic pressure averaged in spherical shells (grey). For each set, the profiles are plotted every 50 Myr from light to dark color. For clarity, the initial thermal and magnetic pressure profiles are shown as yellow and black dashed lines, respectively.

becomes extremely filamentary as it reaches the center. The filaments are approximately aligned with the radial direction, which to first order coincides with the infall trajectory (see middle column). This difference in the morphology of the cold gas clouds between KINETIC and K-MAG cases strongly suggests that magnetic forces may be important. We note in passing that the clouds in the KINETIC case also become filamentary in those cases where they directly interact with the AGN outflow.

3.5.2.2 Impact of magnetic fields on the cold phase morphology

Although the mean magnetic field in the CGM is dynamically weak (initial plasma $\beta \sim 100$), this does not preclude a possibility that the B-field could be locally enhanced. In Fig.3.5 we show the profiles of the thermal pressure (in blue), magnetic pressure averaged in spherical shells (in gray), and the magnetic pressure in cold gas regions ($T < 10^5$K). In each category, different lines correspond to different simulation times with darker lines

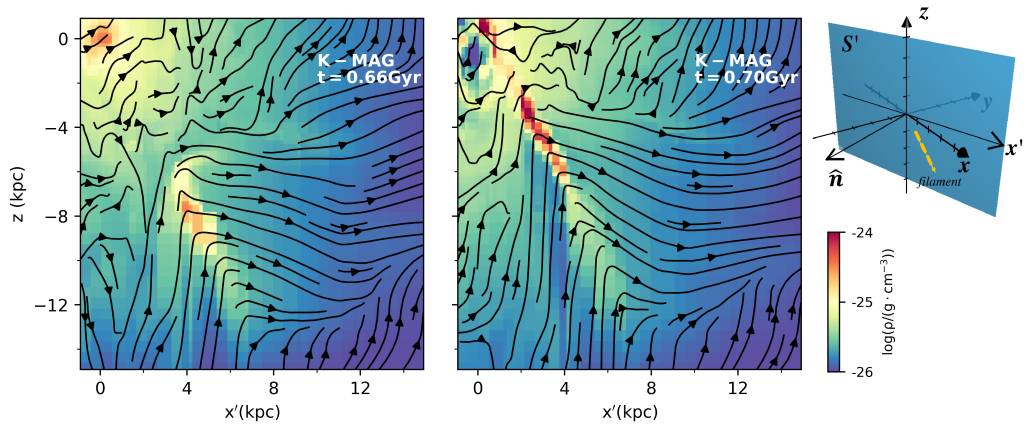

Figure 3.6: Left and middle panel: distribution of gas density and magnetic field lines on the plane S' at the epoch of the formation of a single filament (left, $t = 0.66$ Gyr) and at the epoch when the filament head reaches the center (middle, $t = 0.70$ Gyr). The gas density and magnetic field lines are shown as color maps and stream lines, respectively. Upper right panel: the position of plane S' relative to the x, y, z axes of the simulation box. The normal vector and the intersection with the $x - y$ plane of S' are labelled as $\hat{n}$ and x', respectively. The plane S' slices the volume through the bulk of the filament, which is schematically shown as the orange dashed line.

corresponding to later times. As expected, the average plasma $\beta \gg 1$. Interestingly, the cold gas phase is spatially correlated with enhanced magnetic field strength.

3.5.2.3 magnetic braking and cold gas velocity distribution

The local B-field amplification occurs due to flux freezing during the condensation of the cold gas followed by the field amplification during cloud infall. This amplification could occur on the leading edge of the cloud as well as in the filamentary tail. As the clumps fall to the center, the strong magnetic fields are stretched and exert tension force in the direction anti-parallel to the clump velocity direction. This mechanism is clearly shown in Fig.3.6, which shows the gas density distribution on a plane containing the cold filament at two different times (see left and middle panels). The spatial orientation of this plane is shown in the upper right panel of Fig.3.6. The magnetic field lines are shown as arrows. As the cold clump is falling to the center, it bends and stretches the magnetic field lines. The field

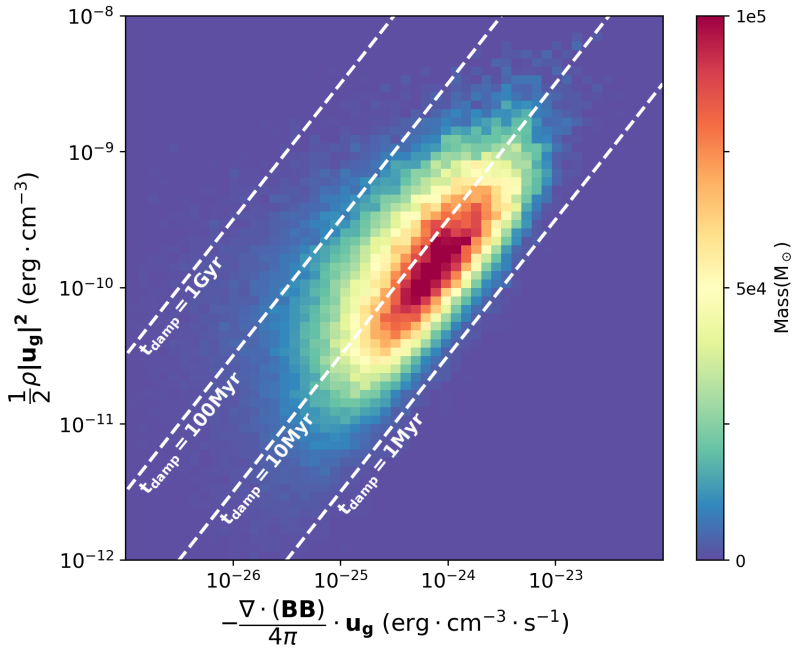

Figure 3.7: Kinetic energy - magnetic tension "resistence" phase plot of the cold gas in K-MAG run. Color represents the cold gas mass. The distribution is averaged over snapshots sampled every 2 Myr within $t = 0 - 2.5$ Gyr. Dashed lines denote the damping time scale $t_{\rm damp} = 1, 10, 100$ Myr and 1 Gyr. The damping time-scale is defined as the time-scale over which the work done by the magnetic tension force depletes the kinetic energy of the gas.

lines exert strong tension force on the cold clump. Any gas that is stripped from the cloud is confined to the ordered fields lagging behind the cloud and slides along these fields forming long cold filaments.

We can now quantify the magnitude of the tension force in the vicinity of the clouds and estimate the time-scale over which it could significantly affect the kinetic energy of the cold gas clumps. The magnetic tension force density is

$$\mathbf{f_t} = \frac{1}{4\pi}\nabla\cdot(\mathbf{BB}) \tag{3.15}$$

We found that, on average, 75 per cent of the cold gas mass has $\mathbf{f_t}\cdot\mathbf{u_g} < 0$, i.e., that the magnetic tension force does negative work on most of the cold phase. This cold gas can thus be decelerated within a short time-scale due to this tension force. Fig.3.7 shows the time-

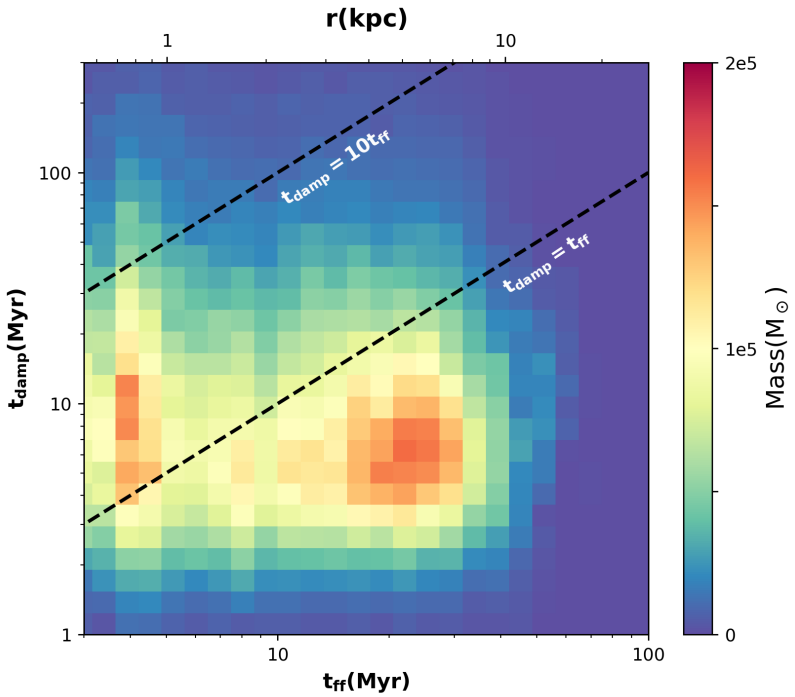

Figure 3.8: The damping time vs. free-fall time ($t_{\rm damp}$ vs. $t_{\rm ff}$) phase plot of the cold gas in K-MAG run. Color represents the cold gas mass. The distribution is averaged over snapshots sampled every 2 Myr within the first 2.5 Gyr. Dashed lines denote the $t_{\rm damp} = t_{\rm ff}$ and $10t_{\rm ff}$. The upper horizontal axis shows the radii according to the dynamical time.

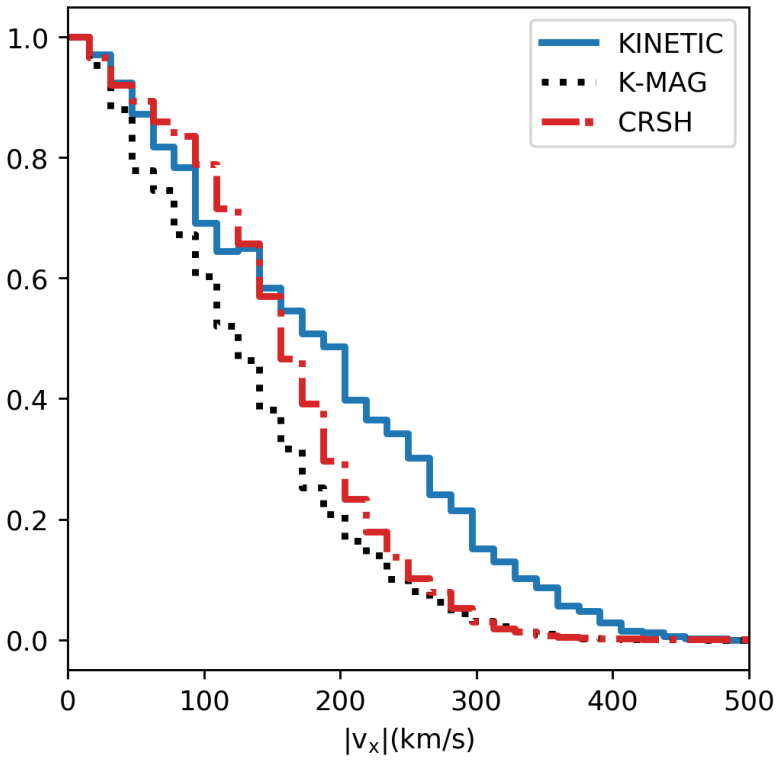

Figure 3.9: Distribution of the magnitude of the cold gas ($T < 10^5$ K) velocity along $x-$axis in KINETIC, KMAG, and CRSH run. The three distributions are weighted by gas mass and averaged over the first 1.2 Gyr.

averaged distribution of the cold gas in the K-MAG case on the plane defined by the kinetic energy density $\frac{1}{2}\rho u_g^2$ and the magnetic tension power density $-\mathbf{f_t} \cdot \mathbf{u_g}$. Color represents the cold gas mass. We define the "damping time" as $t_{\rm damp} = -0.5\rho u_g^2/(\mathbf{f_t} \cdot \mathbf{u_g})$. This is the time-scale over which the work done by the magnetic tension force uses up all the kinetic energy of the cold gas. The white dashed lines in Fig.3.7 denote $t_{\rm damp} = 1, 10, 100$ Myr and 1 Gyr, respectively. The damping time of bulk of the gas is about 10 Myr, which is much shorter than the duration of the simulations and shows that magnetic forces have enough time to significantly affect the dynamics of the cold gas and its morphology. Fig.3.8 shows the time-averaged distribution of cold gas on the plane defined by $t_{\rm damp}$ and the free-fall time, $t_{\rm ff} = \sqrt{2r/g(r)}$. The dashed lines in Fig.3.8 denote $t_{\rm damp} = t_{\rm ff}$ and $10t_{\rm ff}$. Most of the cold gas resides in the region where and $t_{\rm damp} < 10t_{\rm ff}$, which implies that the magnetic forces can significantly alter the orbits of filaments and lead to dramatic enhancement in the rate of momentum extraction via magnetic braking, which explains why K-MAG run never transitions to the disk phase. We note that the mass concentration at $t_{\rm ff} \approx 4$ Myr in Fig.3.8 is due to the residual angular momentum of the cold gas along the $z-$direction. This cold gas forms transient disk with significantly sub-Keplerian velocity and is quickly accreted.

Significant magnetic tension forces that are anti-parallel to the velocity vectors of the cold gas not only affect the morphology of that gas phase but also modify its velocity distribution. Fig.3.9 shows the average distribution of the magnitude of the cold gas velocity along the $x-$axis. To make an equivalent comparison between the runs, we only include the data for the first 1.2 Gyr, during which both the KINETIC and K-MAG runs experience similar cyclic evolution. This figure clearly demonstrates that the cold gas in KINETIC run (solid blue line) has a high-velocity tail that is absent in the K-MAG case (dotted black line).

3.5.2.4 Ambipolar diffusion of magnetic fields

The impact of magnetic tension on the cloud velocity can be reduced when the magnetic fields are allowed to slide past the clouds. This can happen as a result of ambipolar

diffusion since the clouds are only partially ionized. In order to assess the impact of this process, we estimate the ambipolar diffusion time-scale on which the field sliding occurs, $t_{\rm ad} \sim L^2 \nu_{\rm in}/u_{\rm A}^2$, where L is the filament width, $u_{\rm A} = B/(4\pi\rho_i)^{1/2}$ is the Alfvén speed, ρ_i is the ion mass density, and $\nu_{\rm in} \sim 10^{-9} T_2^{1/2} n_n$ s^{-1} is the ion-neutral collision frequency (*De Pontieu et al.*, 2001), where n_n is the number density of neutrals and $T_2 = T/10^2$K, where T is the cold phase temperature. We can compare this time-scale to the dynamical time $t_{\rm dyn} \sim R/u$, where R is the distance of a cloud from the center and u is its velocity,

$$\frac{t_{\rm ad}}{t_{\rm dyn}} \sim 1.3 \times 10^{-8} x(1-x) T_2^{1/2} \frac{m_p n_H^2 L^2}{B^2} \frac{u}{R}, \tag{3.16}$$

where x is the ionization fraction, and n_H is the number density of hydrogen. In realistic filaments most of the gas mass is likely to in the molecular form (*Ferland et al.*, 2008, 2009). Assuming that, for low ionization, recombination are balanced by CR ionization, we can estimate the ionization fraction as $x \sim K/n_n^{1/2}$, where $K \sim 10^{-5}$cm$^{-3/2}$ (*McKee et al.*, 1993; *Padoan et al.*, 2000). This estimate for the ionization fraction assumes ionization rate $\zeta_H = 10^{-17}$s^{-1} *Spitzer* (1978). Since this ionization rate is uncertain and can be larger (e.g., *Indriolo et al.* (2010, 2018)), and $K \propto \zeta_H^{1/2}$, the above estimate for the ionization fraction is likely a lower limit. For typical, if somewhat conservative, filament parameters $R \sim 10$ kpc, $L \sim 10$ pc (*Fabian et al.*, 2008), $u \sim 200$ km s^{-1}, $n_H \sim 2 \times 10^4$ cm^{-3}, $T \sim 10^2$ K, and $B \sim 50\mu$G (see *Werner et al.* (2013) for the estimates of the last three quantities), we obtain $t_{\rm ad}/t_{\rm dyn} \sim 1.4 \times 10^2$. This implies that ambipolar diffision is unlikely to lead to significant magnetic line slippage past the cold filaments. While detailed predictions for the filament powering rates are beyond the scope of this work, we also estimated that unlike other mechanisms proposed to significantly contribute the filament powering (e.g., *Fabian et al.* (2011); *Ferland et al.* (2008); *Churazov et al.* (2013); *Ruszkowski et al.* (2018)), the ambipolar drift heating rate is unlikely to account for the observed amount of power emitted by the Hα filaments, which is consistent with relatively long ambipolar diffusion

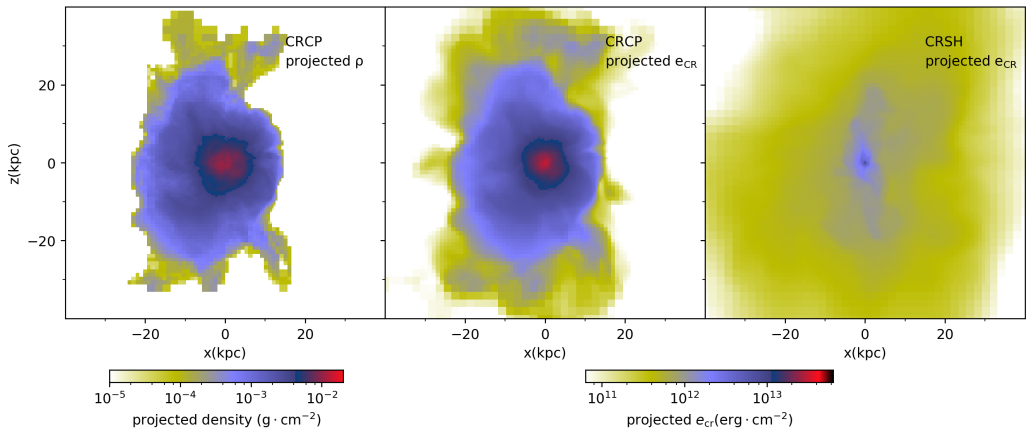

Figure 3.10: Projected cold gas ($T < 10^5$ K) density (left) and CR energy in the CRCP (middle) and CRSH (right) cases at $t = 1.43$ Gyr. The projections are along the y-axis and cover the central 80 kpc-wide cubic region.

time-scales. These conclusions become even stronger for the case of filaments composed predominantly of Hα-emitting gas of typical density of ~ 30 cm^{-3} and $T \sim 10^4$K (*Werner et al.*, 2013).

3.5.3 AGN feedback including magnetic fields and CRs

As mentioned in the introduction, AGN jets inflate cavities in the CGM that can be dominated by CRs. CR simulations of AGN feedback (*Yang et al.*, 2019) suggest that such CR-filled bubbles could uplift more cold thermally unstable gas because they have lower inertia and flatten in the direction perpendicular to the radial direction, which increases their cross section. These short-duration simulations also show that there is not enough time to transfer the CR energy from the bubbles to the ambient CGM. We now extend the results presented in the above sections to include CR-dominated bubbles inflated by AGN jets in order to study their long-term impact on the CGM.

3.5.3.1 Simulations without CR streaming

We begin by including CRs and their losses via Coulomb and hadronic interactions with the CGM (run CRCP). These processes heat the thermal CGM. The CRCP run does not

exhibit a cycling behavior seen in the KINETIC and K-MAG cases. Instead, it suffers from the cooling catastrophe despite the fact that the AGN continues to inject energy. Cold gas piles up in the center since the early times in the simulation ($t \approx 120$ Myr) and forms an overdense region that gradually grows with time (see third column in Fig.3.1). The cold gas mass increases monotonically as shown in the top panel of Fig.3.2. At $t \approx 1.4$ Gyr, the mass of the cold gas reaches $\sim 10^{10}$ $M_{\odot}$. This is two orders of magnitude more than typical values seen in elliptical galaxies. Therefore, we stop the simulation at $t \approx 1.4$ Gyr. One fundamental difference between the CRCP case and the KINETIC and K-MAG cases is that the energy transfer from the bubbles to the CGM proceeds at different rates. While in the KINETIC and K-MAG cases the thermal bubble gas eventually mixes with the surrounding CGM and instantly transfers its energy to the CGM, in the CRCP case the CRs that come into contact with the CGM due to mixing need time to transfer their energy to the CGM via Coulomb and hadronic interactions. Assuming that the bubbles are in pressure equilibrium with the CGM, we can estimate the heating time-scale $t_{\rm heat}$ using Eq. 6 and 7. For typical conditions in the cool core at 10 kpc away from the center ($n_p \sim 10^{-2}$ cm^{-3}, $T \sim 10^7$ K), we obtain $t_{\rm heat} \sim 1$ Gyr, which is a significant fraction of the simulation duration and suggests that the energy transfer from CRs to the CGM should be inefficient.

Fig.3.10 shows the projected distribution of the cold gas density (left panel) and CR energy density in the CRCP run (middle panel) at $t \approx 1.4$ Gyr. The two distributions are very similar, which indicates that the cooling gas from the outer parts of the cool core flows in and traps the CR fluid in the region occupied by the cold gas. Although energetic CRs are co-spatial with the cold gas, the inefficient CR heating is unable to reheat the cold gas, which has excessively short cooling times. Consequently, cold gas accumulates in the center and the CRCP run suffers from a cooling catastrophe. Similar result was found in the context of cluster simulations (*Ruszkowski et al.*, 2017a).

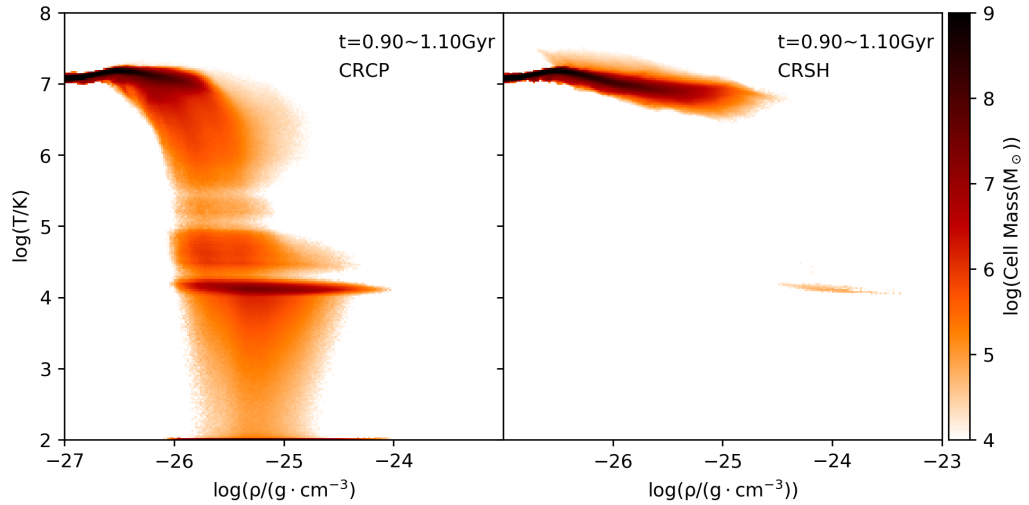

Figure 3.11: The average temperature - density phase diagrams plotted over $t = 0.9 \sim 1.1$ Gyr in CRCP (left) and CRSH run (right). The averaging method is the same as that used by Fig.3.3. Color shows the gas mass.

3.5.3.2 Simulations with CR streaming and heating

We now extend the CR simulations of AGN feedback discussed above to include the effect of the CR streaming instability (CRSH run). That is, we include CR streaming with respect to the thermal gas and the associated CR heating of the CGM. The right panel in Fig.3.10 shows the projected distribution of the CR energy density in the CRSH run. This figure clearly demonstrates that the spatial distribution of CRs can be much broader in this case compared to the one where CR transport is neglected (CRCP run; middle panel). The better dispersal of CRs throughout the CGM in the CRSH case compared to CRCP case leads to more efficient heating as the CRs can come into contact with more hot thermal gas. It is evident from the comparison of the middle and right panels in Fig.3.10 that the energy density of CRs is lower in the CRSH case compared to CRCP case. The decrease in the CR energy density is due to a combination of adiabatic expansion and streaming of CRs and the additional heating of the gas associated with the CR streaming instability. This heating time-scale is $t_{\rm heat,A} \sim 3L/u_A$, where L is the scalelength of the CR gradient where significant heating takes place. Periods of the most significant CR heating coincide with the AGN

name	$E_{\rm agn}$(erg)	$E_{\rm cr}$(erg)	$E_{\rm cr,used}$(erg)	$\frac{E_{\rm cr,used}}{f_{\rm cr}E_{\rm AGN}}$
CRCP	2.41×10^{59}	6.28×10^{58}	1.30×10^{59}	84%
CRSH	1.81×10^{59}	2.33×10^{58}	1.22×10^{59}	67%

Table 3.2: Components of AGN energy

outbursts when the pressure gradients of CR escaping from the jet regions are the strongest, and there is relatively little heating between AGN episodes when the CRs have had time to disperse substantially. Depending on the steepness of the CR pressure gradient, $t_{\rm heat,A}$ can be significantly shorter than the heating time-scale $t_{\rm heat}$ corresponding to Coulomb and hadronic losses described above (e.g., $\sim 5 \times 10^7$yr for $L \sim 1$ kpc and assuming $\beta = 10^2$). Similar effect was observed in the context of CR simulations of AGN feedback in galaxy clusters (*Ruszkowski et al.*, 2017a). Consequently, the cooling catastrophe that was present in the CRCP case does not occur. This is illustrated in Fig.3.11 that shows the temperature versus gas density phase space. In the left panel, that corresponds to the CRCP run, large quantities of dense and low temperature gas can be seen, whereas only a relatively very small amounts of precipitating gas can be seen in the right panel that corresponds to the CRSH case. Similarly to the K-MAG case, the CRSH case also exhibits cyclic behavior that was absent in the CRCP run (See orange line in Fig.2). Finally, the impact of the magnetic fields on the precipitating clouds in the CRSH case is also reminiscent of that seen in the K-MAG run (see right panel in Fig. 4). Consequently, the distribution of cold cloud velocities in the CRSH is also similar to that corresponding to the K-MAG case (see red line in Fig. 8) and the cold disk surrounding the SMBH does not form, which is in agreement with observations that suggest that such disks are seen in a relatively small number of systems.

That the evolution of the CRCP run differs so substantially from that seen in the CRSH run suggests that CR streaming plays a decisive role in determining whether the CR-dominated AGN jets could efficiently deliver the energy to the CGM. To better understand how efficiently the AGN energy is supplied to the CGM, we analyze the following quantities in these two runs: total energy released by the AGN $E_{\rm agn}$, total energy of the CR fluid that

remains in the simulation box $E_{\rm cr}$, and the CR energy transferred to the gas $E_{\rm cr,used} = f_{\rm cr}E_{\rm AGN} - E_{\rm cr}$ computed assuming negligible CR outflow through the box boundary. In principle, $E_{\rm cr,used}$ should exceed the energy that is actually used to heat the gas because a fraction of CR energy that lost due to hadronic collisions is removed from the system via gamma ray and neutrino emission. However, we verified that the hadronic energy losses in both cases are small compared to other terms and therefore approximately all of $E_{\rm cr,used}$ is utilized to heat the gas. Comparison of these quantities for the CRCP and CRSH runs at $t \approx 1.2$ Gyr (see Table 2) reveals that: (i) $E_{\rm agn}$ is larger in CRCP run than that in CRSH run. This is likely caused by the weak coupling of the AGN energy to the gas. One manifestation of this is the fact that while in the CRCP run the AGN is continuously injecting energy, the CRSH run undergoes a quiescent phase at $t \approx 750$ Myr during which AGN releases zero energy as the atmosphere is relatively close to being in the state of global thermal equilibrium (the solid orange line in the middle panel of Fig.2); (ii) the above finding is consistent with the observation that, due to the additional streaming heating, CR energy is more efficiently utilized in CRSH run, i.e., $E_{\rm cr,used}/(f_{\rm cr}E_{\rm AGN}) \approx 84\%$ and $\approx 67\%$ in the CRSH and CRCP cases, respectively.

The total CR energy transferred to gas is slightly higher in the CRCP (as the AGN is trying to compensate for the low heating efficiency), but the heating in this case still fails to balance cooling globally. However, the ability of the AGN to shut off catastrophic cooling of the atmosphere depends not only on the total amount of energy transferred to it but also on how uniform the heating is distributed and how much of the cooling gas can come into contact with CRs. As mentioned above, the spatial distribution of CRs is broader in the CRSH case which, together with the fact that the amount of the injected energy is better utilized in this case, explains why the cooling catastrophe is prevented when CR streaming effects are included.

The better utilization of the AGN energy is also evident from the bottom panel in Fig.3.2. This figure shows the evolution of the total AGN energy $E_{\rm AGN}$. The smallest

values of $E_{\rm AGN}$ correspond to the CRSH case, i.e., the smallest values of AGN energy suffice to offset cooling in a time average sense and prevent cooling catastrophe.

3.6 Conclusions

We performed MHD simulations of AGN feedback in elliptical galaxies including the effects of CR heating and streaming. In these simulations we followed the evolution for a long period of time (Gyrs). We found that non-ideal hydrodynamical effects have a profound impact on the evolution of elliptical galaxies. In other words, the evolution of the systems on 100 kpc scales depends sensitively on the physics governing the "microscopic" scales relevant to plasma physics. Specifically, we showed that

1. in the purely hydrodynamical case, the AGN jet initially maintains the atmosphere in global thermal balance. However, local thermal instability eventually leads to the formation of massive cold disk in the vicinity of the central SMBH. This is a generic finding. Similar conclusion was found in other grid-based and smooth particle hydrodynamics simulations performed by other groups. Once the disk has formed, it continues to feed the central SMBH and the jet begins to overheat the central regions of the atmosphere and does not prevent fast cooling of the gas in the direction perpendicular to it close to the center. Thus the AGN-to-CGM energy coupling is weak due to the inflow-outflow geometry very close to the SMBH. This leads to further disk growth and excessive buildup of the cold gas in the very center, which is in disagreement with the observations;

2. including high-β magnetic fields prevents the formation of the cold disks. The removal of the cold gas from the central regions is due to local B-field amplification in the cold precipitating gas and increased magnetic braking acting on the cold blobs. The local field amplification occurs via flux freezing during the development of local thermal instability, which is followed by stretching of the fields caused by the motion

of the cold gas clumps that dynamically decouple from the hot gas. The B-field line stretching leads to filamentary/cometary appearance of the cold clouds that do not fall ballistically onto the center. In a statistical sense, the magnetic tension vectors are anti-parallel to the cold cloud velocities, which leads to magnetic braking of the cold clouds. Even though the magnetic field in both the cold and hot phases remains dynamically weak throughout the evolution, the tension forces acting on the cold clouds are capable of affecting their dynamics on time-scales much shorter than the evolutionary time-scale of the system. We also find that magnetic fields can narrow the velocity distribution of the cold phase (compared to that observed in the purely hydrodynamical case);

3. when plasma composition in the AGN jets is dominated by CRs, and CR transport is neglected, the atmospheres exhibit cooling catastrophes due to the inefficient heat transfer from the AGN to CGM despite Coulomb/hadronic CR losses being present. In this case, CRs continue to accumulate in the center due to the fact that CRs do not come into direct contact with sufficiently large fraction of the radiatively cooling atmosphere. CR energy is not utilized very efficiently due to the lack of transport and the fact that typical CR cooling time-scales associated with Coulomb and hardonic interactions are a substantial fraction of the system lifetime;

4. including CR streaming and heating restores the agreement with the observations, i.e., cooling catastrophes are prevented, the gas does not overheat, and massive cold central disks do not form. The AGN power is reduced as its energy is utilized efficiently.

CHAPTER IV

Non-Kolmogorov Turbulence in Multiphase Intracluster Medium Driven by Cold Gas Precipitation and AGN Jets

4.1 Preface

The results presented in this chapter were published in: *Wang, C., et al. "Non-Kolmogorov turbulence in multiphase intracluster medium driven by cold gas precipitation and AGN jets." Monthly Notices of the Royal Astronomical Society 504.1 (2021): 898-909.* and are reproduced here with minor style revisions.

4.2 Abstract

Active galactic nuclei (AGN) feedback is responsible for maintaining plasma in global thermal balance in extended halos of elliptical galaxies and galaxy clusters. Local thermal instability in the hot gas leads to the formation of precipitating cold gas clouds that feed the central supermassive black holes, thus heating the hot gas and maintaining global thermal equilibrium. We perform three dimensional magnetohydrodynamical (MHD) simulations of self-regulated AGN feedback in a Perseus-like galaxy cluster with the aim of understanding the impact of the feedback physics on the turbulence properties of the hot and cold phases of the intracluster medium (ICM). We find that, in general, the cold phase velocity structure function (VSF) is steeper than the prediction from Kolmogorov's theory. We attribute the

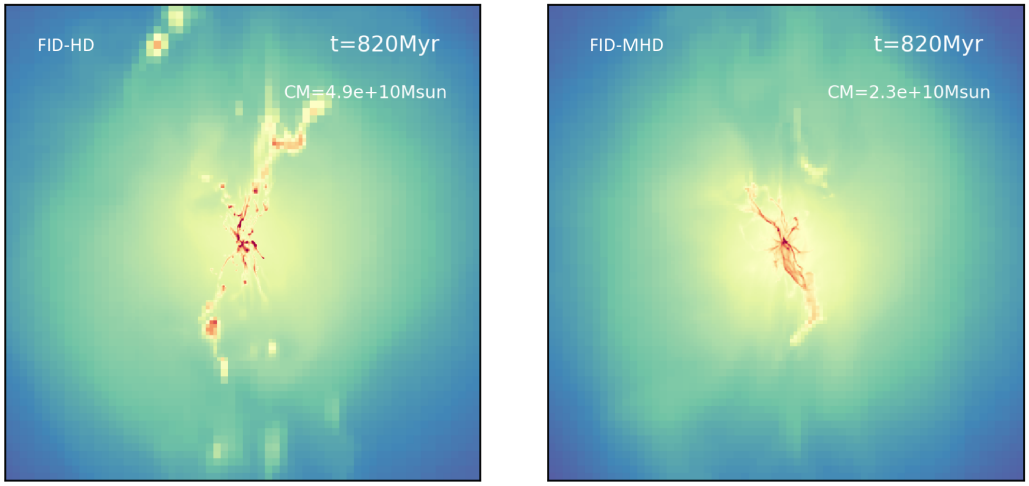

Figure 4.1: Snapshots of the projected gas density from our fiducial hydrodynamical (FID-HD; left) and fiducial MHD (FID-MHD; right) runs. The projection is done along the x-axis and within the central 125 kpc-wide cube. It is clear that cold filaments are more spatially confined in FID-MHDthan FID-HD.

physical origin of the steeper slope of the cold phase VSF to the driving of turbulent motions primarily by the gravitational acceleration acting on the ballistic clouds. We demonstrate that, in the pure hydrodynamical case, the precipitating cold filaments may be the dominant agent driving turbulence in the hot ICM. The arguments in favor of this hypothesis are that: (i) the cold phase mass dominates over hot gas mass in the inner cool core; (ii) hot and cold gas velocities are spatially correlated; (iii) both the cold and hot phase velocity distributions are radially biased. We show that, in the MHD case, the turbulence in the ambient hot medium (excluding the jet cone regions) can also be driven by the AGN jets. The driving is then facilitated by enhanced coupling due to magnetic fields of the ambient gas and the AGN jets. In the MHD case, turbulence may thus be driven by a combination of AGN jet stirring and filament motions. We conclude that future observations, including those from high spatial and spectral resolution X-ray missions, may help to constrain self-regulated AGN feedback by quantifying the multi-temperature VSF in the ICM.

4.3 Introduction

Hot and dilute plasmas in elliptical galaxies and galaxy clusters often exhibit cooling times shorter than the Hubble time. These short cooling times lead to local thermal instability in the hot atmospheres of these objects. The observational evidence for this instability comes in the form of detection of molecular and Hα+[N II] emission from dense and cold gas (e.g., *Lakhchaura et al.*, 2018; *Pulido et al.*, 2018; *Babyk et al.*, 2019; *Olivares et al.*, 2019). The systems containing the cold gas are characterized by relatively shorter radiative cooling times, higher overall gas density, lower entropies, and less symmetric X-ray emissivity distributions caused by gas motions (e.g., *Lakhchaura et al.*, 2018). While there continues to be a debate on whether in the locally thermally unstable systems the ratios of the cooling time to the free-fall time are systematically lower (see *Lakhchaura et al.* (2018) for evidence in favor of this hypothesis and *Babyk et al.* (2019) for the opposing view), there is emerging consensus that the cold gas has cooled out of the hot plasma.

Since the cool and thermally unstable gas is expected to be unsupported by the pressure gradients in the hot gas phase, the cold phase precipitates and feeds the central supermassive black holes (e.g., *Werner et al.*, 2013, 2014). There is well-established evidence for active galactic nuclei feedback from black holes in the systems characterized by short radiative cooling times. For example, recent LOFAR observations by *Bîrzan et al.* (2020) of X-ray cavity systems present in such systems confirm that there is a connection between radio emission and AGN jet power inflating the cavities.

Observations of cold gas precipitation and AGN feedback in these systems have spurred theoretical investigations aiming to explain the feedback cycle. Using idealized numerical experiments in which heating was distributed globally to balance cooling in the time average sense, *McCourt et al.* (2012); *Sharma et al.* (2012); *Gaspari et al.* (2013) demonstrated that heated atmospheres can remain in global thermal equilibrium while exhibiting local thermal instability. In these models, thermal instability led to precipitation of cold gas, feeding of the central engine, and subsequent heating to balance radiative cooling globally.

Using analytic methods to interpret recent simulations of feedback, *Voit et al.* (2017) considered two condensation modes – (i) precipitation and infall and (ii) uplift of ambient gas by outflows followed by condensation – and argued in favor of the former. An alternative suggestion was made by *McNamara et al.* (2016) who proposed that cold clouds condense out of the low-entropy gas uplifted by the AGN bubbles.

Hydrodynamical AGN feedback simulations including bipolar jet outflows were performed by *Gaspari et al.* (2012b); *Li et al.* (2017); *Martizzi et al.* (2019); *Wang et al.* (2019). These simulations were successful in establishing (i) self-regulating feedback cycle, where the balance of cooling and heating was achieved globally, and where the amount of energy injected by the jets was regulated by the amount of accretion of the cold gas, and (ii) predicting density, temperature, and entropy profiles in agreement with the observations. In particular, the simulations by *Wang et al.* (2019) of self-regulated AGN feedback can maintain the observed properties of single and multi phase halos, which is consistent with analytical models (*Voit et al.*, 2015b) and recent observations (*Frisbie et al.*, 2020). Using a similar approach, albeit excluding the formation of the cold phase clouds, *Yang and Reynolds* (2016) performed a careful analysis of various contributions to the AGN heating budget. Specifically, they demonstrated that a substantial contribution to heating comes from shock heating and turbulent mixing (inside the jet cones) and weak shocks and adiabatic compression (outside the jet cones). The importance of sound wave heating was recently put on a firmer footing (*Bambic and Reynolds* 2019, see also *Ruszkowski et al.* 2004a,b).

The nature of the simulated AGN feedback cycle and the properties of the multiphase gas depend on the physics included in the simulations. Recent results by *Beckmann et al.* (2019) demonstrate that while both the precipitation and uplift of dense gas is present in the simulated atmospheres, purely hydrodynamical simulations struggle to regulate the cluster cooling-feedback cycle and lead to very clumpy distributions on cold gas that is inconsistent with the very filamentary cold structures seen in the observational data. These findings un-

derscore the importance of investigating the impact of a wider array of physical processes in the simulations. *Qiu et al.* (2019a) performed hydrodynamical simulations of self-regulated feedback including the effects of radiation feedback, and while they observed the formation of elongated filaments, the simulations also resulted in the formation of overly massive cold central disks.

MHD simulations of AGN jet feedback with super-Lagrangian resolution and including the effect of cosmic ray (CR) pressure were performed by *Weinberger et al.* (2017a). Single injection AGN events were studied using CR MHD simulations including CR diffusion and Alfvén wave cooling, thus emulating CR streaming, by *Ehlert et al.* (2018), who concluded that CR heating rates were significant compared to cooling and matched radial CR pressure profiles of one-dimensional steady-state CR heating models (*Jacob and Pfrommer* 2017a,b, see also *Guo and Oh* 2008). The CR pressure of AGN lobes is also consistent with the missing thermal pressure as inferred from Sunyaev-Zel'dovich observations of the extreme AGN outburst in MS0735 (*Abdulla et al.*, 2019; *Yang et al.*, 2019; *Ehlert et al.*, 2019). CR MHD simulations of self-regulated AGN jet feedback cycle including the effects of CR streaming, and associated with it CR heating of the gas, were performed by *Ruszkowski et al.* (2017a) and *Wang et al.* (2020), who demonstrated that CR could serve as a dominant heating agent to keep the atmospheres in global thermodynamical equilibrium. *Wang et al.* (2020) also demonstrated that the magnetic fields play a crucial role in angular momentum redistribution via magnetic braking of the precipitating cold gas, which allows the gas to accrete and feed the central supermassive black hole without invariably forming massive cold central tori. More broadly, this suggest that the magnetic fields may play a role in shaping the statistical properties of the velocity distribution of the gas in these systems.

As mentioned above, AGN feedback, cold gas precipitation, and the physics relevant to the problem of the feedback cycle are all intricately related to the question of turbulence in the atmospheres of galaxies and clusters. Thus turbulence measurements could provide constraints on how the AGN feedback works in realistic systems. A recent review

of turbulence in the hot halos of ellipticals and clusters has been presented by *Simionescu et al.* (2019). Constraints on the level of turbulence have been obtained from non-spatially-resolved line broadening. *Sanders and Fabian* (2013) reported velocity limits of 300 to 500 km s^{-1} in elliptical galaxy atmospheres. Using a combination of resonant scattering and line broadening, *Ogorzalek et al.* (2017) measured turbulent velocities in the hot halos of giant ellipticals and found typical Mach numbers of ~ 0.45. Direct measurements of the level of turbulence in the Perseus cluster obtained using the Hitomi mission (*Hitomi Collaboration et al.*, 2016, 2018) are consistent with relatively low level of turbulence in this cluster. Future high spectral and spatial resolution X-ray missions may be able to quantify the level of turbulence in significantly more detail by measuring the velocity power spectrum or VSF of the hot gas phase (*Zhuravleva et al.*, 2012; *ZuHone et al.*, 2016). Recently, a very promising alternative approach to constraining turbulence has been presented by *Li et al.* (2020), who measured the VSF of the cold gas phase and showed that the slope of the cold phase VSF departs from the Kolmogorov prediction. Motivated by these observations, *Hillel and Soker* (2020) simulated the VSF in non-radiative simulation of AGN jet outburst and concluded that the VSF is steeper than that expected based on the Kolmogorov theory of turbulent cascade. In this paper, we study via MHD simulations of the self-regulated AGN feedback, the properties of turbulence in the hot and cold phases of the intracluster medium. In particular, we discuss the coupling between the two gaseous phases and the mechanisms driving turbulence in these phases, and make predictions for the slope of the cold phase VSF, and its relationship to the hot phase counterpart. The paper is organized as follows. In Section 2 we present the simulation approach. The discussion of the results is presented in Section 3, and we conclude in Section 4.

4.4 Methods

We perform three-dimensional MHD simulations using the FLASH code (*Fryxell et al.*, 2000; *Dubey et al.*, 2008) using the directional unsplit staggered mesh MHD solver (*Lee*

name	magnetic field	$n_{\rm max}$	$\Delta x_{\rm min}$
LR-HD	no	6	0.244 kpc
LR-MHD	yes	6	0.244 kpc
FID-HD	no	7	0.122 kpc
FID-MHD	yes	7	0.122 kpc

Table 4.1: List of models

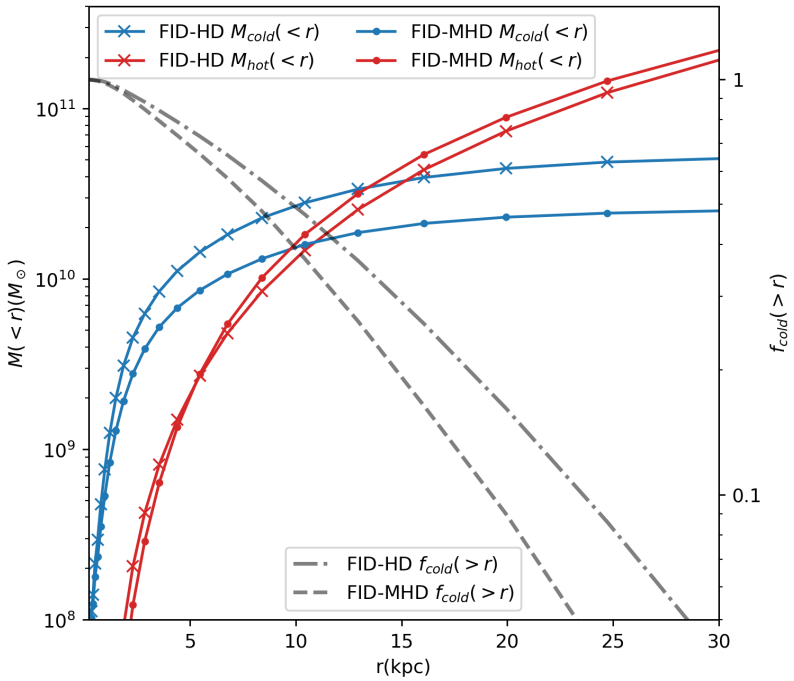

Figure 4.2: Blue and red lines: radial profile of enclosed mass ($M < (r)$) of hot and cold gas in FID-HD and FID-MHD cases. Grey lines: the profiles of cold gas fraction outside of a given radius ($f_{\rm cold}(> r)$). All profiles are averaged over $t = 0.4 \sim 1.5$ Gyr.

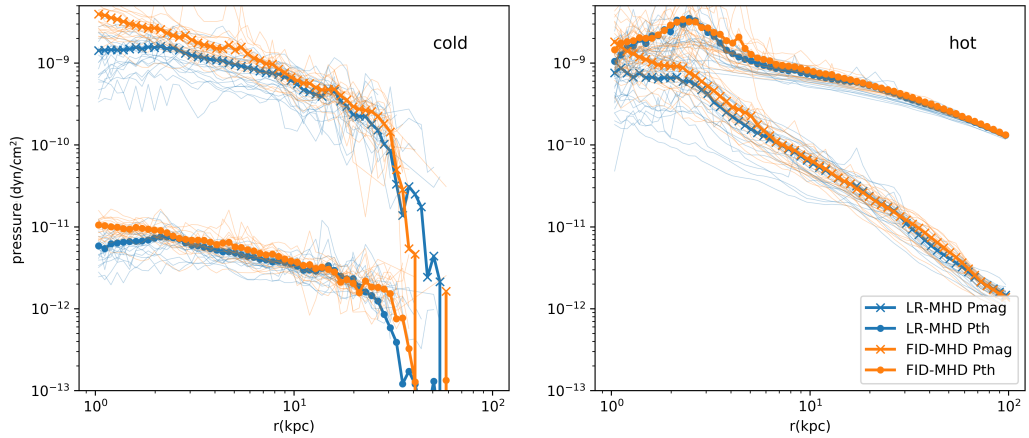

Figure 4.3: Left: radial profile of the magnetic pressure ("x"-labelled line) and thermal pressure (dot-labelled line) of the cold gas in the MHD runs. Right: same as on the left but for the hot gas.

and Deane, 2009; *Lee*, 2013). We adopt a simulation domain with statically-refined grids. Similar to *Wang et al.* (2020), the domain is refined by a set of nested cubic regions. The entire domain is a cubic region with width $L_{\rm box} = 1$ Mpc and 64^3 base grids. The central regions with width

$$L_n = L_{\rm box}/2^n \text{ kpc} \tag{4.1}$$

have n additional nested refinement levels. We include models with different $n_{\rm max}$, as listed in Table 4.4. The size of the smallest cell is $\Delta x_{\rm min} = L_{\rm box}/64/2^{n_{\rm max}}$. For the resolution study, we modify the width of the two most refined regions in the high resolution models, so that L_7 in the high resolution models equals $L_6 \approx 15.6$ kpc in the low resolution models. Therefore, in order to calculate the sizes of the regions at a given refinement level in the FID-HD and FID-MHD cases, we use eq. (4.1) for $n \leq 5$ and set $L_7 \approx 15.6$ kpc and choose L_6 such that it falls between L_5 and L_7 (our adopted value of L_6 is ≈ 23.4 kpc).

We use the diode boundary conditions, where all variables have zero gradient and gas can only flow out at the domain boundary.

4.4.1 Cluster initial conditions

We setup the initial conditions of the hot gaseous halo consistent with the Perseus cluster. For the temperature profile, we use an analytical fit based on the observed X-ray surface brightness distribution in the Perseus cluster (*Churazov et al.*, 2003):

$$T(r) = 7 \text{ keV} \frac{1 + (r_{\rm kpc}/71)^3}{2.3 + (r_{\rm kpc}/71)^3} [1 + (r_{\rm kpc}/380)^2]^{-0.23}. \tag{4.2}$$

We include a static gravitational field with contributions from a dark matter halo and stars. The dark matter potential is described by an NFW profile (*Navarro et al.*, 1996), with scale radius $r_s = 358.3$ kpc, virial radius $r_{\rm vir} = 2.44$ Mpc and virial mass $M_{\rm vir} = 8.5 \times 10^{14} M_\odot$. The gravitational acceleration due to stars is based on the analytic fit to the de Vaucouleurs profile (*Mathews et al.*, 2006):

$$g_{\rm star}(r) = \left[\frac{r_{\rm kpc}^{0.5378}}{2.853 \times 10^{-7}} + \frac{r_{\rm kpc}^{1.738}}{1.749 \times 10^{-6}} \right]^{-1.11} \text{ cm s}^{-2}. \tag{4.3}$$

Assuming hydrostatic equilibrium, we then calculate the density profile and normalize it to match the azimuthally averaged observed density profile (*Mathews et al.*, 2006).

Following *Ruszkowski et al.* (2007), we set up tangled magnetic fields with power spectrum $B_k \propto k^{-11/6} \exp(-k^4/k_0^4)$, where $k_0 = 100(2\pi/L_{\rm box})$. To obtain magnetic fields with this power spectrum and plasma $\beta \sim 100$, we first inversely Fourier transform the power spectrum to real space; then normalize the real space magnetic fields to have $\beta \sim 100$; Fourier transform the magnetic fields; clean the magnetic field divergence in Fourier space; and finally perform inverse Fourier transformation to obtain real space magnetic fields. We repeat this procedure until the magnetic fields become divergence free. For radiative cooling, we adopt the tabulated Sutherland-Dopita cooling function assuming one-third solar metallicity (*Sutherland and Dopita*, 1993).

4.4.2 AGN feedback

We use the cold accretion model to simulate the fueling of the AGN. The cold gas is accreted at a rate of $\dot{M}_{\rm acc} = M_{\rm acc}/5$ Myr, where $M_{\rm acc}$ is the total mass of the cold gas ($T < 10^5$ K) within the depletion region, $r < 1.2$ kpc. For each computational time step (Δt), $\dot{M}_{\rm acc}\Delta t$ of the cold gas is removed in the depletion region and loaded to the jet base. The gas in the jet base is then launched into the halo via bipolar jets along $z-$axis of the simulation domain. The jet base is a cylinder at the domain center with a radius of 1.25 kpc and a height of 4 kpc. The AGN jets may change direction as evidenced by the relative misalignment of the X-ray cavities observed in Perseus cluster. The orientation of the jets can change due to many reasons (*Babul et al.*, 2013), precession of the central supermassive black hole being one of them (*Dunn et al.*, 2006), and can explain the observed misalignment. The precession of the central supermassive black hole can happen when the spin axis of the black hole is misaligned with respect to its accretion disk; *Lodato and Pringle* (2006); *Martin et al.* (2007) have shown that the precession period of the black hole is comparable to or even a few times longer than the timescale over which the spin axis of the black hole re-aligns itself with the accretion disk due to viscosity. The precession timescale can be on the order of tens of Myr as shown by *Martin et al.* (2007). Therefore, we assume a period of 10 Myr. We also assume a jet precession angle of 15 degrees. The AGN feedback is purely kinetic with power $\dot{E}_k = \epsilon\eta\dot{M}_{\rm acc}c^2$, where $\epsilon = 10^{-3}$ is the feedback efficiency, $\eta = 1$ is the mass loading factor, and c is the speed of light.

4.5 Results

4.5.1 General characteristics of cold gas distribution and the evolution of the cluster

In all cases, the systems go through the self-regulated AGN feedback cycles. The development of thermal instabilities leads to cold gas condensation in the form of filaments. The cold gas forms a long-lived massive rotating disk during the long term evolution of the

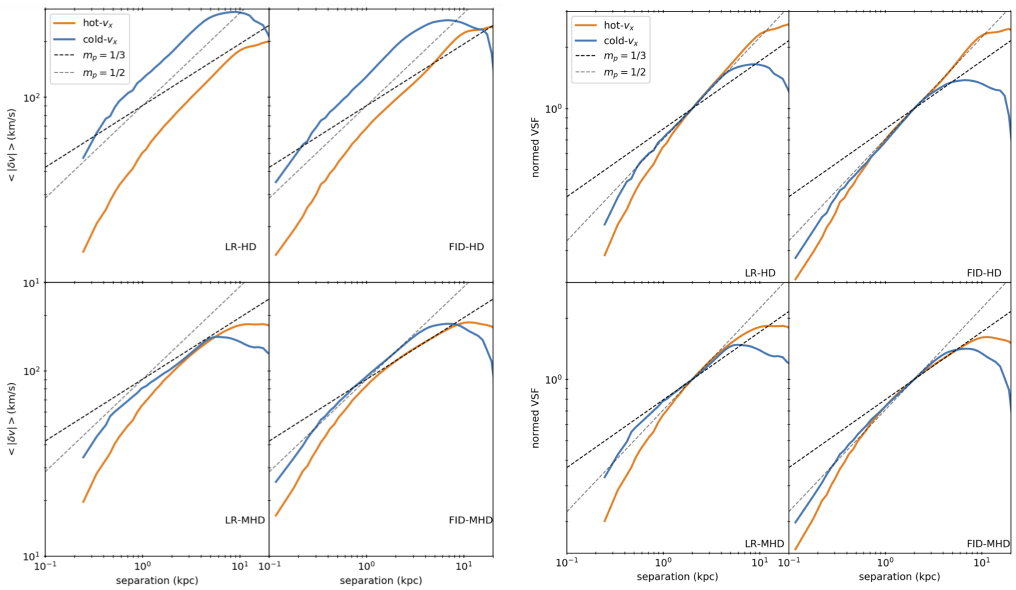

Figure 4.4: VSFs of hot (orange) and cold (blue) phase gas averaged over $t = 0.5 \sim 1$ Gyr of the four runs. The right four panels are the same as the left four except that they are normalized to 1 at the separation of 2 kpc. The black and grey dashed lines have slopes $m_p = m_{\rm kol} = 1/3$ and $m_p = 1/2$, respectively.

hydro cases, while the disk is absent in the MHD cases. The same phenomenon was found in *Wang et al.* (2020). As we argued there, the formation of such a disk is unphysical and in tension with observations. The magnetic tension force can effectively decelerate the cold gas. Therefore the magnetic fields redistribute the angular momentum of the cold gas, and prevents disk formation.

Snapshots of the projected gas density are shown in Fig. 4.1 in the FID-HD and FID-MHD case (left and right panel, respectively). There are clear morphological differences between these two cases. While in the hydro case, the dense and cold gas exists in the form of blobs and filaments, in the MHD case the dense gas structures are noticeably more filamentary. In both cases the filaments tend to be biased in the radial direction. The cold filaments are more spatially confined to the cluster center in the MHD cases than those in hydro cases (Fig. 4.1).

In the FID-MHD runs 95% of the cold gas mass is contained within $r \lesssim 25$ kpc, while for FID-HD, this happens within $r \lesssim 30$ kpc (grey lines in Fig. 4.2; hereafter cold gas is defined

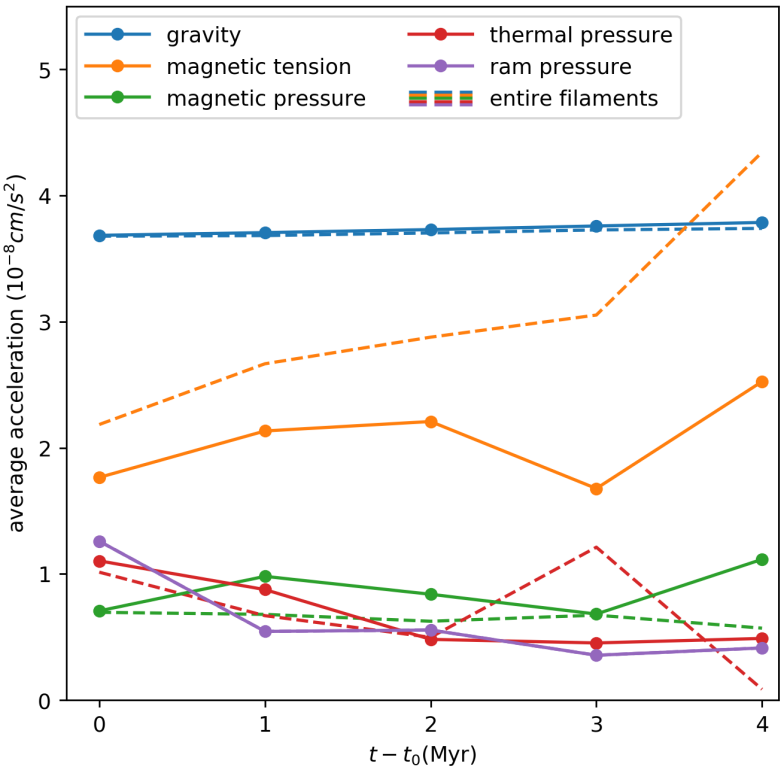

Figure 4.5: Values of accelerations contributed by different sources during the infall process of a cold filament. The solid lines show the values averaged over the head of the filament and the dashed lines are over the entire filament.

as having $T < 2 \times 10^4$K and $\rho > 10^{-24}$g cm^{-3}, and hot gas as having 10^7K $< T < 10^8$K). When the system is active, the typical mass of the cold gas is $10^{10} \sim 5 \times 10^{10} M_\odot$, which is broadly consistent with the high end of the molecular gas mass observed in galaxy clusters (e.g., *Vantyghem et al.*, 2018; *Olivares et al.*, 2019). This is especially so given that our definition of the cold gas includes the molecular gas as well as the gas at higher temperatures. We also note that, as evidenced in Fig. 4.2, the time averaged amount of cold gas is smaller in the FID-MHD cases compared to the FID-HD case.

For all four runs, the typical one-dimensional velocity dispersion of the hot gas during the AGN active phase in the 30 kpc $< r <$ 60 kpc region is $\sim$ 100 km s^{-1}, which is consistent with other hydrodynamic simulations (*Prasad et al.*, 2018) but underestimates the Hitomi observation (*Hitomi Collaboration et al.*, 2016). In the $r <$ 10 kpc region, the dispersion is $\sim$ 200 km s^{-1}. Our results thus suggest that AGN-related activities may be the dominated driver of turbulence in the ICM center, but can not account for the turbulence observed in the outer region of the ICM halo, where large-scale motions such as cosmic accretion and mergers may be the major contributor (*Ruszkowski et al.*, 2011; *Lau et al.*, 2017; *Bourne et al.*, 2019) with possibly important contributions from orbiting substructures (*Bourne and Sijacki*, 2017) and magnetic tension forces resulting from MHD turbulence (*Ehlert et al.*, 2021).

In the left panel of Fig. 4.3 we show radial profiles of the magnetic pressure ("x"-labelled line) and thermal pressure (dot-labelled line) of the cold gas in the MHD runs. The right panel shows the profiles of the same quantities but for the hot gas. In the $r <$ 10 kpc region, the average plasma β reduces to $\sim$ 10 from the initial value of $\sim$ 100. With $\beta \sim 10$, there is an energy equal partition between kinetic energy and magnetic energy in the hot halo. Therefore, the magnetic fields are globally amplified by turbulent stirring in the hot halo and lose memory of the initial conditions. It is clear from this figure that the pressure support of the cold filaments is dominated by the magnetic pressure. The magnetic pressure of the cold filaments is in balance with the thermal pressure of the ambient hot gas,

which is evident from comparing top orange line in the left panel (representing magnetic pressure) with the top orange line in the right line (representing thermal pressure) – both of these curves have very similar values in the central ∼20 kpc. This result is in agreement with the optical emission line observations of Perseus cluster (*Fabian et al.*, 2008) and numerical simulations (*Sharma et al.*, 2010). Furthermore, the low plasma β filaments are consistent with the models suggesting that the Hα emission of the cold filaments is powered by magnetic reconnection (*Churazov et al.*, 2013) or cosmic rays (*Ruszkowski et al.*, 2018).

4.5.2 Velocity structure function

Throughout this paper, we use the first order VSF of the $x-$component to study the properties of the ICM turbulence. It is defined as VSF(l)$\equiv \langle |v_x(\mathbf{r}+\mathbf{l}) - v_x(\mathbf{r})| \rangle$, where v_x, $\mathbf{r}$ and $\mathbf{l}$ are the $x-$component of the gas velocity, position vector and the vector connecting a pair of points, respectively, and the averaging is performed over pairs of points with the same separation $l = |\mathbf{l}|$. We note that the y-component VSF shows qualitatively the same results due to the axisymmetry about the jet launching $z-$axis. We denote the slope of the VSF as m_p, i.e., VSF(l) $\propto l^{m_p}$. For all the VSFs calculated in this paper, we only use the data in the region with the highest refinement level. This approximately corresponds to the central $r < 10$ kpc region for all runs. Thus we ensure a uniform sampling of the velocity fields without interpolations. In this paper, we focus on three-dimensional VSF and on how the physics included in the simulations affects the VSF slope. Thus, our results can be compared to the prediction from the Kolmogorov theory in a straightforward fashion.

4.5.2.1 Velocity structure function of the precipitating cold gas

Figure 4.4 shows the first order VSFs averaged over the AGN active phase ($t = 0.5 \sim$ 1 Gyr). The right four panels are the same as the left four except that they are normalized to 1 at the separation of 2 kpc. We include the normalized version in order to make it easier to compare the VSF slopes. One of our key results is that the averaged VSF of cold

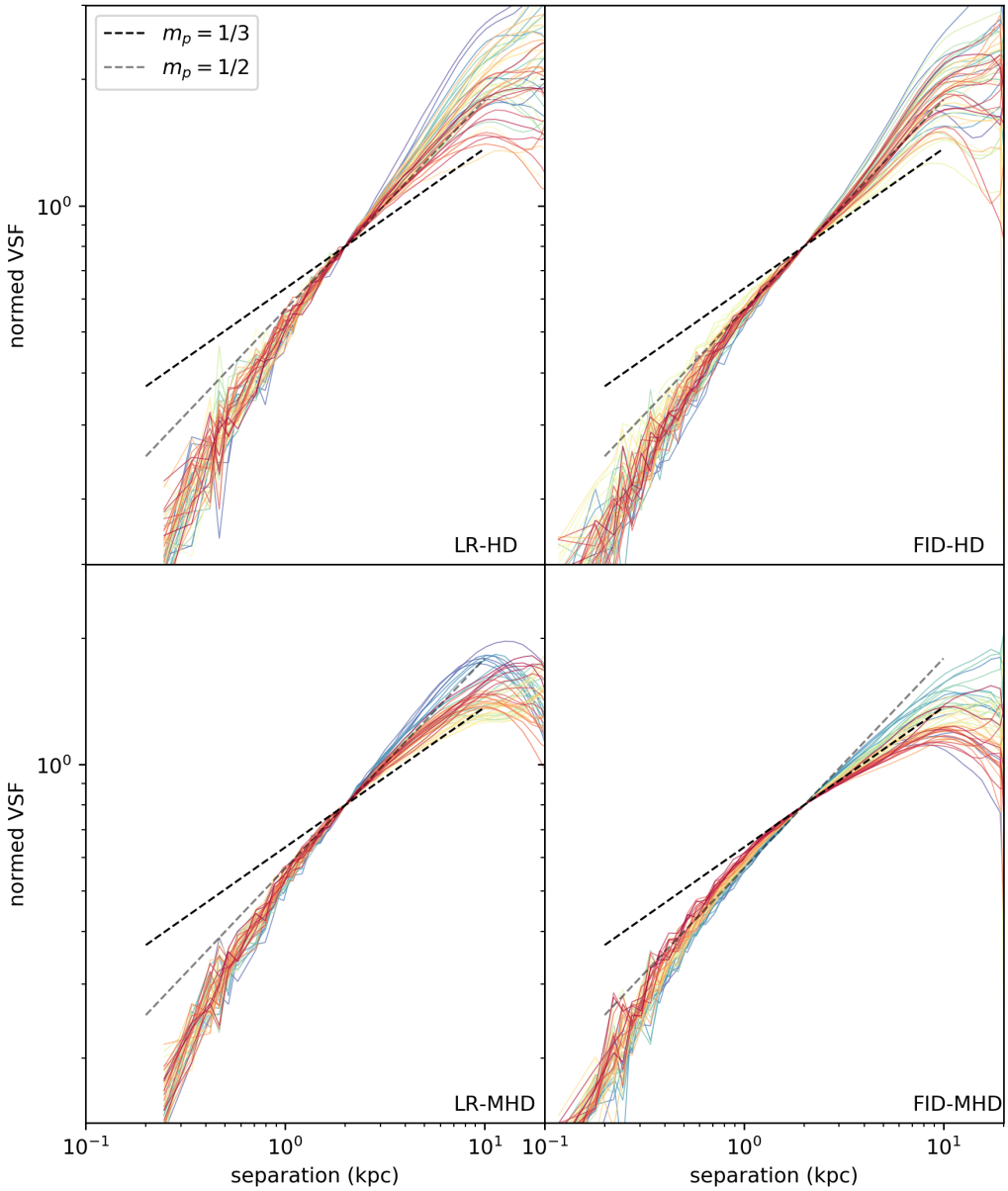

Figure 4.6: Hot phase VSFs plotted every 10 Myr for $t = 0.5 \sim 1$ Gyr in four runs. Time is denoted by the color, changing from purple to red.

filaments ($T < 2 \times 10^4$K, $\rho > 10^{-24}$g cm^{-3}) has a slope steeper than that predicted from the Kolmogorov turbulence, $m_{\rm kol} = 1/3$. In the hydro cases, the slope is $m_p \approx 1/2$; and in the MHD cases, the slope is either close to $1/2$ or slightly shallower. Comparisons of blue curves in the LR-HD and FID-HD cases (top row), and of the blue curves in the LR-MHD and FID-MHD cases (bottom row), demonstrate the slopes of the cold phase VSF are numerically convergent in the inertial range ($2 \sim 4$ kpc in low-resolution and $0.8 \sim 3$ kpc in fiducial cases).

In order to understand the nature of this scaling of the velocity with cloud separation, we inspect the acceleration terms in the Euler equation for an isolated cold filament. According to the momentum equation, the average acceleration acting on the filament can be decomposed into: gravity (a_g), magnetic tension (a_t), thermal pressure gradient (a_p), magnetic pressure gradient (a_m), and the ram pressure ($a_{\rm rp}$). The accelerations are calculated from:

$$\mathbf{a}_g = \frac{1}{M}\int \rho \mathbf{g} \mathrm{d}V \tag{4.4}$$

$$\mathbf{a}_t = \frac{1}{M}\int \rho \nabla \cdot \left(\frac{\mathbf{BB}}{4\pi}\right) \mathrm{d}V \tag{4.5}$$

$$\mathbf{a}_p = -\frac{1}{M}\int \nabla p_{\rm th} \mathrm{d}V \tag{4.6}$$

$$\mathbf{a}_m = -\frac{1}{M}\int \nabla p_{\rm mag} \mathrm{d}V, \tag{4.7}$$

$$\mathbf{a}_{\rm rp} = -\frac{1}{M}\rho_{\rm ICM} v_{\rm com}^2 \mathbf{S}, \tag{4.8}$$

where the integral is over the filament; ρ is the gas density; $\mathbf{g}$ is the gravitational acceleration; $\mathbf{B}$ is the magnetic field strength; $M = \int \rho \mathrm{d}V$ is the total mass of the filament; $p_{\rm th}$ is the thermal pressure; $p_{\rm mag}$ is the magnetic pressure; $\rho_{\rm ICM}$ is the density of ambient ICM; $v_{\rm com}$ is the center of mass velocity of the filament; and $\mathbf{S}$ is the surface area of the cross section normal to $v_{\rm com}$ of the filament. We estimate $\rho_{\rm ICM} = 2 \times 10^{-25}$g cm^{-3}. As the filament falls towards the halo center, it is elongated due to the deceleration from magnetic

tension force and forms a tail behind the head of the filament. The magnitudes of all the acceleration vectors are shown in Fig. 4.5. The solid lines are the accelerations averaged over the the head of the filament and the dashed lines are over the entire filament (note that selecting the entire filament or just its head has little effect on $a_{\rm rp}$; filament head is defined as the location in the filament closest to the cluster center). This analysis shows that when magnetic fields are absent, the motion of the cold filament is dominated by the gravitational force. Gravitational acceleration close to the cluster center is nearly constant. The velocity v of the cold filaments subject to constant gravitational acceleration, g, scales with travel length L as $v \propto (gL)^{1/2}$, which leads to the $m_p \approx 1/2$ slope of the VSF in the hydro runs. We verify this hypothesis by performing a simple experiment where we calculate the VSF of multiple 1D velocity-position pairs sampled from a free-fall trajectory (see Appendix B for details). When magnetic fields are included, the sub-dominant magnetic tension force increases as the filaments fall, which effectively makes the filaments gain less velocity for the same travel length compared with the hydro case. Therefore, $m_p < 1/2$ for cold phase in the MHD cases.

4.5.2.2 Velocity structure function of the hot ICM

The hot phase discussed hereafter has the temperature in the range $10^7\mathrm{K} < T < 10^8$ K and excludes the gas component directly entrained by the bipolar jets. We define the entrained gas as that with fast outflow velocity along the jet launching axis, i.e., $\mathrm{sign}(z)v_z > 500$ km/s, where v_z is the gas velocity along $z-$axis.

In general, the turbulence in the hot ICM is volume filling. We estimate the degree of volume filling following *Iapichino and Niemeyer* (2008), where the volume filling factor (f_V) is defined as the fraction of the volume of the gas that has vorticity magnitude larger than the mass-weighted average vorticity. We find $f_V \sim 0.4$ for hot gas in both FID-HD and FID-MHD runs, indicating moderately volume filling turbulence.

In the hydro cases, when the system is active (i.e., when the AGN jet is switched on and

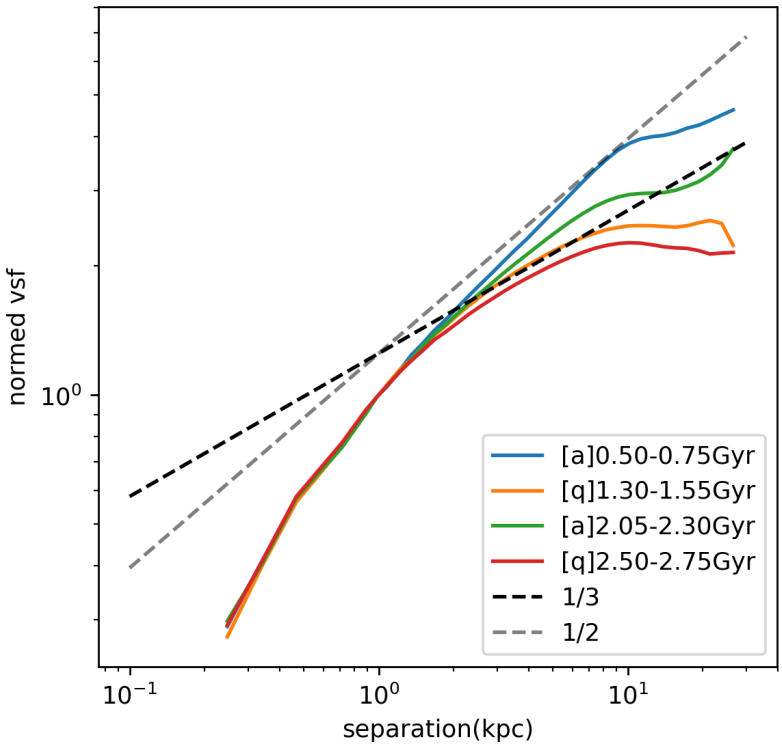

Figure 4.7: ’
’) or quiescent (“[q]”) epoch and the corresponding time range in the legend.]Normalized VSF of the hot gas averaged over quiescent and active epochs in the LR-HD case. Each VSF is labelled with active (“[a]”) or quiescent (“[q]”) epoch and the corresponding time range in the legend.

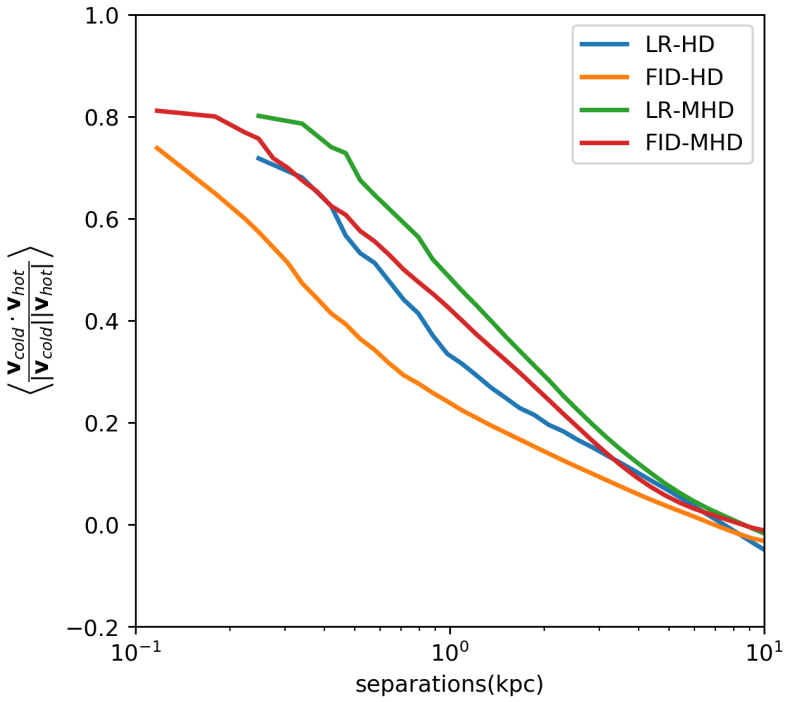

Figure 4.8: Average spatial correlation of the cold and hot velocity normalized by the velocity magnitude.

cold gas precipitation is present), the slope of the hot phase VSF scatters around $m_p = 1/2$. This can be seen in Fig. 4.6, which shows the hot phase VSFs during the active phases (for the hydro cases, see top two panels in this figure) and the average VSF has the same slope as that of the cold phase in the inertial range (top two panels of Fig. 4.4). This result is numerically convergent and is consistent with the possibility that it is the cold filaments that predominantly drive turbulence in hot gas (see also Section 4.5.3 below). Note that the steep slope of hot phase VSF is not likely caused by the superposition of turbulence with multiple injection scales. *Yoo and Cho* (2014) perform turbulent simulations adopting multiple injection scales by design, and find that the kinetic energy power spectra show spiky features in the injection scales range and the spectra in the inertial range are still Kolmogorov-like. The hot VSFs in our simulations do not have these features. In the quiescent phase, the hot VSF flattens towards $m_{\rm kol}$ on large scales (Fig. 4.7). We note that the same steepening/flattening trends in the active/quiescent phases are also present in the

MHD cases, which we do not show in this figure in the interest of brevity.

In the MHD cases, when system is in the active phase, the hot phase VSFs have slopes scattering around $m_p = 1/2$ in LR-MHD case, while in the FID-MHD case, the VSFs are systematically shallower and the slopes are scattered between $m_p \lesssim 1/3$ to $m_p \approx 1/2$ (two bottom panels in Fig. 4.6). Although not numerically convergent, in both MHD cases the hot phase slopes m_p are generally distributed above 1/3 predicted from Kolmogorov theory. In Appendix A we verify via a simple controlled experiment that the expected slope of the hot phase VSF is indeed 1/3 and we assess at what minimum separations the numerical effects become important. In this experiment, we find the Kolmogorov-like VSFs steepen at sub-kpc scales due to numerical dissipation, which explains the same steepening in the hot VSFs of full physics runs (Fig. 4.4). Note that cold-phase VSFs are less affected by the numerical steepening at small scales. This is because gravity dominates the motion of cold filaments (Fig. 4.5); and gravity is insensitive to numerical resolution. This is consistent with the fact that the slope of cold phase VSF is numerically convergent in both hydro and MHD cases. In general, in full physics simulations, the slopes of the hot phase VSF in the MHD cases are shallower than 1/2. There appears to be tentative evidence for the flattening of the hot phase VSF in the MHD case toward the 1/3 slope expected in the Kolmogorov case. However, we note that we cannot make definite statement about the slope of the hot phase VSF due to relatively narrow inertial range and limited numerical resolution. We further discuss the driving of the hot phase turbulence in Section 4.5.3.

As mentioned above, here we focus on three-dimensional VSF and the physics shaping the VSF slope. This allows us to *directly* compare simulation results to the prediction from the Kolmogorov theory. In order to make detailed comparisons to the observations of the VSF of the cold and hot phases of the ICM, one needs to perform careful projections on to the plane of the sky. As far as the hot phase VSF is concerned, *ZuHone et al.* (2016) demonstrate that, while the projected and three-dimensional velocity power spectra have the same slope, the second order three dimensional VSF has a steeper slope than 2/3 predicted

from Kolmogorov's theory. Thus, we expect that the first order projected hot phase VSF could also have a steeper slope than its Kolmogorov's counterpart. Although the hot gas power spectra from X-ray observations can be corrected for the projection effect, there are difficulties with doing direct comparison between our results and the current X-ray observations. First, the X-ray analyses of power spectra (e.g., *Zhuravleva et al.*, 2014) do not cover the $r \lesssim 10$ kpc region of the ICM halo, where the VSFs in our simulations are calculated. Second, observed turbulence in the hot phase is derived from the density fluctuations by assuming an isobaric equation of state and no other sources of density fluctuations. However, tangential discontinuities (including but not limited to bubble-ICM discontinuities or cold fronts) can source density fluctuations but without contributing to velocity fluctuations, thus causing bias in the turbulence derivation. For the cold phase, the projected slope may be shallower than the slope of the three-dimensional VSF (*Li et al.*, 2020). The relationship between the two- and three- dimensional slope may be further complicated in this case by the fact that many filaments may be seen along the same line of sight. Maps of the distribution of the cold filaments on the sky used to compute the VSF by *Li et al.* (2020) suggest that the covering factor may exceed unity. It is for these reasons that we defer the projection analysis to future work and in this paper we instead focus on the physics of the three dimensional VSF and comparisons to the prediction from the Kolmogorov theory.

4.5.3 The driving sources of turbulence in the hot ICM

We now consider two turbulence driving mechanisms that operate in the hot phase and discuss their relative importance depending on the physics included in the simulations. Note that there are other possible driving sources of turbulence in the ICM, such as cosmological mergers (*Lau et al.*, 2017; *Bourne et al.*, 2019), orbiting substructures (*Bourne and Sijacki*, 2017), penetrating gas streams (*Zinger et al.*, 2016), gas sloshing (*ZuHone et al.*, 2018), and magnetic tension forces resulting from MHD turbulence driven by any of the effects above

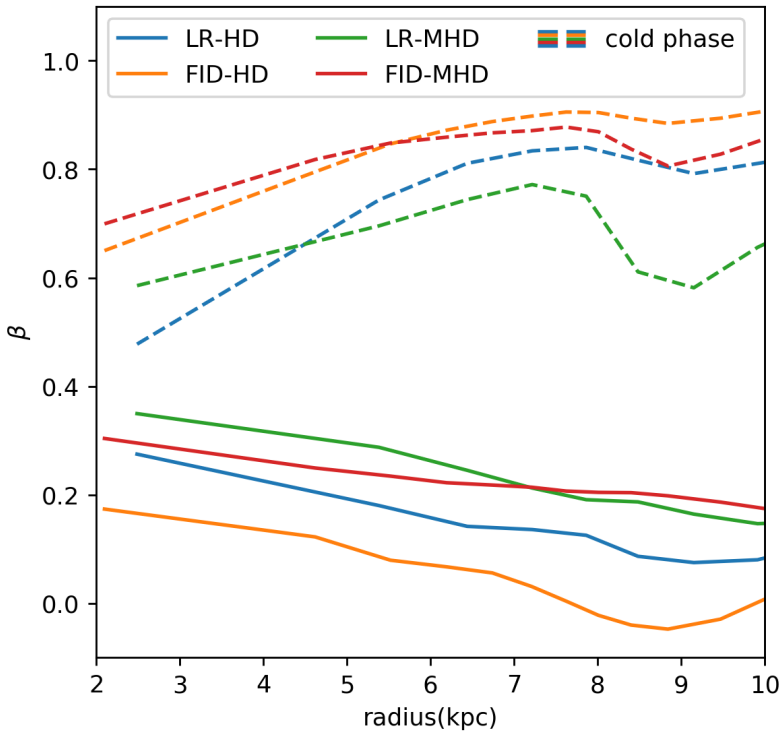

Figure 4.9: Average radial profile of the anisotropy parameter (β) of the hot gas in all runs. β of the cold gas is shown as dashed lines. Positive values of β correspond to radial bias in the velocity distribution.

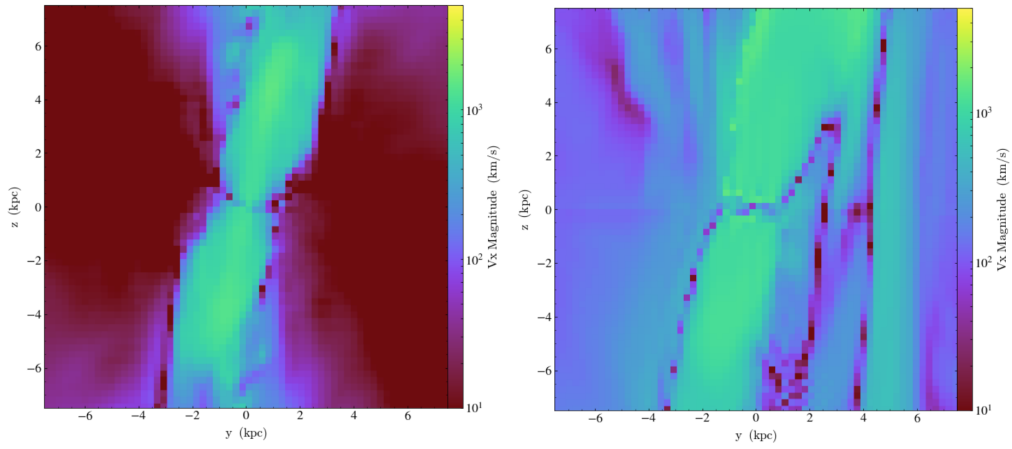

Figure 4.10: Snapshots of the slice plot of $|v_x|$ in the test simulations with AGN manually turned-on. Left panel is for the test run with the same initial conditions as in the LR-HD run and the right panel corresponds to the same initial conditions as in the LR-MHD run.

(*Ehlert et al.*, 2021). However, these sources should be less important in the central region of the ICM considered here.

4.5.3.1 Turbulence driving by cold filaments

It is conceivable that cold filaments stir the ambient hot gas and generate turbulence. The arguments in favor of this hypothesis are the following:

(a) The cold phase mass has a dominant contribution to the mass budget in the inner core of ICM. Specifically, as shown by the blue and red lines in Fig. 4.2, the cold gas mass exceeds the hot gas mass for radii $r < 10$ kpc in the FID cases, and we see smaller amounts of cold gas in the FID-MHD case compared to the FID-HD case. Using Chandra observations, *Babyk et al.* (2019) show that the ratio of molecular gas to atmospheric gas within a 10 kpc radius lies between 3% and 50% for central galaxies in clusters. As mentioned above, our definition of the cold gas includes the molecular gas and the gas at higher temperatures, so the cold gas portion in our simulations may be broadly consistent with the observations. Thus, in the inner region, the cold filaments have sufficient momentum and may be capable of driving the motion of the hot phase.

(b) Hot and cold gas velocities are spatially correlated. The spatial correlation is defined as: $f_{\rm ch}(r) = \langle \mathbf{v}_{\rm hot}(\mathbf{x}) \cdot \mathbf{v}_{\rm cold}(\mathbf{x}+\mathbf{r}) \rangle_{\mathbf{x}}$, where $r = |\mathbf{r}|$. This quantity is positive and increases with decreasing spatial separation (Fig. 4.8), indicating that the velocities of the cold and hot gas parcels are more aligned when they are closer. Thus, the motions of cold filaments and hot gas are *coupled*.

(c) In the hydro cases, when the system is in the active phase, the slope of hot phase VSF is $m_p \sim 1/2$, which is the same as the average VSF slope of the cold gas in the inertial range.

(d) The distributions of the hot and cold gas velocities are radially-biased. The anisotropy

parameter is defined as: $\beta = 1 - \sigma^2_{\rm tan}/2\sigma^2_{\rm rad}$ (not to be confused with plasma β parameter), where $\sigma^2_{\rm tan} = \sigma^2_\theta + \sigma^2_\phi$. The motion of the cold filaments is highly radial due to the radial gravity and launching of the thermally unstable blobs by the AGN jets. The motion of the hot gas is also radial ($\beta > 0$; Fig. 4.9). This is so despite the fact that the hot gas entrained by the AGN jets is filtered out in the process of computing β. This implies coupling between the radially-biased cold filaments and hot phase. This conclusion is further strengthened by noting that in the process of decay of hot phase turbulence, the tangential motions should be progressively more important than the radial motions (e.g., *Ruszkowski and Oh*, 2010) due to buoyant restoring forces. So the fact the hot gas motions are nevertheless radially-biased suggests that they may be driven by the cold gas.

We note that the radial bias in the velocity distribution of the hot phase is unlikely to be caused by anisotropy in the radial hot gas accretion or the "gentle circulation" described in *Yang and Reynolds* (2016). As explained below, the inflow velocities due to these two mechanisms are both much smaller than the values of the hot gas VSF (except at very small separations).

The average AGN cold mass accretion rates over the first Gyr of all runs are in the range $40 \sim 70\ M_\odot\ {\rm yr}^{-1}$. The estimated hot mode accretion rate is $\dot{M} \lesssim 1\ M_\odot\ {\rm yr}^{-1}$ as it is expected to be ~2 orders of magnitude smaller than that of the cold mode (*Gaspari et al.*, 2013). This accretion rate corresponds to an inflow velocity $v_{\rm in,hot} \sim \dot{M}/4\pi r^2 \rho_{\rm ICM}$. For $r = 10$ kpc and $\rho_{\rm ICM} \approx 10^{-25}$g cm^{-3}, the inflow velocity is only $v_{\rm in,hot} \lesssim 0.6$ km s^{-1}.

The ambient gas outside of the jet cone can form a reduced cooling flow (*Yang and Reynolds*, 2016). Assuming this inflow replenishes the gas mass in the central region lost to the bipolar outflow, the inflow velocity ($v_{\rm in,circ}$) can be estimated from:

$$v_{\rm in,circ} = \frac{2\Omega}{4\pi - 2\Omega}\frac{\rho_{\rm jet}}{\rho_{\rm ICM}} v_{\rm jet}, \tag{4.9}$$

where Ω is the solid angle subtended by the jet cone; $\rho_{\rm jet}$ and $\rho_{\rm ICM}$ are the gas density of jet and ambient ICM respectively; and $v_{\rm jet}$ is the jet velocity. Estimating right hand side quantities at $r \approx 10$ kpc to be $\Omega \approx 0.2$ (for jet cone apex angle equals to 30 degree), $\rho_{\rm jet}/\rho_{\rm ICM} \approx 0.1$, and $v_{\rm jet} \lesssim 5000$ km s^{-1}, the estimated inflow velocity is only $v_{\rm in,circ} \lesssim 17$ km s^{-1}.

4.5.3.2 Turbulence driving by AGN

AGN jets can be an important source of turbulence in the hot phase. In order to disentangle the contributions of AGN and cold filaments to hot phase VSF, we perform four test simulations with the same initial conditions as the four full physics simulations, but excluding radiative cooling and enforcing constant AGN jet power. The constant AGN power is chosen to be consistent with the average AGN power in the production runs within the first 1 Gyr. We note that all four full physics simulations inject almost identical amount of energy during this time interval, which simplifies the interpretation of the results.

These test simulations demonstrate that the AGN jets effectively transfer momentum to the hot ambient gas (i.e., the hot gas outside of the jet cone) when the magnetic fields are present. Specifically, Fig. 4.10 shows the slice plots of $|v_x|$ for the test simulations. It is clear from this figure that the ambient gas moves much faster in the MHD case compared to the hydro case. This implies that the magnetic fields in the center of the cluster facilitate the momentum transfer from the jets to the ambient region.

Figure 4.11 shows the averaged VSF of hot phase gas in the production runs and those in the corresponding test runs. In this figure we consider LR-HD and LR-MHD cases as we evolved them for the longest time. However, we also note that FID-HD and FID-MHD evolved up to ~0.6 Gyr were convergent when compared to their lower resolution counterparts both in terms of the normalization and slope of the VSF. In the hydro cases, the motion induced by the AGN only is subdominant (orange dotted lines in the left panel), so it is likely that the hot phase motion is mainly driven by cold filaments in this case. In the

MHD cases, the VSF contribution from the AGN only (orange dotted line in the right panel) is comparable to that due to the combination of the filaments and AGN in the full physics case, indicating that the motion driver of the hot gas could be a mixture of the AGN jet and cold filament stirring. This is likely due to better coupling of the jets with the ambient medium facilitated by the presence of the magnetic fields. Additionally, this picture is further supported by comparing the normalization of the hot and cold VSF (left four panels of Fig. 4.4). In the hydro cases, the cold phase VSF has higher velocity normalization than the hot phase VSF on all scales, so the massive cold filaments with high velocity may be sufficiently energetic to drive turbulence in the hot phase. In the MHD cases, at large scale the hot VSF has higher normalization than the cold VSF, indicating the turbulence in hot phase must be driven by other means.

We note that our manual jet case scenario is similar to the one considered by *Hillel and Soker* (2020). In their simulations, the hot phase VSF slope is 1/2, i.e., steeper than Kolmogorov, which is what we also find in our case in general. Since their simulations are too short for the local thermal instability to trigger the formation of precipitating clouds, and they neglect magnetic fields, the efficient stirring of the ICM in their case was likely facilitated by considering wide jet opening angle (half opening angle = 70 degrees) to better couple the jet to the ambient medium. In our case, direct stirring of the ICM by the jet is less efficient because the jet is narrow and the precession angle is only 15 degrees. Alternatively, jet intermittency considered by *Hillel and Soker* (2020) could also contribute to the differences in the efficiency of the coupling of the jet energy to the ICM (perhaps even while enforcing the same average jet luminosity), though we note that more bursty AGN activity is more efficient in generating sound waves than gentler AGN activity (*Bambic and Reynolds*, 2019).

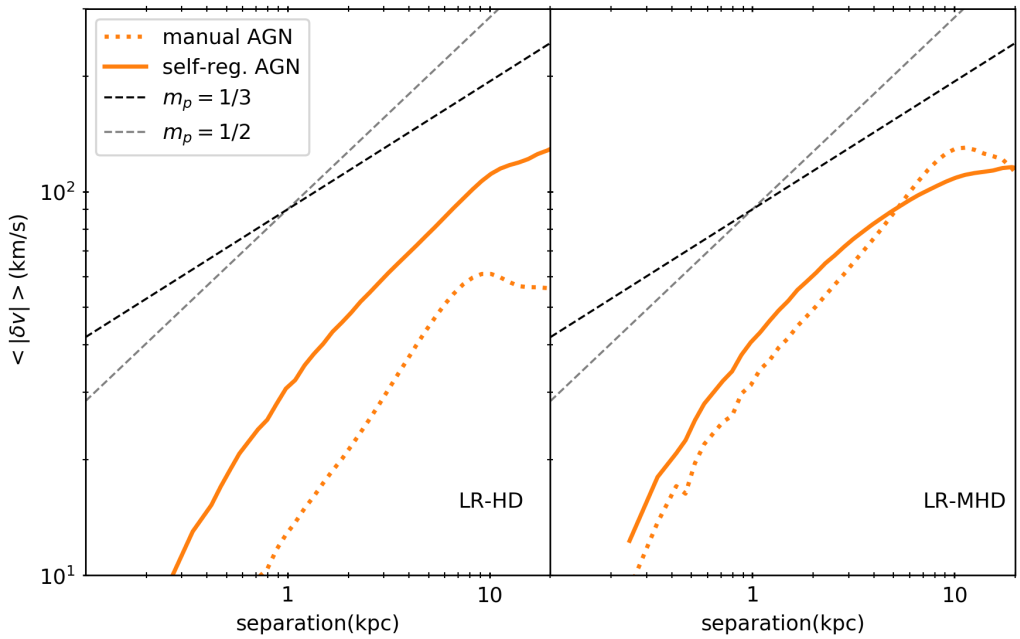

Figure 4.11: Averaged VSF of the hot gas in self-regulated AGN simulations (solid lines) and in the corresponding test simulations with manually turned-on AGN (dot line). The VSFs are averaged over $t = 0$ to 1 Gyr.

4.6 Summary

We perform 3D MHD simulations to study the properties of turbulence in the multiphase ICM affected by self-regulated AGN feedback. We find that, in general, the first-order velocity structure function of the multi-phase ICM is steeper than the slope predicted from Kolmogorov's theory ($m_p > 1/3$). Specifically we show that,

- the turbulent motions of the cold gas are primarily driven by the gravitational acceleration. This leads to the cold phase VSF slope close to $1/2$. When magnetic fields are included, the magnetic tension decelerates the cold gas and the VSF slope is either close to 1/2 or slightly shallower.

- Without the influence of magnetic fields, the precipitating cold filaments are likely the dominant driving source of the turbulence in the ambient hot ICM. The arguments in favor of this hypothesis are: i) in the central region of the gaseous halo, cold filaments have sufficient momentum to drive motions in the ambient hot gas; (ii) velocities of

hot and cold phases are spatially correlated; (iii) in the absence of magnetic fields, the slope of hot gas VSF during AGN active phase is steeper than 1/3 and matches that of the cold phase; (iv) both hot and cold phase velocities are radially biased.

- When magnetic fields are included, turbulence in the hot phase may be driven by a combination of AGN jet stirring and filament motion. This is because the magnetic fields facilitate the AGN driving by enhanced coupling between jet-like outflow and the ambient hot gas.

- We find tentative evidence for the flattening of the hot phase VSF in the MHD case (see Fig. 4.6). However, in this case, we cannot draw definite conclusions on the slope of the hot phase VSF due to narrower inertial range and lack of numerical convergence.

CHAPTER V

Turbulent Dissipation and Mixing in the Intracluster Medium

5.1 Preface

This chapter presents original results that are still in preparation. While I led this investigation, the results presented here were obtained in collaboration with Mateusz Ruszkowski and Peng Oh. I intend to submit an extension of the results presented here for publication in the Monthly Notices of the Royal Astronomical Society.

5.2 Introduction

Although it has been widely accepted that AGN feedback provides the energy needed to balance radiative cooling in the center of cool core clusters, how exactly this energy is coupled with the ICM is not well understood. Turbulence may play a role in delivering the energy to the ambient gas. By measuring the X-ray surface brightness fluctuation of the ICM, *Zhuravleva et al.* (2014) derive the turbulent dissipation rate in the ICM of the Perseus cluster and find that the heating rate due to turbulence dissipation can balance the radiative cooling rate. Their results suggest that turbulent dissipation is the key mechanism in solving the cooling flow problem.

However, the effect of turbulent mixing may change this picture. Due to the positive radial entropy gradient in the ICM, the random displacement of gas caused by turbulence generates inward thermal energy flux and effectively heats the inner ICM. Therefore, assessing the relative importance of turbulent mixing and turbulent dissipation in heating the ICM is vital for improving our understanding of the balance of heating and radiative cooling in hot gaseous halos.

In this work, I investigate the heating rate due to turbulent mixing and dissipation in cluster environments using numerical simulations. The objective is to understand the turbulent mixing in the framework of the mixing length theory (*Kim and Narayan*, 2003) and search the parameter space of the ICM properties for possible conditions, where the heating due to turbulent mixing is more important than that due to turbulent dissipation.

The level of gravitational stratification can be quantified by specifying the Froude number

$$Fr = \frac{u_{\rm rms}}{\omega_{\rm BV} l_{\rm drive}}, \tag{5.1}$$

where $\omega_{\rm BV} = \sqrt{\frac{g}{\gamma}\left(\frac{\partial \ln P}{\partial r} - \gamma \frac{\partial \ln \rho}{\partial r}\right)}$ is the Brunt–Väisälä frequency, $\gamma = 5/3$ is the adiabatic index, ρ is the gas density, P is the gas pressure, and g is the gravitational acceleration. It has been shown in the literature that strong gravitational stratification, which corresponds to small Froude number, can have a significant impact on turbulent dissipation (*Pouquet et al.*, 2018) and turbulent mixing (*Weinstock*, 1981). The analytical models presented in these works depend on the parameters that are calibrated from numerical simulations. However, these simulations are not tailored to the conditions of galaxy clusters. Thus, my work aims to calibrate these parameters and present a set of analytical formulae describing turbulent dissipation and mixing heating rates in the regimes appropriate for gaseous halos. These formulae can find many applications in future studies of the evolution of hot gaseous halos of galaxy clusters and ellipticals.

5.3 Methodology

I perform three-dimensional hydrodynamic simulations using the FLASH code (*Fryxell et al.*, 2000; *Dubey et al.*, 2008). The simulation domain is a 500 kpc-wide cubic box uniformly resolved by a 320^3 grid and the resolution is $\Delta x \approx 1.6$ kpc. The gaseous halo is continuously perturbed as the simulation proceeds. Turbulence is driven using the FLASH StirTurb module. This module applies a spectral forcing scheme utilizing an Ornstein-Uhlenbeck random process to accelerate the gas.

I performed four simulations. The three runs IB-SL03, IB-SL05, IB-SL08 listed in the order of increasing entropy gradient, have power-law entropy profiles, isobaric initial conditions, and no gravity. The run named PER-HSE has initial conditions modeled on the Perseus cluster and the gas is initially in hydrostatic equilibrium.

I set the power spectrum of the forcing scheme to be a top-hat function with very narrow width in the module of the wavevector k and centered on the scale of 20 kpc. Thus, the generated turbulence has approximately a driving scale of $l_{\rm drive} = 20$ kpc. The resulting turbulent velocity field has a Kolmogorov-like power spectrum, namely, $P(k) \propto k^{-5/3}$, where $P(k)$ is the turbulent kinetic energy power spectrum. The spectrum has cut-offs at $k_{\rm max} = 2$ kpc^{-1} and $k_{\rm min} = 0.3$ kpc^{-1} that correspond to the driving scale ($l_{\rm drive} \approx 2\pi/k_{\rm min}$) and the shortest wavelength that can be resolved, i.e., $2\Delta x \approx 2\pi/k_{\rm max}$, according to the Nyquist sampling theorem. These cut-off scales determine the coherence length $l_{\rm coh}$ of turbulence

$$l_{\rm coh} = \pi \frac{\int_{k_{\rm min}}^{k_{\rm max}} P(k)/k \mathrm{d}k}{\int_{k_{\rm min}}^{k_{\rm max}} P(k) \mathrm{d}k} \approx 5.5 \text{ kpc}. \tag{5.2}$$

5.3.1 An analytic model for the heating rate due to turbulent mixing

In mixing length theory, the heating due to turbulent mixing is described in terms of the convective energy flux (*Kim and Narayan*, 2003):

$$\mathbf{F}_{\rm MLT}(r) = F_{\rm MLT}(r)\mathbf{e}_r = -\frac{u_{\rm rms} l_{\rm coh} \xi(r)}{3} \rho(r) T(r) \frac{\partial s(r)}{\partial r} \mathbf{e}_r, \tag{5.3}$$

where $s(r) = c_v \ln\left(\frac{P(r)}{\rho(r)^\gamma}\right)$ is the specific gas entropy, $c_v = \frac{k_B}{\mu m_p (\gamma - 1)}$ is the heat capacity at constant volume per unit mass, m_p is proton mass, k_B is the Boltzmann constant, $\mu \approx 0.6$ is the mean molecular weight of the plasma, $u_{\rm rms}$ is the root mean square velocity of the turbulence, $\mathbf{e}_r$ is the unit vector along the radial direction, and $T(r)$ is the radial profiles of gas temperature. The $\xi(r)$ is a dimensionless factor correcting for the effect of gravitational stratification. It takes the form of (*Weinstock*, 1981)

$$\xi(r) = \frac{1}{1 + c_1 F r^{-2}}. \tag{5.4}$$

Weinstock (1981) calibrates the parameter c_1 using numerical simulations of vertically-stratified medium in the parameter regime appropriate for the Earth's atmosphere. Here I calibrate this parameter in my simulations in the context of galaxy clusters. The heating rate due to turbulent mixing predicted from the analytic model is

$$\dot{e}_{\rm MLT}(r) = -\nabla \cdot \mathbf{F}_{\rm MLT}(r) = -\frac{1}{r^2} \frac{\partial (r^2 F_{\rm MLT})}{\partial r}. \tag{5.5}$$

5.4 Preliminary results: Analytical model of turbulent mixing calibrated by the simulations

As the simulation proceeds, the spectral forcing scheme drives turbulence in the halo. The $u_{\rm rms}$ increases with time. After the simulated halo has been sufficiently stirred (i.e., after a few eddy turnover times at the driving scale), the energy injection from the forcing scheme

balances the dissipation of turbulent energy due to numerical viscosity. Consequently, the turbulent velocity $u_{\rm rms}$ reaches a plateau after $\sim$ 300 Myr.

I calculated the convective flux in the simulation ($\mathbf{F}_{\rm conv}$) using:

$$\mathbf{F}_{\rm conv}(r) = F_{\rm conv}(r)\mathbf{e}_r = \frac{\gamma}{\gamma-1} k_B \left(\langle nu_r T\rangle - \langle nu_r\rangle \langle T\rangle\right) \mathbf{e}_r, \tag{5.6}$$

where n is the gas number density, u_r is the radial velocity, and <> represents averaging over the solid angle, e.g., $\langle T\rangle = \frac{1}{4\pi}\int T(r,\Omega)\mathrm{d}\Omega$. The convective heat flux is obtained by subtracting the heat flux due to mass inflow/outflow from the total heat flux. Thus, the actual heating rate due to the convective flux is

$$\dot{e}_{\rm conv}(r) = -\nabla\cdot\mathbf{F}_{\rm conv}(r) = -\frac{1}{r^2}\frac{\partial(r^2 F_{\rm conv})}{\partial r}. \tag{5.7}$$

I then fit the radial profile of $\dot{e}_{\rm conv}$ calculated from my simulations with the analytical formula for $\dot{e}_{\rm MLT}(r)$ (Eq.5.5, where the free parameter is c_1).

My results for isobaric case (i.e., runs IB-SL03, IB-SL05, and IB-SL08) suggest that when gravitational stratification is excluded ($Fr \rightarrow \infty$, and $\xi = 1$), the standard mixing length theory as described in *Kim and Narayan* (2003) describes the heating rate due to turbulent mixing very well. As shown in the top and the lower left panels in Fig. 5.1, the $\dot{e}_{\rm MLT}$ from analytical model with $\xi = 1$ (the grey lines) is in good agreement with the heating rate due to turbulent convection measured from simulations ($\dot{e}_{\rm conv}$; red lines). On the other hand, in PER-HSE run, where stratification is present, the prediction from standard mixing length theory significantly deviates from the actual turbulent mixing heating rate. This is demonstrated by the offset between the dashed grey line (representing the prediction from standard mixing length theory) and the red line (representing the values measured from the simulation) in the lower right panel in Fig. 5.1. However, I find that the mixing length model corrected for the gravitational stratification (dotted solid black line) can accurately describe the turbulent mixing heating rate directly measured from the numerical simulations. The

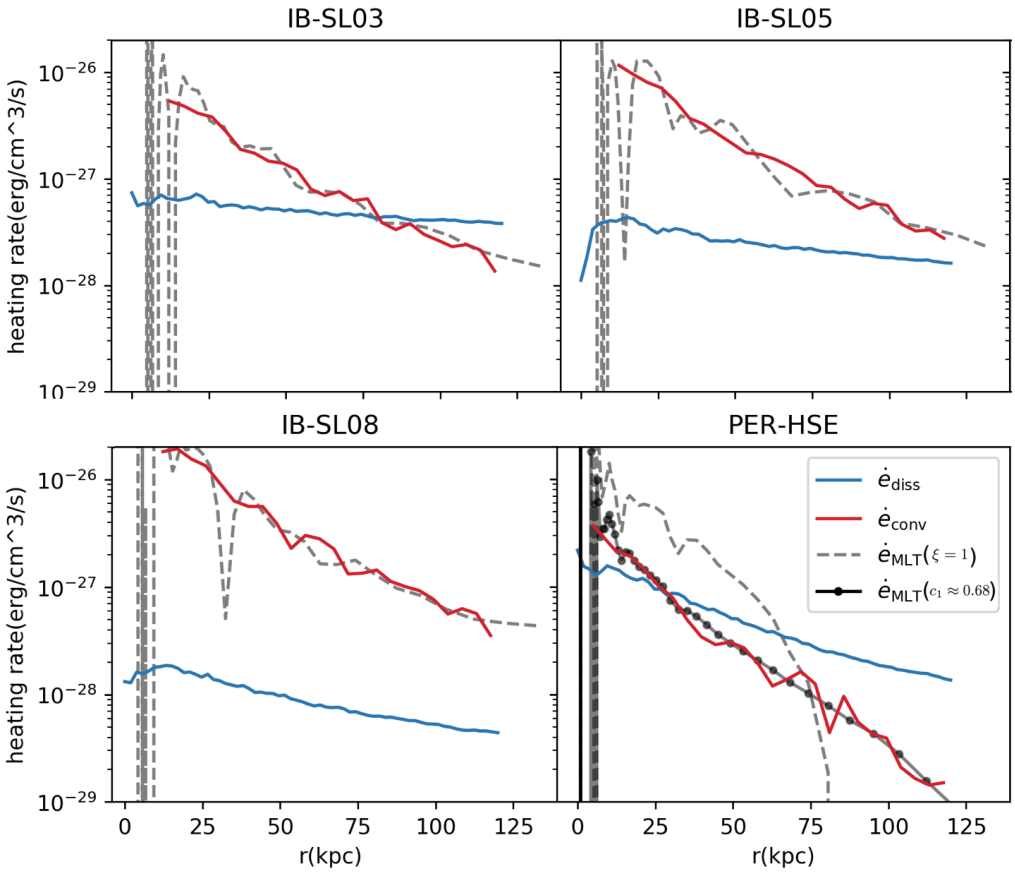

Figure 5.1: Averaged radial profiles of the heating rates. The dashed grey lines correspond to the turbulent mixing heating rate predicted from the standard mixing length theory ($\xi = 1$); the red lines correspond to the actual turbulent mixing heating rates measured from the simulations; the dotted black line corresponds to the prediction from the mixing length theory corrected for stratification with the best fit value of the free parameter $c_1 \approx 0.68$. All profiles are averaged over $t =$ 0.3 to 1 Gyr, i.e., after the turbulence has reached a steady state.

best fit requires

$$c_1 \approx 0.68, \tag{5.8}$$

which is a factor of 16 larger than the original value calibrated in *Weinstock* (1981) for the conditions appropriate for the Earth's atmosphere.

5.5 Future work

Kolmogorov's theory of isotropic turbulence predicts that as turbulent eddies cascade down to the viscous scale, the energy deposition rate of turbulent dissipation is

$$\dot{e}_{\rm diss} = \alpha \frac{\rho u_{\rm rms}^3}{l_{\rm drive}}, \tag{5.9}$$

where α is a constant. When gravitational stratification is included, *Pouquet et al.* (2018) show that α becomes a function of the Froude number:

$$\alpha \propto Fr^{0.91} \ (0.01 \lesssim Fr \lesssim 0.2). \tag{5.10}$$

When the medium is weakly stratified ($Fr > 0.2$), α has the same constant value as in the case of non-stratified turbulence, while for strong stratification ($Fr < 0.01$), the effect of stratification saturates and α assumes a smaller constant value (see Fig.1(c) in *Pouquet et al.*, 2018).

The four simulations that I have performed so far are either non-stratified or too weakly stratified; and the gravitational stratification does not affect the turbulent dissipation. Therefore, I plan to set up additional simulations in order to search the parameter space of smaller *Fr*, so that I can produce a relation between α and *Fr* covering a large range of *Fr* expected in the cluster environments. I anticipate obtaining the same proportionality as that in *Pouquet et al.* (2018) but the exact values of α and range of *Fr* might be different.

Thus, one can present an analytical formula for calculating the turbulent dissipation rate in stratified medium calibrated from cluster simulations. Together with the analytic model for turbulent mixing heating (Eq. 5.5 with $c_1 = 0.68$), one can compare the relative importance of turbulent mixing and dissipation in counterbalancing the radiative cooling given the properties of thermal profiles and turbulence in the ICM.

CHAPTER VI

Summary and Future Work

In this thesis, I study the evolution of hot gaseous halos and how the AGN feedback, fueled by the cooling of the hot halo gas, interacts with the gaseous halos. I summarize the key findings as follows.

1. My numerical simulations demonstrate that self-regulated AGN feedback can maintain the observed multi- or single- phase nature of the gaseous halos in elliptical galaxies. Multiphase halos are characterized by the presence of extended cold gas structures that condensed out of the hot gas, and the thermal properties of the hot gas (e.g., entropy gradient, cooling time to free-fall time ratio) that are conducive to the development of thermal instability. In single-phase gaseous halos, the cold gas exists only in the central nuclear regions and the hot is less likely to develop thermal instability. Such multiphase and single-phase dichotomy was first observed by *Werner et al.* (2014) (which motivated my work) and subsequently confirmed by the observations with larger sample size (*Lakhchaura et al.*, 2018). Furthermore, a recent work analysing entropy profiles of nearby early-type galaxies finds excellent agreement with my single-phase galaxy model (*Frisbie et al.*, 2020). My simulations of self-regulated AGN feedback in the gaseous halos in giant elliptical galaxies show excellent consistency with the multi-wavelength observations of these galaxies. Thus, my numerical model is able to robustly describe the observed properties of

these gaseous halos.

2. Hydrodynamic simulations of AGN feedback and cold gas condensation in hot gaseous halos often reveal the formation of long-lived and massive rotating disks. These results were reported both in the literature and in this thesis, including the MPG and SPG runs in Chapter II, the KINETIC run in Chapter III, and LR-HD, FID-HD runs in Chapter IV. However, such disks are in tension with the observations. My work suggests that including weak magnetic fields can prevent the formation of the cold disks. At the locations where condensation happens, magnetic fields are locally amplified due to flux freezing. The enhanced magnetic tension force decelerates the cold clouds, extracts angular momentum from them, and thus can prevent the formation of the rotating cold disks. My work illustrates the importance of including magnetic fields in the numerical simulations of AGN feedback and multiphase gaseous halos and provides a solution to the "disk problem," which is commonly encountered in AGN feedback simulations reported in the literature.

3. When plasma composition in the AGN jets is dominated by CRs, cooling catastrophes can be prevented, the gas does not overheat, and massive cold central disks do not form, provided that CR streaming is included. CR transport helps to distribute the AGN energy more evenly throughout the cool cores and heat the ICM. This process ensures that CRs come into direct contact with sufficiently large fraction of the radiatively cooling atmosphere, which in turn helps to maintain global thermodynamical equilibrium. Furthermore, compared to the kinetic AGN jet case, CR-dominated AGN jets have reduced power due to more efficient energy utilization, i.e., better coupling of the AGN-supplied energy to the ICM.

4. Consistent with the properties of turbulence in the cold ICM phase (*Li et al.*, 2020), my simulations of AGN feedback and cold gas condensation suggest that the ICM turbulence is non-Kolmogorov, i.e., the first order VSFs of the multiphase ICM

are steeper than the VSF predicted from the Kolmogorov theory (that VSF has a slope of 1/3). The turbulent motions of the cold gas are primarily driven by the gravitational acceleration. This leads to the cold phase VSF slope close to 1/2. The turbulence in the hot gas in the central regions of cool cores can be driven by both the AGN feedback and ambient cold filament motions. Interestingly, the magnetic fields facilitate enhanced coupling between the AGN driven outflows and the ambient hot gas; when the magnetic fields are excluded, the cold filaments are the dominant driving source of turbulence in the simulated hot gas. A non-Kolmogorov nature of turbulence in the multiphase ICM predicted by my simulations has important implications for the role of turbulence in heating the hot gaseous halos. Specifically, the steeper velocity structure function of turbulence predicted by my models indicates that the heating rate due to turbulent dissipation derived from the Kolmogorov's theory, i.e., $\propto v_l^3/l$, may severely overestimate the actual heating rate.

Motivated by several major findings presented in my thesis, I intend to pursue a number of follow-up research projects. My general plans for the future work are listed below.

1. Although the formation of long-lived massive cold disks found in the simulations of AGN feedback and cold gas condensation are in tension with the observations, cold disks do exist in many early-type galaxies. These disks either have origins other than the condensation of hot gaseous halos or are generated from rotating hot halos, as suggested by observations of systems with significant angular momentum (*Juráňová et al.*, 2020). The recent numerical study (*Gaspari et al.*, 2015) on the condensation of rotating hot halo demonstrates that the cold disks can form that way and that the level of turbulence significantly affects the angular momentum evolution of the disks. However, *Gaspari et al.* (2015) does not include AGN feedback, and the turbulence therein is generated manually. I will perform numerical simulations of rotating hot gaseous halos and employ the AGN feedback model used in my previous works. In this way, I will study the evolution of the cold disks, their interaction with the AGN

jets, and how the disks are affected by the turbulence that is self-consistently generated by the AGN jets in the full feedback loop.

2. My recent results from MHD simulations of AGN feedback demonstrated that the VSF slope of the cold phase departs from Kolmogorov prediction (Chapter IV). I will build on this work to make specific predictions for the actual observables (i.e., properly projected mock observations of the VSF) that could be compared to the existing data (*Li et al.*, 2020) in order to put constraints on the ICM turbulence and thus the feedback physics. This work will also make predictions for the hot phase VSF that could assist us in the interpretation of the data from future *Lynx* or *Athena* missions.

APPENDICES

APPENDIX A

Driven Turbulence Test and Inertial Range

In order to verify that the expected reference value of the hot phase VSF slope is indeed 1/3, and to assess at what minimum separations numerical effects become important, we perform controlled turbulence experiment neglecting AGN feedback, magnetic fields, radiative cooling, and gravity. In this idealized test turbulence is driven via a spectral forcing scheme utilizing an Ornstein–Uhlenbeck random process. The spectral forcing scheme is set to stir the hot halo via a time-correlated, stochastic forcing with a narrow spectral range corresponding to $\sim$ 10 kpc. We use the same implementation of this scheme and model parameters as described in *Ruszkowski and Oh* (2010). The computational volume in this test is uniformly refined and the resolution is the same as in the FID-HD and FID-MHD cases.

After $\sim$ 250 Myr, the turbulent dissipation balances the energy injection rate due to the forcing and the 3D rms velocity stabilizes at $\sim$ 150 km s^{-1} (top panel in Fig. A.1). Variations are caused in part by the fact that we use finite correlation timescale for the driving forces ($\sim$100 Myr). This is reflected in the top panel in Fig. A.1 that shows that characteristic timescale for the fluctuations in the velocity dispersion is about 100 Myr.

As expected, the VSF reaches a stable state, where the VSF follows the Kolmogorov prediction in the inertial range with the averaged slope equal to $m_{\rm kol} = 1/3$. The fluctuations

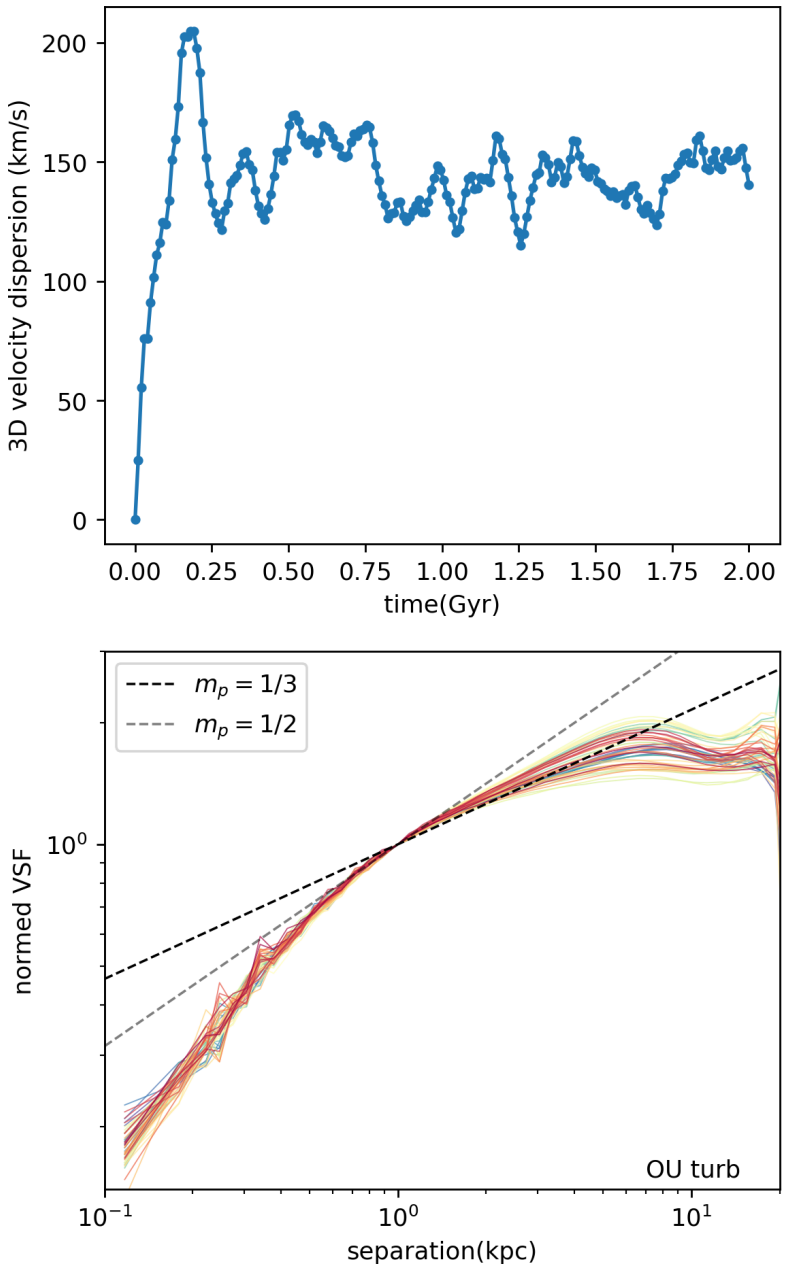

Figure A.1: Top panel: time evolution of the 3D velocity dispersion in the driving turbulence test (see Appendix A). Bottom panel: VSFs plotted every 10 Myr from $t = 1$ to 1.5 Gyr for the driving turbulence test. The color scheme is the same as Fig. 4.6.

in the slope are again a direct consequence of the finite correlation timescale and fluctuations in the overall level of velocity dispersion. The VSF slope steepens on sub-kpc scales (bottom panel in Fig. A.1). This indicates that the steepening of the VSF on sub-kpc scales is numerical in origin.

APPENDIX B

VSF of Idealized Motion Dominated by Gravity

In order to investigate the VSF slope resulting from motions dominated by gravity, we perform a simple one-dimensional calculation. We consider the motion of a test particle falling in the gravitational field $g_{\rm test}(x) = -{\rm sign}(x)g_0$, where g_0 is a constant (note that the gravitational acceleration in the central region of the cluster is approximately constant, which simplifies our analysis of the impact of gravity on the motions of cold gas clouds; see Fig. 4.5). The time evolution of the particle velocity and position are shown in Fig. B.1. We sample the velocities and positions on this trajectory and calculate the VSF. In Fig. B.2, we show VSFs corresponding to three different sampling cases: (i) when we sample the part of the trajectory that does not include overshooting through the very center (time range from 1 to 2 in Fig. B.1), the VSF slope is close to or slightly above 1/2 (green line in Fig. B.2); (ii) when we exclude the the times past the turnover where velocity changes sign (i.e., when we consider the time range from 1 to 3), the VSF slope is close to 1/2 (blue line in Fig. B.2); (iii) when sampling over a longer trajectory that includes the turnover (time ranging from 0 to 5), the VSF slope is close to 1/3 (orange line in Fig. B.2).

Our full physics simulation results imply that rather than getting launched by the jet from the center and raining back, most of the cold filaments form in the atmosphere and fall towards the center. In Fig. B.3 we show the amount of cold gas that is inflowing (blue

lines) and outflowing (orange lines). It is evident from this figure that the inflow dominates over outflow. The infalling cold clouds either get accreted by the black hole or collide with the preexisting cold gas clumps. Therefore, the velocity magnitude of the clouds is damped by the collisions with the preexisting cold gas as they overshoot the center of the cluster. This situation corresponds approximately to the case in between (i) and (ii) above, where the expected slope is either 1/2 or slightly above it. As our simple experiment also demonstrates that longer sampling time range results in flatter VSF slopes. As the actual magnitude of the cloud velocity is expected to be damped over time, this simple test shows that the velocities and positions sampled from a free-falling trajectory can lead to the VSF slope close to $\sim$1/2 as seen in the full physics simulations.

As mentioned in the main text, the effect of the magnetic fields is to decelerate the clouds, which may further flatten the slope below 1/2. Interestingly, the dynamical effect of the magnetic fields are also seen in Fig. B.3. Top and bottom panels in this figure corresponds to the FID-HD and FID-MHD cases, respectively. This figure shows that in the FID-MHD case outflow is even more subdominant compared to inflow. This is consistent with stronger damping of motions by the magnetic tension, especially as the clouds get closer to the center, that reduces the tendency of the infalling cold gas to overshoot the center.

Since the objective of this simple experiment is to provide a proof of concept for the idea that ballistic (or nearly ballistic) motions can account for the cold phase VSF slopes, we choose not do pursue a more detailed analysis including additional free parameters such as the cloud velocity damping time or the distributions of heights from which the clouds are released, etc.

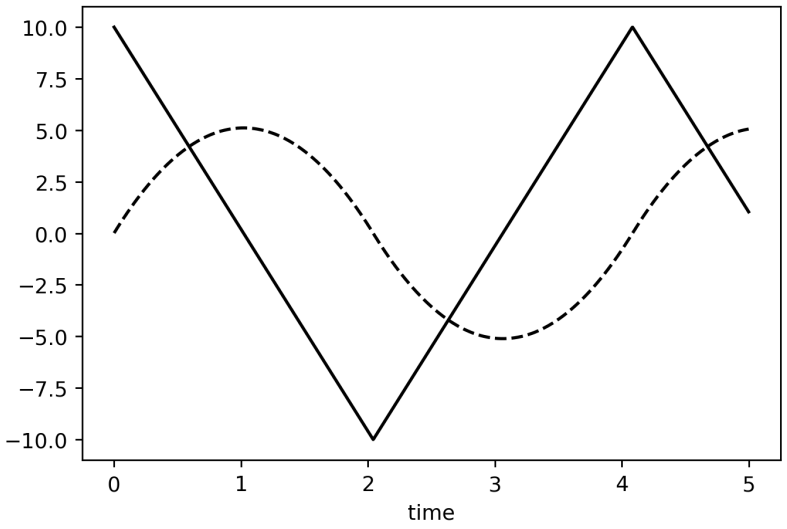

Figure B.1: Time evolution of velocity (solid) and position (dashed line) of a test particle in a 1D gravitational potential $g_{\rm test}(x)$ (see Appendix B). All quantities are in arbitrary units.

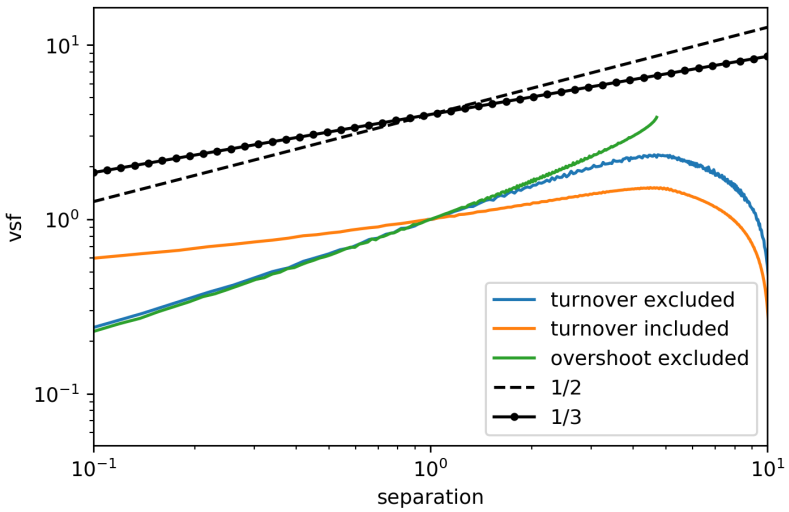

Figure B.2: VSF of velocities and positions sampled from the trajectory of motion dominated by gravity. The meaning of color is the same as Fig. B.1.

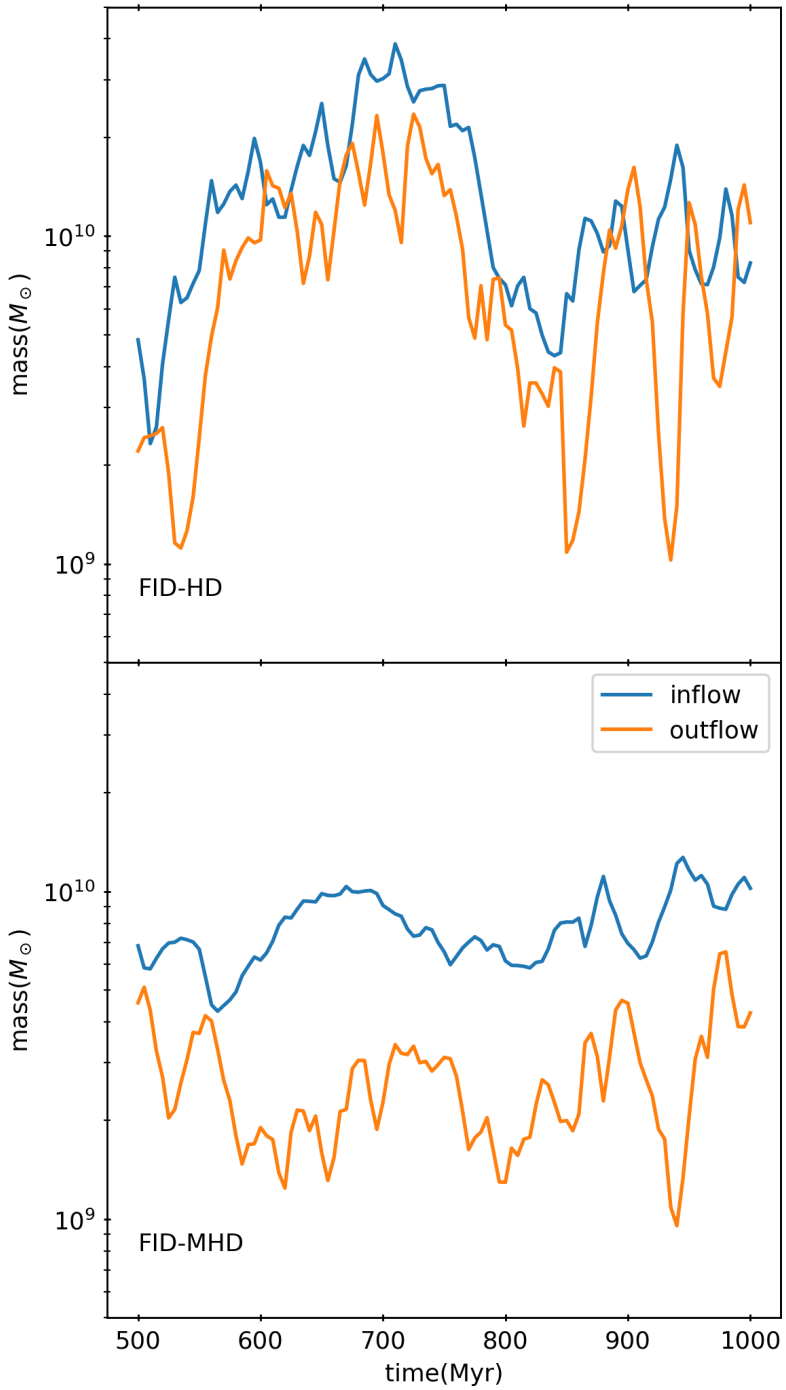

Figure B.3: The evolution of the inflowing (blue lines) and ouftlowing (oragne lines) cold gas mass. Top panel corresponds to the FID-HD case and the bottom one to the FID-MHD case.

BIBLIOGRAPHY

BIBLIOGRAPHY

Abdo, A. A., et al. (2012), Fermi Observations of γ-Ray Emission from the Moon, *ApJ*, *758*(2), 140, doi:10.1088/0004-637X/758/2/140.

Abdulla, Z., et al. (2019), Constraints on the Thermal Contents of the X-Ray Cavities of Cluster MS 0735.6+7421 with Sunyaev-Zel'dovich Effect Observations, *ApJ*, *871*(2), 195, doi:10.3847/1538-4357/aaf888.

Alatalo, K., et al. (2013), The ATLAS^{3D} project - XVIII. CARMA CO imaging survey of early-type galaxies, *MNRAS*, *432*, 1796–1844, doi:10.1093/mnras/sts299.

Athey, A. E. (2007), Chandra Observations of Early-type Galaxies, Ph.D. thesis, Univ. of Michigan, 2007.

Babul, A., P. Sharma, and C. S. Reynolds (2013), Isotropic Heating of Galaxy Cluster Cores via Rapidly Reorienting Active Galactic Nucleus Jets, *ApJ*, *768*(1), 11, doi:10.1088/0004-637X/768/1/11.

Babyk, I. V., B. R. McNamara, P. E. J. Nulsen, H. R. Russell, A. N. Vantyghem, M. T. Hogan, and F. A. Pulido (2018), A Universal Entropy Profile for the Hot Atmospheres of Galaxies and Clusters within R $_{2500}$, *ApJ*, *862*(1), 39, doi:10.3847/1538-4357/aacce5.

Babyk, I. V., B. R. McNamara, P. D. Tamhane, P. E. J. Nulsen, H. R. Russell, and A. C. Edge (2019), Origins of Molecular Clouds in Early-type Galaxies, *ApJ*, *887*(2), 149, doi:10.3847/1538-4357/ab54ce.

Baganoff, F. K., et al. (2003), Chandra X-Ray Spectroscopic Imaging of Sagittarius A* and the Central Parsec of the Galaxy, *ApJ*, *591*, 891–915, doi:10.1086/375145.

Balbus, S. A., and N. Soker (1989), Theory of local thermal instability in spherical systems, *ApJ*, *341*, 611–630, doi:10.1086/167521.

Bambic, C. J., and C. S. Reynolds (2019), Efficient Production of Sound Waves by AGN Jets in the Intracluster Medium, *ApJ*, *886*(2), 78, doi:10.3847/1538-4357/ab4daf.

Barai, P., G. Murante, S. Borgani, M. Gaspari, G. L. Granato, P. Monaco, and C. Ragone-Figueroa (2016), Kinetic AGN feedback effects on cluster cool cores simulated using SPH, *MNRAS*, *461*, 1548–1567, doi:10.1093/mnras/stw1389.

Battaglia, N., J. R. Bond, C. Pfrommer, and J. L. Sievers (2012), On the Cluster Physics of Sunyaev-Zel'dovich and X-Ray Surveys. I. The Influence of Feedback, Non-thermal Pressure, and Cluster Shapes on Y-M Scaling Relations, *ApJ*, *758*(2), 74, doi:10.1088/0004-637X/758/2/74.

Beckmann, R. S., et al. (2019), Dense gas formation and destruction in a simulated Perseus-like galaxy cluster with spin-driven black hole feedback, *A&A*, *631*, A60, doi:10.1051/0004-6361/201936188.

Birnboim, Y., and A. Dekel (2003), Virial shocks in galactic haloes?, *MNRAS*, *345*(1), 349–364, doi:10.1046/j.1365-8711.2003.06955.x.

Bîrzan, L., et al. (2020), LOFAR observations of X-ray cavity systems, *MNRAS*, *496*(3), 2613–2635, doi:10.1093/mnras/staa1594.

Bondi, H. (1952), On spherically symmetrical accretion, *MNRAS*, *112*, 195.

Booth, C. M., O. Agertz, A. V. Kravtsov, and N. Y. Gnedin (2013), Simulations of Disk Galaxies with Cosmic Ray Driven Galactic Winds, *ApJ*, *777*, L16, doi:10.1088/2041-8205/777/1/L16.

Bourne, M. A., and D. Sijacki (2017), AGN jet feedback on a moving mesh: cocoon inflation, gas flows and turbulence, *MNRAS*, *472*(4), 4707–4735, doi:10.1093/mnras/stx2269.

Bourne, M. A., D. Sijacki, and E. Puchwein (2019), AGN jet feedback on a moving mesh: lobe energetics and X-ray properties in a realistic cluster environment, *MNRAS*, *490*(1), 343–349, doi:10.1093/mnras/stz2604.

Bregman, J. N., and E. J. Lloyd-Davies (2006), On the Lack of a Soft X-Ray Excess from Clusters of Galaxies, *ApJ*, *644*, 167–173, doi:10.1086/503551.

Bregman, J. N., E. D. Miller, A. E. Athey, and J. A. Irwin (2005), On VI in Elliptical Galaxies: Indicators of Cooling Flows, *ApJ*, *635*, 1031–1043, doi:10.1086/497421.

Brighenti, F., W. G. Mathews, and P. Temi (2015), Hot Gaseous Atmospheres in Galaxy Groups and Clusters Are Both Heated and Cooled by X-Ray Cavities, *ApJ*, *802*, 118, doi:10.1088/0004-637X/802/2/118.

Brüggen, M., and C. R. Kaiser (2002), Hot bubbles from active galactic nuclei as a heat source in cooling-flow clusters, *Nature*, *418*, 301–303, doi:10.1038/nature00857.

Bryan, G. L., et al. (2014), ENZO: An Adaptive Mesh Refinement Code for Astrophysics, *ApJS*, *211*, 19, doi:10.1088/0067-0049/211/2/19.

Buote, D. A., A. D. Lewis, F. Brighenti, and W. G. Mathews (2003a), XMM-Newton and Chandra Observations of the Galaxy Group NGC 5044. I. Evidence for Limited Multiphase Hot Gas, *ApJ*, *594*, 741–757, doi:10.1086/377094.

Buote, D. A., A. D. Lewis, F. Brighenti, and W. G. Mathews (2003b), XMM-Newton and Chandra Observations of the Galaxy Group NGC 5044. II. Metal Abundances and Supernova Fraction, *ApJ*, *595*, 151–166, doi:10.1086/377256.

Buote, D. A., F. Brighenti, and W. G. Mathews (2004), Ultralow Iron Abundances in the Distant Hot Gas in Galaxy Groups, *ApJ*, *607*, L91–L94, doi:10.1086/422097.

Butsky, I., and T. R. Quinn (2018), The Role of Cosmic Ray Transport in Shaping the Simulated Circumgalactic Medium, *ArXiv e-prints*.

Butsky, I. S., D. B. Fielding, C. C. Hayward, C. B. Hummels, T. R. Quinn, and J. K. Werk (2020), The Impact of Cosmic Rays on Thermal Instability in the Circumgalactic Medium, *ApJ*, *903*(2), 77, doi:10.3847/1538-4357/abbad2.

Cappellari, M., et al. (2011), The ATLAS^{3D} project - I. A volume-limited sample of 260 nearby early-type galaxies: science goals and selection criteria, *MNRAS*, *413*(2), 813–836, doi:10.1111/j.1365-2966.2010.18174.x.

Cavagnolo, K. W., M. Donahue, G. M. Voit, and M. Sun (2008), An Entropy Threshold for Strong Hα and Radio Emission in the Cores of Galaxy Clusters, *ApJ*, *683*(2), L107, doi:10.1086/591665.

Cavagnolo, K. W., M. Donahue, G. M. Voit, and M. Sun (2009), Intracluster Medium Entropy Profiles for a Chandra Archival Sample of Galaxy Clusters, *ApJS*, *182*(1), 12–32, doi:10.1088/0067-0049/182/1/12.

Cen, R., and J. P. Ostriker (1992), Galaxy formation and physical bias, *ApJ*, *399*, L113–L116, doi:10.1086/186620.

Choi, E., J. P. Ostriker, T. Naab, and P. H. Johansson (2012), Radiative and Momentum-based Mechanical Active Galactic Nucleus Feedback in a Three-dimensional Galaxy Evolution Code, *ApJ*, *754*, 125, doi:10.1088/0004-637X/754/2/125.

Choudhury, P. P., P. Sharma, and E. Quataert (2019), Multiphase gas in the circumgalactic medium: relative role of t_{cool}/t_{ff} and density fluctuations, *MNRAS*, *488*(3), 3195–3210, doi:10.1093/mnras/stz1857.

Chung, A., M. Bureau, J. H. van Gorkom, and B. Koribalski (2012), The H I environment of counter-rotating gas hosts: gas accretion from cold gas blobs, *MNRAS*, *422*(2), 1083–1091, doi:10.1111/j.1365-2966.2012.20679.x.

Churazov, E., W. Forman, C. Jones, and H. Böhringer (2003), XMM-Newton Observations of the Perseus Cluster. I. The Temperature and Surface Brightness Structure, *ApJ*, *590*(1), 225–237, doi:10.1086/374923.

Churazov, E., M. Ruszkowski, and A. Schekochihin (2013), Powering of cool filaments in cluster cores by buoyant bubbles - I. Qualitative model, *MNRAS*, *436*, 526–530, doi:10.1093/mnras/stt1594.

Ciotti, L., and J. P. Ostriker (1997), Cooling Flows and Quasars: Different Aspects of the Same Phenomenon? I. Concepts, *ApJ*, *487*, L105–L108, doi:10.1086/310902.

Ciotti, L., and J. P. Ostriker (2001), Cooling Flows and Quasars. II. Detailed Models of Feedback-modulated Accretion Flows, *ApJ*, *551*(1), 131–152, doi:10.1086/320053.

Ciotti, L., and J. P. Ostriker (2007), Radiative Feedback from Massive Black Holes in Elliptical Galaxies: AGN Flaring and Central Starburst Fueled by Recycled Gas, *ApJ*, *665*(2), 1038–1056, doi:10.1086/519833.

Ciotti, L., A. D'Ercole, S. Pellegrini, and A. Renzini (1991), Winds, Outflows, and Inflows in X-Ray Elliptical Galaxies. I., *ApJ*, *376*, 380, doi:10.1086/170289.

Ciotti, L., J. P. Ostriker, and D. Proga (2010), Feedback from Central Black Holes in Elliptical Galaxies. III. Models with Both Radiative and Mechanical Feedback, *ApJ*, *717*(2), 708–723, doi:10.1088/0004-637X/717/2/708.

Ciotti, L., S. Pellegrini, A. Negri, and J. P. Ostriker (2017), The Effect of the AGN Feedback on the Interstellar Medium of Early-Type Galaxies:2D Hydrodynamical Simulations of the Low-Rotation Case., *ApJ*, *835*, 15, doi:10.3847/1538-4357/835/1/15.

Combes, F., L. M. Young, and M. Bureau (2007), Molecular gas and star formation in the SAURON early-type galaxies, *MNRAS*, *377*(4), 1795–1807, doi:10.1111/j.1365-2966.2007.11759.x.

Conroy, C., and J. P. Ostriker (2008), Thermal Balance in the Intracluster Medium: Is AGN Feedback Necessary?, *ApJ*, *681*, 151–166, doi:10.1086/587861.

Conroy, C., P. G. van Dokkum, and A. Kravtsov (2015), Preventing Star Formation in Early-Type Galaxies with Late-Time Stellar Heating, *ApJ*, *803*, 77, doi:10.1088/0004-637X/803/2/77.

Crocker, A. F., M. Bureau, L. M. Young, and F. Combes (2011), Molecular gas and star formation in early-type galaxies, *MNRAS*, *410*(2), 1197–1222, doi:10.1111/j.1365-2966.2010.17537.x.

Croton, D. J., et al. (2006), The many lives of active galactic nuclei: cooling flows, black holes and the luminosities and colours of galaxies, *MNRAS*, *365*(1), 11–28, doi:10.1111/j.1365-2966.2005.09675.x.

David, L. P., P. E. J. Nulsen, B. R. McNamara, W. Forman, C. Jones, T. Ponman, B. Robertson, and M. Wise (2001), A High-Resolution Study of the Hydra A Cluster with Chandra: Comparison of the Core Mass Distribution with Theoretical Predictions and Evidence for Feedback in the Cooling Flow, *ApJ*, *557*, 546–559, doi:10.1086/322250.

Davis, T. A., J. Greene, C.-P. Ma, V. Pandya, J. P. Blakeslee, N. McConnell, and J. Thomas (2016), The MASSIVE survey - III. Molecular gas and a broken Tully-Fisher relation in the most massive early-type galaxies, *MNRAS*, *455*(1), 214–226, doi:10.1093/mnras/stv2313.

Davis, T. A., J. E. Greene, C.-P. Ma, J. P. Blakeslee, J. M. Dawson, V. Pandya, M. Veale, and N. Zabel (2019), The MASSIVE survey - XI. What drives the molecular gas properties of early-type galaxies, *MNRAS*, *486*(1), 1404–1423, doi:10.1093/mnras/stz871.

Davis, T. A., et al. (2011), The ATLAS^{3D} project - X. On the origin of the molecular and ionized gas in early-type galaxies, *MNRAS*, *417*(2), 882–899, doi:10.1111/j.1365-2966.2011.19355.x.

Davis, T. A., et al. (2013), The ATLAS^{3D} Project - XIV. The extent and kinematics of the molecular gas in early-type galaxies, *MNRAS*, *429*(1), 534–555, doi:10.1093/mnras/sts353.

de Gasperin, F., et al. (2012), M 87 at metre wavelengths: the LOFAR picture, *A&A*, *547*, A56, doi:10.1051/0004-6361/201220209.

De Pontieu, B., P. C. H. Martens, and H. S. Hudson (2001), Chromospheric Damping of Alfvén Waves, *ApJ*, *558*, 859–871, doi:10.1086/322408.

De Young, D. S. (2010), How Does Radio AGN Feedback Feed Back?, *ApJ*, *710*, 743–754, doi:10.1088/0004-637X/710/1/743.

Dekel, A., and Y. Birnboim (2006), Galaxy bimodality due to cold flows and shock heating, *MNRAS*, *368*(1), 2–20, doi:10.1111/j.1365-2966.2006.10145.x.

Donahue, M., G. E. de Messières, R. W. O'Connell, G. M. Voit, A. Hoffer, B. R. McNamara, and P. E. J. Nulsen (2011), Polycyclic Aromatic Hydrocarbons, Ionized Gas, and Molecular Hydrogen in Brightest Cluster Galaxies of Cool-core Clusters of Galaxies, *ApJ*, *732*(1), 40, doi:10.1088/0004-637X/732/1/40.

Donahue, M., et al. (2015a), Ultraviolet Morphology and Unobscured UV Star Formation Rates of CLASH Brightest Cluster Galaxies, *ApJ*, *805*(2), 177, doi:10.1088/0004-637X/805/2/177.

Donahue, M., et al. (2015b), Ultraviolet Morphology and Unobscured UV Star Formation Rates of CLASH Brightest Cluster Galaxies, *ApJ*, *805*, 177, doi:10.1088/0004-637X/805/2/177.

Dubey, A., L. Reid, and R. Fisher (2008), Introduction to flash 3.0, with application to supersonic turbulence, *Physica Scripta*, *2008*(T132), 014,046.

Dunn, R. J. H., and A. C. Fabian (2004), Particle energies and filling fractions of radio bubbles in cluster cores, *MNRAS*, *355*, 862–873, doi:10.1111/j.1365-2966.2004.08365.x.

Dunn, R. J. H., A. C. Fabian, and J. S. Sanders (2006), Precession of the super-massive black hole in NGC 1275 (3C 84)?, *MNRAS*, *366*(3), 758–766, doi:10.1111/j.1365-2966.2005.09928.x.

Edge, A. C. (2001), The detection of molecular gas in the central galaxies of cooling flow clusters, *MNRAS*, *328*(3), 762–782, doi:10.1046/j.1365-8711.2001.04802.x.

Ehlert, K., R. Weinberger, C. Pfrommer, R. Pakmor, and V. Springel (2018), Simulations of the dynamics of magnetized jets and cosmic rays in galaxy clusters, *MNRAS*, *481*(3), 2878–2900, doi:10.1093/mnras/sty2397.

Ehlert, K., C. Pfrommer, R. Weinberger, R. Pakmor, and V. Springel (2019), The Sunyaev-Zel'dovich Effect of Simulated Jet-inflated Bubbles in Clusters, *ApJ*, *872*(1), L8, doi:10.3847/2041-8213/ab020d.

Ehlert, K., R. Weinberger, C. Pfrommer, and V. Springel (2021), Connecting turbulent velocities and magnetic fields in galaxy cluster simulations with active galactic nuclei jets, *MNRAS, in press*, arXiv:2011.13964.

Eisenreich, M., T. Naab, E. Choi, J. P. Ostriker, and E. Emsellem (2017), Active galactic nuclei feedback, quiescence and circumgalactic medium metal enrichment in early-type galaxies, *MNRAS*, *468*, 751–768, doi:10.1093/mnras/stx473.

Enßlin, T., C. Pfrommer, F. Miniati, and K. Subramanian (2011), Cosmic ray transport in galaxy clusters: implications for radio halos, gamma-ray signatures, and cool core heating, *A&A*, *527*, A99, doi:10.1051/0004-6361/201015652.

Esmerian, C. J., A. V. Kravtsov, Z. Hafen, C.-A. Faucher-Giguère, E. Quataert, J. Stern, D. Kereš, and A. Wetzel (2021), Thermal instability in the CGM of $L_\star$ galaxies: testing 'precipitation' models with the FIRE simulations, *MNRAS*, *505*(2), 1841–1862, doi:10.1093/mnras/stab1281.

Fabian, A. C. (1994), Cooling Flows in Clusters of Galaxies, *ARA&A*, *32*, 277–318, doi:10.1146/annurev.aa.32.090194.001425.

Fabian, A. C. (2012), Observational Evidence of Active Galactic Nuclei Feedback, *ARA&A*, *50*, 455–489, doi:10.1146/annurev-astro-081811-125521.

Fabian, A. C., J. S. Sanders, C. S. Crawford, C. J. Conselice, J. S. Gallagher, and R. F. G. Wyse (2003), The relationship between the optical Hα filaments and the X-ray emission in the core of the Perseus cluster, *MNRAS*, *344*, L48–L52, doi:10.1046/j.1365-8711.2003.06856.x.

Fabian, A. C., C. S. Reynolds, G. B. Taylor, and R. J. H. Dunn (2005), On viscosity, conduction and sound waves in the intracluster medium, *MNRAS*, *363*, 891–896, doi:10.1111/j.1365-2966.2005.09484.x.

Fabian, A. C., J. S. Sanders, G. B. Taylor, S. W. Allen, C. S. Crawford, R. M. Johnstone, and K. Iwasawa (2006), A very deep Chandra observation of the Perseus cluster: shocks, ripples and conduction, *MNRAS*, *366*, 417–428, doi:10.1111/j.1365-2966.2005.09896.x.

Fabian, A. C., R. M. Johnstone, J. S. Sanders, C. J. Conselice, C. S. Crawford, J. S. Gallagher, III, and E. Zweibel (2008), Magnetic support of the optical emission line filaments in NGC 1275, *Nature*, *454*, 968–970, doi:10.1038/nature07169.

Fabian, A. C., J. S. Sanders, R. J. R. Williams, A. Lazarian, G. J. Ferland, and R. M. Johnstone (2011), The energy source of the filaments around the giant galaxy NGC 1275, *MNRAS*, *417*, 172–177, doi:10.1111/j.1365-2966.2011.19034.x.

Fabian, A. C., S. A. Walker, H. R. Russell, C. Pinto, J. S. Sanders, and C. S. Reynolds (2017), Do sound waves transport the AGN energy in the Perseus cluster?, *MNRAS*, *464*, L1–L5, doi:10.1093/mnrasl/slw170.

Ferland, G. J., A. C. Fabian, N. A. Hatch, R. M. Johnstone, R. L. Porter, P. A. M. van Hoof, and R. J. R. Williams (2008), The origin of molecular hydrogen emission in cooling-flow filaments, *MNRAS*, *386*, L72–L76, doi:10.1111/j.1745-3933.2008.00463.x.

Ferland, G. J., A. C. Fabian, N. A. Hatch, R. M. Johnstone, R. L. Porter, P. A. M. van Hoof, and R. J. R. Williams (2009), Collisional heating as the origin of filament emission in galaxy clusters, *MNRAS*, *392*, 1475–1502, doi:10.1111/j.1365-2966.2008.14153.x.

Fielding, D., E. Quataert, M. McCourt, and T. A. Thompson (2017), The impact of star formation feedback on the circumgalactic medium, *MNRAS*, *466*(4), 3810–3826, doi:10.1093/mnras/stw3326.

Ford, H. A., and J. N. Bregman (2013), Direct Detections of Young Stars in Nearby Elliptical Galaxies, *ApJ*, *770*, 137, doi:10.1088/0004-637X/770/2/137.

Forman, W., et al. (2007), Filaments, Bubbles, and Weak Shocks in the Gaseous Atmosphere of M87, *ApJ*, *665*, 1057–1066, doi:10.1086/519480.

Frisbie, R. L. S., M. Donahue, G. M. Voit, T. Connor, Y. Li, M. Sun, K. Lakhchaura, N. Werner, and R. Grossova (2020), Properties of the Hot Ambient Medium of Early-type Galaxies Hosting Powerful Radio Sources, *ApJ*, *899*(2), 159, doi:10.3847/1538-4357/aba8a8.

Fryxell, B., et al. (2000), FLASH: An Adaptive Mesh Hydrodynamics Code for Modeling Astrophysical Thermonuclear Flashes, *ApJS*, *131*, 273–334, doi:10.1086/317361.

Fujita, Y., and Y. Ohira (2013), Radio mini-halo emission from cosmic rays in galaxy clusters and heating of the cool cores, *MNRAS*, *428*, 599–608, doi:10.1093/mnras/sts050.

Fujita, Y., S. Kimura, and Y. Ohira (2013), Stability analysis for cosmic-ray heating of cool cores in galaxy clusters, *MNRAS*, *432*, 1434–1443, doi:10.1093/mnras/stt563.

Gaspari, M., and E. Churazov (2013), Constraining turbulence and conduction in the hot ICM through density perturbations, *A&A*, *559*, A78, doi:10.1051/0004-6361/201322295.

Gaspari, M., F. Brighenti, and P. Temi (2012a), Mechanical AGN feedback: controlling the thermodynamical evolution of elliptical galaxies, *MNRAS*, *424*, 190–209, doi:10.1111/j.1365-2966.2012.21183.x.

Gaspari, M., M. Ruszkowski, and P. Sharma (2012b), Cause and Effect of Feedback: Multiphase Gas in Cluster Cores Heated by AGN Jets, *ApJ*, *746*, 94, doi:10.1088/0004-637X/746/1/94.

Gaspari, M., M. Ruszkowski, and S. P. Oh (2013), Chaotic cold accretion on to black holes, *MNRAS*, *432*, 3401–3422, doi:10.1093/mnras/stt692.

Gaspari, M., F. Brighenti, and P. Temi (2015), Chaotic cold accretion on to black holes in rotating atmospheres, *A&A*, *579*, A62, doi:10.1051/0004-6361/201526151.

Gilkis, A., and N. Soker (2012), Heating the intra-cluster medium perpendicular to the jets axis, *MNRAS*, *427*, 1482–1489, doi:10.1111/j.1365-2966.2012.22085.x.

Guo, F., and S. P. Oh (2008), Feedback heating by cosmic rays in clusters of galaxies, *MNRAS*, *384*, 251–266, doi:10.1111/j.1365-2966.2007.12692.x.

Hamer, S. L., et al. (2014), Cold gas dynamics in Hydra-A: evidence for a rotating disc, *MNRAS*, *437*(1), 862–878, doi:10.1093/mnras/stt1949.

Hillel, S., and N. Soker (2014), Heating cold clumps by jet-inflated bubbles in cooling flow clusters, *MNRAS*, *445*, 4161–4174, doi:10.1093/mnras/stu2047.

Hillel, S., and N. Soker (2016), Heating the intracluster medium by jet-inflated bubbles, *MNRAS*, *455*, 2139–2148, doi:10.1093/mnras/stv2483.

Hillel, S., and N. Soker (2017), Gentle Heating by Mixing in Cooling Flow Clusters, *ApJ*, *845*, 91, doi:10.3847/1538-4357/aa81c5.

Hillel, S., and N. Soker (2020), Kinematics of Filaments in Cooling Flow Clusters and Heating by Mixing, *ApJ*, *896*(2), 104, doi:10.3847/1538-4357/ab9109.

Hitomi Collaboration, et al. (2016), The quiescent intracluster medium in the core of the Perseus cluster, *Nature*, *535*(7610), 117–121, doi:10.1038/nature18627.

Hitomi Collaboration, et al. (2018), Atmospheric gas dynamics in the Perseus cluster observed with Hitomi, *PASJ*, *70*(2), 9, doi:10.1093/pasj/psx138.

Hogan, M. T., et al. (2017), The Onset of Thermally Unstable Cooling from the Hot Atmospheres of Giant Galaxies in Clusters: Constraints on Feedback Models, *ApJ*, *851*(1), 66, doi:10.3847/1538-4357/aa9af3.

Humphrey, P. J., D. A. Buote, F. Gastaldello, L. Zappacosta, J. S. Bullock, F. Brighenti, and W. G. Mathews (2006), A Chandra View of Dark Matter in Early-Type Galaxies, *ApJ*, *646*, 899–918, doi:10.1086/505019.

Iapichino, L., and J. C. Niemeyer (2008), Hydrodynamical adaptive mesh refinement simulations of turbulent flows - II. Cosmological simulations of galaxy clusters, *MNRAS*, *388*(3), 1089–1100, doi:10.1111/j.1365-2966.2008.13518.x.

Indriolo, N., G. A. Blake, M. Goto, T. Usuda, T. Oka, T. R. Geballe, B. D. Fields, and B. J. McCall (2010), Investigating the Cosmic-ray Ionization Rate Near the Supernova Remnant IC 443 through H^+_3 Observations, *ApJ*, *724*, 1357–1365, doi:10.1088/0004-637X/724/2/1357.

Indriolo, N., E. A. Bergin, E. Falgarone, B. Godard, M. A. Zwaan, D. A. Neufeld, and M. G. Wolfire (2018), Constraints on the Cosmic-Ray Ionization Rate in the z $\sim$ 2.3 Lensed Galaxies SMM J2135-0102 and SDP 17b from Observations of OH^+ and H_2O^+, *ApJ*, *865*, 127, doi:10.3847/1538-4357/aad7b3.

Irwin, J. A., and C. L. Sarazin (1996), X-Ray Evidence for the Interaction of the Giant Elliptical Galaxy NGC 4472 with Its Virgo Cluster Environment, *ApJ*, *471*, 683, doi:10.1086/177998.

Jacob, S., and C. Pfrommer (2017a), Cosmic ray heating in cool core clusters - I. Diversity of steady state solutions, *MNRAS*, *467*, 1449–1477, doi:10.1093/mnras/stx131.

Jacob, S., and C. Pfrommer (2017b), Cosmic ray heating in cool core clusters - II. Self-regulation cycle and non-thermal emission, *MNRAS*, *467*, 1478–1495, doi:10.1093/mnras/stx132.

Ji, S., S. P. Oh, and M. McCourt (2018), The impact of magnetic fields on thermal instability, *MNRAS*, *476*(1), 852–867, doi:10.1093/mnras/sty293.

Juráňová, A., N. Werner, P. E. J. Nulsen, M. Gaspari, K. Lakhchaura, R. E. A. Canning, M. Donahue, F. Hroch, and G. M. Voit (2020), Hot gaseous atmospheres of rotating galaxies observed with XMM-Newton, *MNRAS*, *499*(4), 5163–5174, doi:10.1093/mnras/staa3182.

Kempski, P., and E. Quataert (2020), Thermal instability of halo gas heated by streaming cosmic rays, *MNRAS*, *493*(2), 1801–1817, doi:10.1093/mnras/staa385.

Kereš, D., N. Katz, D. H. Weinberg, and R. Davé (2005), How do galaxies get their gas?, *MNRAS*, *363*(1), 2–28, doi:10.1111/j.1365-2966.2005.09451.x.

Kereš, D., N. Katz, M. Fardal, R. Davé, and D. H. Weinberg (2009), Galaxies in a simulated ΛCDM Universe - I. Cold mode and hot cores, *MNRAS*, *395*(1), 160–179, doi:10.1111/j.1365-2966.2009.14541.x.

Kim, W.-T., and R. Narayan (2003), Turbulent Mixing in Clusters of Galaxies, *ApJ*, *596*(2), L139–L142, doi:10.1086/379342.

Kolmogorov, A. (1941), The Local Structure of Turbulence in Incompressible Viscous Fluid for Very Large Reynolds' Numbers, *Akademiia Nauk SSSR Doklady*, *30*, 301–305.

Komiyama, M., K. Sato, R. Nagino, T. Ohashi, and K. Matsushita (2009), Suzaku Observations of Metallicity Distribution in the Intracluster Medium of the NGC 5044 Group, *PASJ*, *61*, S337–S352, doi:10.1093/pasj/61.sp1.S337.

Kormendy, J., and L. C. Ho (2013), Coevolution (Or Not) of Supermassive Black Holes and Host Galaxies, *ARA&A*, *51*, 511–653, doi:10.1146/annurev-astro-082708-101811.

Lakhchaura, K., N. Werner, M. Sun, R. E. A. Canning, M. Gaspari, S. W. Allen, T. Connor, M. Donahue, and C. Sarazin (2018), Thermodynamic properties, multiphase gas, and AGN feedback in a large sample of giant ellipticals, *MNRAS*, *481*(4), 4472–4504, doi:10.1093/mnras/sty2565.

Lau, E. T., M. Gaspari, D. Nagai, and P. Coppi (2017), Physical Origins of Gas Motions in Galaxy Cluster Cores: Interpreting Hitomi Observations of the Perseus Cluster, *ApJ*, *849*(1), 54, doi:10.3847/1538-4357/aa8c00.

Lauer, T. R., et al. (2005), The Centers of Early-Type Galaxies with Hubble Space Telescope. V. New WFPC2 Photometry, *AJ*, *129*, 2138–2185, doi:10.1086/429565.

Lee, D. (2013), A solution accurate, efficient and stable unsplit staggered mesh scheme for three dimensional magnetohydrodynamics, *Journal of Computational Physics*, *243*, 269–292, doi:10.1016/j.jcp.2013.02.049.

Lee, D., and A. E. Deane (2009), An unsplit staggered mesh scheme for multidimensional magnetohydrodynamics, *Journal of Computational Physics*, *228*, 952–975, doi:10.1016/j.jcp.2008.08.026.

Li, Y., and G. L. Bryan (2012), Simulating the Cooling Flow of Cool-core Clusters, *ApJ*, *747*, 26, doi:10.1088/0004-637X/747/1/26.

Li, Y., and G. L. Bryan (2014a), Modeling Active Galactic Nucleus Feedback in Cool-core Clusters: The Balance between Heating and Cooling, *ApJ*, *789*, 54, doi:10.1088/0004-637X/789/1/54.

Li, Y., and G. L. Bryan (2014b), Modeling Active Galactic Nucleus Feedback in Cool-core Clusters: The Formation of Cold Clumps, *ApJ*, *789*, 153, doi:10.1088/0004-637X/789/2/153.

Li, Y., G. L. Bryan, M. Ruszkowski, G. M. Voit, B. W. O'Shea, and M. Donahue (2015), Cooling, AGN Feedback, and Star Formation in Simulated Cool-core Galaxy Clusters, *ApJ*, *811*, 73, doi:10.1088/0004-637X/811/2/73.

Li, Y., M. Ruszkowski, and G. L. Bryan (2017), AGN Heating in Simulated Cool-core Clusters, *ApJ*, *847*, 106, doi:10.3847/1538-4357/aa88c1.

Li, Y., M. Ruszkowski, and G. Tremblay (2018a), The Effects of Ram Pressure on the Cold Clouds in the Centers of Galaxy Clusters, *ApJ*, *854*, 91, doi:10.3847/1538-4357/aaa843.

Li, Y., et al. (2020), Direct Detection of Black Hole-driven Turbulence in the Centers of Galaxy Clusters, *ApJ*, *889*(1), L1, doi:10.3847/2041-8213/ab65c7.

Li, Y.-P., F. Yuan, H. Mo, D. Yoon, Z.-M. Gan, L. C. Ho, B. Wang, J. P. Ostriker, and L. Ciotti (2018b), Stellar and AGN feedback in isolated early-type galaxies: the role in regulating star formation and ISM properties, *ArXiv e-prints*.

Lodato, G., and J. E. Pringle (2006), The evolution of misaligned accretion discs and spinning black holes, *MNRAS*, *368*(3), 1196–1208, doi:10.1111/j.1365-2966.2006.10194.x.

Loewenstein, M., and W. G. Mathews (1987), Evolution of Hot Galactic Flows, *ApJ*, *319*, 614, doi:10.1086/165482.

Ma, C.-P., J. E. Greene, N. McConnell, R. Janish, J. P. Blakeslee, J. Thomas, and J. D. Murphy (2014), The MASSIVE Survey. I. A Volume-limited Integral-field Spectroscopic Study of the Most Massive Early-type Galaxies within 108 Mpc, *ApJ*, *795*(2), 158, doi:10.1088/0004-637X/795/2/158.

Maoz, D., F. Mannucci, and T. D. Brandt (2012), The delay-time distribution of Type Ia supernovae from Sloan II, *MNRAS*, *426*, 3282–3294, doi:10.1111/j.1365-2966.2012.21871.x.

Martin, R. G., J. E. Pringle, and C. A. Tout (2007), Alignment and precession of a black hole with a warped accretion disc, *MNRAS*, *381*(4), 1617–1624, doi:10.1111/j.1365-2966.2007.12349.x.

Martini, P., D. Dicken, and T. Storchi-Bergmann (2013), The Origin of Dust in Early-type Galaxies and Implications for Accretion onto Supermassive Black Holes, *ApJ*, *766*, 121, doi:10.1088/0004-637X/766/2/121.

Martizzi, D., E. Quataert, C.-A. Faucher-Giguère, and D. Fielding (2019), Simulations of jet heating in galaxy clusters: successes and challenges, *MNRAS*, *483*(2), 2465–2486, doi:10.1093/mnras/sty3273.

Mathews, W. G. (1990), Interstellar events in elliptical galaxies, *ApJ*, *354*, 468–482, doi:10.1086/168708.

Mathews, W. G., and J. C. Baker (1971), Galactic Winds, *ApJ*, *170*, 241, doi:10.1086/151208.

Mathews, W. G., and F. Brighenti (2003), Hot Gas in and around Elliptical Galaxies, *ARA&A*, *41*, 191–239, doi:10.1146/annurev.astro.41.090401.094542.

Mathews, W. G., and M. Loewenstein (1986), Hot Galactic Flows, *ApJ*, *306*, L7, doi:10.1086/184693.

Mathews, W. G., A. Faltenbacher, and F. Brighenti (2006), Heating Cooling Flows with Weak Shock Waves, *ApJ*, *638*(2), 659–667, doi:10.1086/499119.

McCourt, M., P. Sharma, E. Quataert, and I. J. Parrish (2012), Thermal instability in gravitationally stratified plasmas: implications for multiphase structure in clusters and galaxy haloes, *MNRAS*, *419*, 3319–3337, doi:10.1111/j.1365-2966.2011.19972.x.

McKee, C. F., E. G. Zweibel, A. A. Goodman, and C. Heiles (1993), Magnetic Fields in Star-Forming Regions - Theory, in *Protostars and Planets III*, edited by E. H. Levy and J. I. Lunine, p. 327.

McNamara, B. R., and P. E. J. Nulsen (2007), Heating Hot Atmospheres with Active Galactic Nuclei, *ARA&A*, *45*, 117–175, doi:10.1146/annurev.astro.45.051806.110625.

McNamara, B. R., and P. E. J. Nulsen (2012), Mechanical feedback from active galactic nuclei in galaxies, groups and clusters, *New Journal of Physics*, *14*(5), 055023, doi: 10.1088/1367-2630/14/5/055023.

McNamara, B. R., H. R. Russell, P. E. J. Nulsen, M. T. Hogan, A. C. Fabian, F. Pulido, and A. C. Edge (2016), A Mechanism for Stimulating AGN Feedback by Lifting Gas in Massive Galaxies, *ApJ*, *830*(2), 79, doi:10.3847/0004-637X/830/2/79.

Meece, G. R., B. W. O'Shea, and G. M. Voit (2015), Growth and Evolution of Thermal Instabilities in Idealized Galaxy Cluster Cores, *ApJ*, *808*, 43, doi:10.1088/0004-637X/808/1/43.

Meece, G. R., G. M. Voit, and B. W. O'Shea (2017), Triggering and Delivery Algorithms for AGN Feedback, *ApJ*, *841*, 133, doi:10.3847/1538-4357/aa6fb1.

Mohapatra, R., and P. Sharma (2019), Turbulence in the intracluster medium: simulations, observables, and thermodynamics, *MNRAS*, *484*(4), 4881–4896, doi: 10.1093/mnras/stz328.

Mohapatra, R., C. Federrath, and P. Sharma (2020), Turbulence in stratified atmospheres: implications for the intracluster medium, *MNRAS*, *493*(4), 5838–5853, doi: 10.1093/mnras/staa711.

Morganti, R., P. T. de Zeeuw, T. A. Oosterloo, R. M. McDermid, D. Krajnović, M. Cappellari, F. Kenn, A. Weijmans, and M. Sarzi (2006), Neutral hydrogen in nearby elliptical and lenticular galaxies: the continuing formation of early-type galaxies, *MNRAS*, *371*(1), 157–169, doi:10.1111/j.1365-2966.2006.10681.x.

Navarro, J. F., C. S. Frenk, and S. D. M. White (1996), The Structure of Cold Dark Matter Halos, *ApJ*, *462*, 563, doi:10.1086/177173.

Navarro, J. F., C. S. Frenk, and S. D. M. White (1997), A Universal Density Profile from Hierarchical Clustering, *ApJ*, *490*, 493–508.

Negri, A., S. Pellegrini, and L. Ciotti (2015), X-ray haloes and star formation in early-type galaxies, *MNRAS*, *451*(2), 1212–1228, doi:10.1093/mnras/stv968.

O'Dea, C. P., et al. (2008), An Infrared Survey of Brightest Cluster Galaxies. II. Why are Some Brightest Cluster Galaxies Forming Stars?, *ApJ*, *681*, 1035–1045, doi: 10.1086/588212.

Ogorzalek, A., et al. (2017), Improved measurements of turbulence in the hot gaseous atmospheres of nearby giant elliptical galaxies, *MNRAS*, *472*, 1659–1676, doi: 10.1093/mnras/stx2030.

Olivares, V., et al. (2019), Ubiquitous cold and massive filaments in cool core clusters, *A&A*, *631*, A22, doi:10.1051/0004-6361/201935350.

Oosterloo, T., et al. (2010), Early-type galaxies in different environments: an HI view, *MNRAS*, *409*(2), 500–514, doi:10.1111/j.1365-2966.2010.17351.x.

O'Sullivan, E., D. A. Forbes, and T. J. Ponman (2001), A catalogue and analysis of X-ray luminosities of early-type galaxies, *MNRAS*, *328*, 461–484, doi:10.1046/j.1365-8711.2001.04890.x.

O'Sullivan, E., et al. (2017), The Complete Local Volume Groups Sample - I. Sample selection and X-ray properties of the high-richness subsample, *MNRAS*, *472*(2), 1482–1505, doi:10.1093/mnras/stx2078.

O'Sullivan, E., et al. (2018), Cold gas in a complete sample of group-dominant early-type galaxies, *A&A*, *618*, A126, doi:10.1051/0004-6361/201833580.

Padoan, P., E. Zweibel, and Å. Nordlund (2000), Ambipolar Drift Heating in Turbulent Molecular Clouds, *ApJ*, *540*, 332–341, doi:10.1086/309299.

Pakmor, R., C. Pfrommer, C. M. Simpson, and V. Springel (2016), Galactic Winds Driven by Isotropic and Anisotropic Cosmic-Ray Diffusion in Disk Galaxies, *ApJ*, *824*, L30, doi:10.3847/2041-8205/824/2/L30.

Panagoulia, E. K., A. C. Fabian, and J. S. Sanders (2014), A volume-limited sample of X-ray galaxy groups and clusters - I. Radial entropy and cooling time profiles, *MNRAS*, *438*(3), 2341–2354, doi:10.1093/mnras/stt2349.

Pandya, V., et al. (2017), The MASSIVE Survey. VI. The Spatial Distribution and Kinematics of Warm Ionized Gas in the Most Massive Local Early-type Galaxies, *ApJ*, *837*, 40, doi:10.3847/1538-4357/aa5ebc.

Panuzzo, P., R. Rampazzo, A. Bressan, O. Vega, F. Annibali, L. M. Buson, M. S. Clemens, and W. W. Zeilinger (2011), Nearby early-type galaxies with ionized gas. VI. The Spitzer-IRS view. Basic data set analysis and empirical spectral classification, *A&A*, *528*, A10, doi:10.1051/0004-6361/201015908.

Parriott, J. R., and J. N. Bregman (2008), Mass Loss from Evolved Stars in Elliptical Galaxies, *ApJ*, *681*, 1215-1232, doi:10.1086/588033.

Peng, Y., R. Maiolino, and R. Cochrane (2015), Strangulation as the primary mechanism for shutting down star formation in galaxies, *Nature*, *521*(7551), 192–195, doi:10.1038/nature14439.

Pfrommer, C. (2013), Toward a Comprehensive Model for Feedback by Active Galactic Nuclei: New Insights from M87 Observations by LOFAR, Fermi, and H.E.S.S., *ApJ*, *779*(1), 10, doi:10.1088/0004-637X/779/1/10.

Pillepich, A., et al. (2017), Simulating Galaxy Formation with the IllustrisTNG Model, *ArXiv e-prints*.

Pizzolato, F., and N. Soker (2005), On the Nature of Feedback Heating in Cooling Flow Clusters, *ApJ*, *632*, 821–830, doi:10.1086/444344.

Pouquet, A., D. Rosenberg, R. Marino, and C. Herbert (2018), Scaling laws for mixing and dissipation in unforced rotating stratified turbulence, *Journal of Fluid Mechanics*, *844*, 519–545, doi:10.1017/jfm.2018.192.

Prasad, D., P. Sharma, and A. Babul (2015), Cool Core Cycles: Cold Gas and AGN Jet Feedback in Cluster Cores, *ApJ*, *811*, 108, doi:10.1088/0004-637X/811/2/108.

Prasad, D., P. Sharma, and A. Babul (2018), Cool-core Clusters: The Role of BCG, Star Formation, and AGN-driven Turbulence, *ApJ*, *863*(1), 62, doi:10.3847/1538-4357/aacce8.

Pulido, F. A., B. R. McNamara, A. C. Edge, M. T. Hogan, A. N. Vantyghem, H. R. Russell, P. E. J. Nulsen, I. Babyk, and P. Salomé (2018), The Origin of Molecular Clouds in Central Galaxies, *ApJ*, *853*(2), 177, doi:10.3847/1538-4357/aaa54b.

Qiu, Y., T. Bogdanović, Y. Li, and M. McDonald (2019a), Using Hα Filaments to Probe Active Galactic Nuclei Feedback in Galaxy Clusters, *ApJ*, *872*(1), L11, doi:10.3847/2041-8213/ab0375.

Qiu, Y., T. Bogdanović, Y. Li, K. Park, and J. H. Wise (2019b), The Interplay of Kinetic and Radiative Feedback in Galaxy Clusters, *ApJ*, *877*(1), 47, doi:10.3847/1538-4357/ab18fd.

Qiu, Y., B. R. McNamara, T. Bogdanovic, K. Inayoshi, and L. C. Ho (2021), On the Mass Loading of AGN-Driven Outflows in Elliptical Galaxies and Clusters, *arXiv e-prints*, arXiv:2103.06505.

Rafferty, D. A., B. R. McNamara, P. E. J. Nulsen, and M. W. Wise (2006), The Feedback-regulated Growth of Black Holes and Bulges through Gas Accretion and Starbursts in Cluster Central Dominant Galaxies, *ApJ*, *652*(1), 216–231, doi:10.1086/507672.

Randall, S. W., et al. (2015), A Very Deep Chandra Observation of the Galaxy Group NGC 5813: AGN Shocks, Feedback, and Outburst History, *ApJ*, *805*, 112, doi:10.1088/0004-637X/805/2/112.

Rosen, A., and J. N. Bregman (1995), Global Models of the Interstellar Medium in Disk Galaxies, *ApJ*, *440*, 634, doi:10.1086/175303.

Russell, H. R., A. C. Fabian, B. R. McNamara, and A. E. Broderick (2015), Inside the Bondi radius of M87, *MNRAS*, *451*, 588–600, doi:10.1093/mnras/stv954.

Russell, H. R., et al. (2019), Driving massive molecular gas flows in central cluster galaxies with AGN feedback, *MNRAS*, *490*(3), 3025–3045, doi:10.1093/mnras/stz2719.

Ruszkowski, M., and S. P. Oh (2010), Shaken and Stirred: Conduction and Turbulence in Clusters of Galaxies, *ApJ*, *713*(2), 1332–1342, doi:10.1088/0004-637X/713/2/1332.

Ruszkowski, M., M. Brüggen, and M. C. Begelman (2004a), Cluster Heating by Viscous Dissipation of Sound Waves, *ApJ*, *611*, 158–163, doi:10.1086/422158.

Ruszkowski, M., M. Brüggen, and M. C. Begelman (2004b), Three-Dimensional Simulations of Viscous Dissipation in the Intracluster Medium, *ApJ*, *615*, 675–680, doi:10.1086/424702.

Ruszkowski, M., T. A. Enßlin, M. Brüggen, S. Heinz, and C. Pfrommer (2007), Impact of tangled magnetic fields on fossil radio bubbles, *MNRAS*, *378*, 662–672, doi:10.1111/j.1365-2966.2007.11801.x.

Ruszkowski, M., T. A. Enßlin, M. Brüggen, M. C. Begelman, and E. Churazov (2008), Cosmic ray confinement in fossil cluster bubbles, *MNRAS*, *383*, 1359–1365, doi:10.1111/j.1365-2966.2007.12659.x.

Ruszkowski, M., D. Lee, M. Brüggen, I. Parrish, and S. P. Oh (2011), Cosmological Magnetohydrodynamic Simulations of Cluster Formation with Anisotropic Thermal Conduction, *ApJ*, *740*(2), 81, doi:10.1088/0004-637X/740/2/81.

Ruszkowski, M., H. Y. K. Yang, and C. S. Reynolds (2017a), Cosmic-Ray Feedback Heating of the Intracluster Medium, *ApJ*, *844*(1), 13, doi:10.3847/1538-4357/aa79f8.

Ruszkowski, M., H.-Y. K. Yang, and E. Zweibel (2017b), Global Simulations of Galactic Winds Including Cosmic-ray Streaming, *ApJ*, *834*, 208, doi:10.3847/1538-4357/834/2/208.

Ruszkowski, M., H.-Y. K. Yang, and C. S. Reynolds (2018), Powering of Hα Filaments by Cosmic Rays, *ApJ*, *858*, 64, doi:10.3847/1538-4357/aaba72.

Salem, M., and G. L. Bryan (2014), Cosmic ray driven outflows in global galaxy disc models, *MNRAS*, *437*, 3312–3330, doi:10.1093/mnras/stt2121.

Sanders, J. S., and A. C. Fabian (2008), Sound waves in the intracluster medium of the Centaurus cluster, *MNRAS*, *390*, L93–L97, doi:10.1111/j.1745-3933.2008.00549.x.

Sanders, J. S., and A. C. Fabian (2013), Velocity width measurements of the coolest X-ray emitting material in the cores of clusters, groups and elliptical galaxies, *MNRAS*, *429*(3), 2727–2738, doi:10.1093/mnras/sts543.

Sanders, J. S., A. C. Fabian, S. W. Allen, R. G. Morris, J. Graham, and R. M. Johnstone (2008), Cool X-ray emitting gas in the core of the Centaurus cluster of galaxies, *MNRAS*, *385*, 1186–1200, doi:10.1111/j.1365-2966.2008.12952.x.

Schure, K. M., D. Kosenko, J. S. Kaastra, R. Keppens, and J. Vink (2009), A new radiative cooling curve based on an up-to-date plasma emission code, *A&A*, *508*, 751–757, doi:10.1051/0004-6361/200912495.

Serra, P., et al. (2012), The ATLAS^{3D} project - XIII. Mass and morphology of H I in early-type galaxies as a function of environment, *MNRAS*, *422*(3), 1835–1862, doi:10.1111/j.1365-2966.2012.20219.x.

Serra, P., et al. (2014), The ATLAS^{3D} project - XXVI. H I discs in real and simulated fast and slow rotators, *MNRAS*, *444*(4), 3388–3407, doi:10.1093/mnras/stt2496.

Sharma, P., P. Colella, and D. F. Martin (2009), Numerical Implementation of Streaming Down the Gradient: Application to Fluid Modeling of Cosmic Rays and Saturated Conduction, *ArXiv e-prints*.

Sharma, P., I. J. Parrish, and E. Quataert (2010), Thermal Instability with Anisotropic Thermal Conduction and Adiabatic Cosmic Rays: Implications for Cold Filaments in Galaxy Clusters, *ApJ*, *720*(1), 652–665, doi:10.1088/0004-637X/720/1/652.

Sharma, P., M. McCourt, E. Quataert, and I. J. Parrish (2012), Thermal instability and the feedback regulation of hot haloes in clusters, groups and galaxies, *MNRAS*, *420*(4), 3174–3194, doi:10.1111/j.1365-2966.2011.20246.x.

Sijacki, D., V. Springel, T. Di Matteo, and L. Hernquist (2007), A unified model for AGN feedback in cosmological simulations of structure formation, *MNRAS*, *380*, 877–900, doi:10.1111/j.1365-2966.2007.12153.x.

Simionescu, A., et al. (2019), Constraining Gas Motions in the Intra-Cluster Medium, *Space Sci. Rev.*, *215*(2), 24, doi:10.1007/s11214-019-0590-1.

Spitzer, L. (1978), *Physical processes in the interstellar medium*, doi: 10.1002/9783527617722.

Stern, J., D. Fielding, C.-A. Faucher-Giguère, and E. Quataert (2020), The maximum accretion rate of hot gas in dark matter haloes, *MNRAS*, *492*(4), 6042–6058, doi: 10.1093/mnras/staa198.

Stone, J. M., and M. L. Norman (1992), ZEUS-2D: A radiation magnetohydrodynamics code for astrophysical flows in two space dimensions. I - The hydrodynamic algorithms and tests., *ApJS*, *80*, 753–790, doi:10.1086/191680.

Sutherland, R. S., and M. A. Dopita (1993), Cooling functions for low-density astrophysical plasmas, *ApJS*, *88*, 253–327, doi:10.1086/191823.

Terzić, B., and A. W. Graham (2005), Density-potential pairs for spherical stellar systems with Sérsic light profiles and (optional) power-law cores, *MNRAS*, *362*, 197–212, doi: 10.1111/j.1365-2966.2005.09269.x.

Tremblay, G. R., et al. (2015), Far-ultraviolet morphology of star-forming filaments in cool core brightest cluster galaxies, *MNRAS*, *451*, 3768–3800, doi:10.1093/mnras/stv1151.

Tremblay, G. R., et al. (2016), Cold, clumpy accretion onto an active supermassive black hole, *Nature*, *534*(7606), 218–221, doi:10.1038/nature17969.

Valdarnini, R. (2019), A Multifiltering Study of Turbulence in a Large Sample of Simulated Galaxy Clusters, *ApJ*, *874*(1), 42, doi:10.3847/1538-4357/ab0964.

Valentini, M., and F. Brighenti (2015), AGN-stimulated cooling of hot gas in elliptical galaxies, *MNRAS*, *448*, 1979–1998, doi:10.1093/mnras/stv090.

van de Voort, F., Y. M. Bahé, R. G. Bower, C. A. Correa, R. A. Crain, J. Schaye, and T. Theuns (2017), The environmental dependence of gas accretion on to galaxies: quenching satellites through starvation, *MNRAS*, *466*(3), 3460–3471, doi:10.1093/mnras/stw3356.

van Dokkum, P. G., and M. Franx (1995), Dust in the Cores of Early-Type Galaxies, *AJ*, *110*, 2027, doi:10.1086/117667.

Vantyghem, A. N., B. R. McNamara, H. R. Russell, A. C. Edge, P. E. J. Nulsen, F. Combes, A. C. Fabian, M. McDonald, and P. Salomé (2018), Molecular Gas Filaments and Star-forming Knots Beneath an X-Ray Cavity in RXC J1504-0248, *ApJ*, *863*(2), 193, doi:10.3847/1538-4357/aad2e0.

Veale, M., C.-P. Ma, J. E. Greene, J. Thomas, J. P. Blakeslee, N. McConnell, J. L. Walsh, and J. Ito (2017), The MASSIVE Survey - VII. The relationship of angular momentum, stellar mass and environment of early-type galaxies, *MNRAS*, *471*(2), 1428–1445, doi:10.1093/mnras/stx1639.

Voit, G. M. (2018), A Role for Turbulence in Circumgalactic Precipitation, *ApJ*, *868*(2), 102, doi:10.3847/1538-4357/aae8e2.

Voit, G. M., and M. Donahue (2005), An Observationally Motivated Framework for AGN Heating of Cluster Cores, *ApJ*, *634*, 955–963, doi:10.1086/497063.

Voit, G. M., and M. Donahue (2015), Cooling Time, Freefall Time, and Precipitation in the Cores of ACCEPT Galaxy Clusters, *ApJ*, *799*, L1, doi:10.1088/2041-8205/799/1/L1.

Voit, G. M., M. Donahue, G. L. Bryan, and M. McDonald (2015a), Regulation of star formation in giant galaxies by precipitation, feedback and conduction, *Nature*, *519*, 203–206, doi:10.1038/nature14167.

Voit, G. M., M. Donahue, B. W. O'Shea, G. L. Bryan, M. Sun, and N. Werner (2015b), Supernova Sweeping and Black Hole Feedback in Elliptical Galaxies, *ApJ*, *803*, L21, doi:10.1088/2041-8205/803/2/L21.

Voit, G. M., G. Meece, Y. Li, B. W. O'Shea, G. L. Bryan, and M. Donahue (2017), A Global Model for Circumgalactic and Cluster-core Precipitation, *ApJ*, *845*, 80, doi:10.3847/1538-4357/aa7d04.

Wang, C., Y. Li, and M. Ruszkowski (2019), AGN feedback and multiphase gas in giant elliptical galaxies, *MNRAS*, *482*, 3576–3590, doi:10.1093/mnras/sty2906.

Wang, C., M. Ruszkowski, and H. Y. K. Yang (2020), Chaotic cold accretion in giant elliptical galaxies heated by AGN cosmic rays, *MNRAS*, *493*(3), 4065–4076, doi:10.1093/mnras/staa550.

Weinberger, R., K. Ehlert, C. Pfrommer, R. Pakmor, and V. Springel (2017a), Simulating the interaction of jets with the intracluster medium, *MNRAS*, *470*(4), 4530–4546, doi:10.1093/mnras/stx1409.

Weinberger, R., et al. (2017b), Simulating galaxy formation with black hole driven thermal and kinetic feedback, *MNRAS*, *465*, 3291–3308, doi:10.1093/mnras/stw2944.

Weinstock, J. (1981), Vertical turbulence diffusivity for weak or strong stable stratification, *J. Geophys. Res.*, *86*(C10), 9925–9928, doi:10.1029/JC086iC10p09925.

Werk, J. K., et al. (2014), The COS-Halos Survey: Physical Conditions and Baryonic Mass in the Low-redshift Circumgalactic Medium, *ApJ*, *792*, 8, doi:10.1088/0004-637X/792/1/8.

Werner, N., S. W. Allen, and A. Simionescu (2012), On the thermodynamic self-similarity of the nearest, most relaxed, giant ellipticals, *MNRAS*, *425*, 2731–2740, doi:10.1111/j.1365-2966.2012.21245.x.

Werner, N., et al. (2013), The Nature of Filamentary Cold Gas in the Core of the Virgo Cluster, *ApJ*, *767*(2), 153, doi:10.1088/0004-637X/767/2/153.

Werner, N., et al. (2014), The origin of cold gas in giant elliptical galaxies and its role in fuelling radio-mode AGN feedback, *MNRAS*, *439*, 2291–2306, doi:10.1093/mnras/stu006.

White, S. D. M., and M. J. Rees (1978), Core condensation in heavy halos: a two-stage theory for galaxy formation and clustering., *MNRAS*, *183*, 341–358, doi:10.1093/mnras/183.3.341.

Wiener, J., S. P. Oh, and F. Guo (2013a), Cosmic ray streaming in clusters of galaxies, *MNRAS*, *434*, 2209–2228, doi:10.1093/mnras/stt1163.

Wiener, J., E. G. Zweibel, and S. P. Oh (2013b), Cosmic Ray Heating of the Warm Ionized Medium, *ApJ*, *767*, 87, doi:10.1088/0004-637X/767/1/87.

Yang, H.-Y. K., and C. S. Reynolds (2016), How AGN Jets Heat the Intracluster Medium-Insights from Hydrodynamic Simulations, *ApJ*, *829*, 90, doi:10.3847/0004-637X/829/2/90.

Yang, H. Y. K., M. Gaspari, and C. Marlow (2019), The Impact of Radio AGN Bubble Composition on the Dynamics and Thermal Balance of the Intracluster Medium, *ApJ*, *871*(1), 6, doi:10.3847/1538-4357/aaf4bd.

Yi, S. K., et al. (2005), Galaxy Evolution Explorer Ultraviolet Color-Magnitude Relations and Evidence of Recent Star Formation in Early-Type Galaxies, *ApJ*, *619*, L111–L114, doi:10.1086/422811.

Yoast-Hull, T. M., J. E. Everett, J. S. Gallagher, III, and E. G. Zweibel (2013), Winds, Clumps, and Interacting Cosmic Rays in M82, *ApJ*, *768*, 53, doi:10.1088/0004-637X/768/1/53.

Yoo, H., and J. Cho (2014), Effects of Multiple-scale Driving on Turbulence Statistics, *ApJ*, *780*(1), 99, doi:10.1088/0004-637X/780/1/99.

Young, L. M., et al. (2011), The ATLAS^{3D} project - IV. The molecular gas content of early-type galaxies, *MNRAS*, *414*, 940–967, doi:10.1111/j.1365-2966.2011.18561.x.

Young, L. M., et al. (2014), The ATLAS^{3D} project - XXVII. Cold gas and the colours and ages of early-type galaxies, *MNRAS*, *444*(4), 3408–3426, doi:10.1093/mnras/stt2474.

Yuan, F., and R. Narayan (2014), Hot Accretion Flows Around Black Holes, *ARA&A*, *52*, 529–588, doi:10.1146/annurev-astro-082812-141003.

Yuan, F., D. Yoon, Y.-P. Li, Z.-M. Gan, L. C. Ho, and F. Guo (2017), Active Galactic Nuclei Feedback in an Elliptical Galaxy with the Most Updated AGN Physics (I): Low-angular Momentum Case, *ArXiv e-prints*.

Zhuravleva, I., E. Churazov, A. Kravtsov, and R. Sunyaev (2012), Constraints on the ICM velocity power spectrum from the X-ray lines width and shift, *MNRAS*, *422*(3), 2712–2724, doi:10.1111/j.1365-2966.2012.20844.x.

Zhuravleva, I., et al. (2014), Turbulent heating in galaxy clusters brightest in X-rays, *Nature*, *515*, 85–87, doi:10.1038/nature13830.

Zinger, E., A. Dekel, Y. Birnboim, A. Kravtsov, and D. Nagai (2016), The role of penetrating gas streams in setting the dynamical state of galaxy clusters, *MNRAS*, *461*(1), 412–432, doi:10.1093/mnras/stw1283.

ZuHone, J. A., M. Markevitch, and I. Zhuravleva (2016), Mapping the Gas Turbulence in the Coma Cluster: Predictions for Astro-H, *ApJ*, *817*(2), 110, doi:10.3847/0004-637X/817/2/110.

ZuHone, J. A., E. D. Miller, E. Bulbul, and I. Zhuravleva (2018), What Do the Hitomi Observations Tell Us About the Turbulent Velocities in the Perseus Cluster? Probing the Velocity Field with Mock Observations, *ApJ*, *853*(2), 180, doi:10.3847/1538-4357/aaa4b3.

Zweibel, E. G. (2013), The microphysics and macrophysics of cosmic raysa), *Physics of Plasmas*, *20*(5), 055501, doi:10.1063/1.4807033.

Zweibel, E. G. (2017), The basis for cosmic ray feedback: Written on the wind, *Physics of Plasmas*, *24*(5), 055402, doi:10.1063/1.4984017.

Zweibel, E. G., V. V. Mirnov, M. Ruszkowski, C. S. Reynolds, H.-Y. K. Yang, and A. C. Fabian (2018), Acoustic Disturbances in Galaxy Clusters, *ApJ*, *858*, 5, doi:10.3847/1538-4357/aab9ae.